Astronomy & Astrophysics manuscript no. output
February 3, 2020

Variability of OB stars from TESS southern Sectors 1-13 and high-resolution IACOB and OWN spectroscopy⋆

S. Burssens[1], S. Simón-Díaz[2,3], D. M. Bowman[1], G. Holgado[2,3,4], M. Michielsen[1], A. de Burgos[2,3,5], N. Castro[6], R. H Barbá[7], and C. Aerts[1,8,9,]

[1] Instituut voor Sterrenkunde, KU Leuven, Celestijnenlaan 200D, 3001 Leuven, Belgium
e-mail: siemen.burssens@kuleuven.be
[2] Instituto de Astrofísica de Canarias, 38200 La Laguna, Tenerife, Spain
[3] Departamento de Astrofísica, Universidad de La Laguna, 38205 La Laguna, Tenerife, Spain
[4] Centro de Astrobiología, CSIC-INTA, Campus ESAC, Camino bajo del Castillo s/n, E-28692 Madrid, Spain.
[5] Nordic Optical Telescope, E-38 711, Breña Baja, La Palma, Spain
[6] Leibniz-Institut für Astrophysik Potsdam (AIP), An der Sternwarte 16, 14482 Potsdam, Germany
[7] Departamento de Física y Astronomía, Universidad de La Serena, Avenida Juan Cisternas 1200, La Serena, Chile
[8] Department of Astrophysics, IMAPP, Radboud University Nijmegen, 6500 GL Nijmegen, The Netherlands
[9] Max Planck Institute for Astronomy, Königstuhl 17, 69117 Heidelberg, Germany

Received x xx, xxxx; accepted x x, xxx

ABSTRACT

Context. Lack of high-precision long-term continuous photometric data for large samples of stars has prevented the large-scale exploration of pulsational variability in the OB star regime. As a result, the candidates for in-depth asteroseismic modelling remained limited to a few tens of dwarfs. The TESS nominal space mission has surveyed the southern sky, including parts of the galactic plane, yielding continuous data of at least 27 d for hundreds of OB stars.
Aims. We aim to couple TESS data in the southern sky with ground-based spectroscopy to study the variability in two dimensions, mass and evolution. We focus mainly on the presence of coherent pulsation modes that may or may not be present in the predicted theoretical instability domains and unravel all frequency behaviour in the amplitude spectra of the TESS data.
Methods. We compose a sample of OB-type stars observed by TESS Sectors 1-13 and with available multi-epoch, high-resolution spectroscopy gathered by the IACOB and OWN surveys. We present the short-cadence 2-min light curves of dozens of OB-type stars, that have one or more spectra in the IACOB database. Based on these light curves and their Lomb-Scargle periodograms we perform variability classification and frequency analysis. We place the stars in a spectroscopic Hertzsprung-Russell diagram to interpret the variability in an evolutionary context.
Results. We find among the sample several new variable stars, including three hybrid pulsators, three eclipsing binaries, high frequency modes in a Be star, and potential heat-driven pulsations in two Oe stars.
Conclusions. We identify stars for which future asteroseismic modelling is possible, provided mode identification using additional data is achieved. By comparing the position of the variables to theoretical instability strips we discuss the current shortcomings in non-adiabatic pulsation theory, and the distribution of pulsators in the Hertzsprung-Russell diagram.

Key words. asteroseismology – stars: OB-type – techniques: photometry – techniques: spectroscopy

1. Introduction

OB-type stars are key in understanding the chemical, dynamical and energetic evolution of galaxies (e.g Langer 2012). Despite their importance, large uncertainties regarding their structure and evolution remain and strongly dictate the ultimate fate of these stars (Ekström et al. 2012; Georgy et al. 2012; Chieffi & Limongi 2013; Martins & Palacios 2013; Castro et al. 2014). Spectroscopic surveys such as the IACOB (Simón-Díaz et al. 2011a; Simón-Díaz et al. 2015), OWN (Barbá et al. 2010, 2014), GOSS (Sota et al. 2011), the two VLT-FLAMES massive star surveys (Evans et al. 2005, 2011) and MiMeS (Wade et al. 2016; Grunhut et al. 2017; Petit et al. 2019), have contributed significantly to our understanding of OB-type stars. More specifically, the effects of rotation (Dufton et al. 2013; Ramírez-Agudelo et al. 2013, 2015; Simón-Díaz & Herrero 2014; Dufton et al. 2018; Markova et al. 2018), the high rate of binarity (Sana et al. 2012, 2014), magnetic fields (Wade et al. 2016; Grunhut et al. 2017), and mass-loss through line-driven winds (Vink et al. 2011; Bestenlehner et al. 2014; Vink 2018) that are all important aspects of stellar evolution.

Despite tremendous efforts, direct access to OB-type star interiors is most powerful through *asteroseismology*. Analysis of stellar pulsations has gained traction across the Hertzsprung-Russell diagram (HRD), allowing for both direct inference of the internal rotation and chemical stratification from pulsation mode period spacing patterns in stars born with a convective

⋆ Based on observations made with the Nordic Optical Telescope (FIES), operated by NOTSA, and the Mercator Telescope (HERMES), operated by the Flemish Community, both at the Observatorio del Roque de los Muchachos (La Palma, Spain) of the Instituto de Astrofísica de Canarias. In addition observations collected with the FEROS spectrograph at the La Silla observatory in the framework of the OWN survey are used.

core (Van Reeth et al. 2015; Moravveji et al. 2015; Pápics et al. 2017; Ouazzani et al. 2019; Li et al. 2019) and determination of masses and ages through forward seismic modelling (Handler et al. 2006; Briquet et al. 2011; Kurtz et al. 2014; Moravveji et al. 2015, 2016; Schmid & Aerts 2016; Buysschaert et al. 2018a; Szewczuk & Daszyńska-Daszkiewicz 2018; Mombarg et al. 2019). A set back is that asteroseismology requires long term, near-continuous, high-precision data sets.

The era of studying OB-type star variability has arrived with the advent of high-precision (at μmag) space missions MOST (Walker et al. 2003), CoRoT (Auvergne et al. 2009), Kepler/K2 (Borucki et al. 2010; Howell et al. 2014) and now the Transiting Exoplanet Survey Satellite (TESS, Ricker et al. 2014). The first two TESS sectors have already shown that OB-type stars show diverse variability (Pedersen et al. 2019; Handler et al. 2019; Bowman et al. 2019b). These studies provide an exploratory evolutionary context and mass range based on distance and brightness measurements assembled by the ESA Gaia mission (Gaia Collaboration et al. 2016, 2018), which included (large) uncertainties linked to extinction and reddening effects. Coupling the photometric wealth of TESS observations to high-resolution spectroscopy for OB-type stars is the next step in understanding how to improve our knowledge of stellar evolution.

Coherent pulsations in OB-type ($M \gtrsim 3$ M$_\odot$) stars[1] come in two main flavours, gravity (g) modes — historically associated with the Slowly Pulsating B stars (Waelkens 1991; De Cat & Aerts 2002) — and pressure (p) modes — historically associated with β Cep type variables (Frost 1902; Stankov & Handler 2005). These coherent pulsation modes are standing waves for which the dominant restoring forces are buoyancy and the pressure force, respectively (Moskalik & Dziembowski 1992; Dziembowski & Pamiatnykh 1993; Dziembowski et al. 1993; Gautschy & Saio 1993). Using stellar evolution and pulsational codes, instability regions can be calculated (Pamyatnykh 1999; Miglio et al. 2007; Szewczuk & Daszyńska-Daszkiewicz 2017; Godart et al. 2017). These strips are sensitive to metallicity (Pamyatnykh 1999), rotation (Szewczuk & Daszyńska-Daszkiewicz 2017), opacity and the chemical mixture (Miglio et al. 2007; Salmon et al. 2012; Walczak et al. 2015; Moravveji 2016). Coherent pulsations are also found in Be and Oe stars, which are main sequence stars with spectral types that range between late O and early A, and show at least one Balmer line in emission (Porter & Rivinius 2003). The origin of the emission feature is likely related to episodic mass ejections producing a circumstellar disk, which is induced by a combination of fast rotation and stellar pulsations (Townsend et al. 2004; Huat et al. 2009; Neiner et al. 2013; Kurtz et al. 2015; Baade et al. 2016; Rivinius et al. 2016; Pápics et al. 2017; Baade et al. 2018).

In addition to coherent pulsations, internal gravity waves (IGWs) are also predicted in massive stars. These are travelling waves excited at the interface of convective and radiative zones. Numerical simulations of OB-type stars, have shown that the turbulent motions are able to generate IGWs by the convective cores of these stars (Rogers et al. 2013; Edelmann et al. 2019; Augustson & Mathis 2019). Every star with a convective core is expected to generate IGWs. They are efficient at transporting angular momentum and chemical species within such stars (Rogers et al. 2013; Rogers 2015; Rogers & McElwaine 2017; Aerts et al. 2019 — see Aerts 2019 for an extensive overview). The recent near-ubiquitous detection of stochastic low frequency variability in space photometry of OB-type stars reveals a frequency spectrum that is consistent with predictions from numerical simulations of IGWs generated by core convection (Aerts & Rogers 2015; Ramiaramanantsoa et al. 2018; Bowman et al. 2019a,b). By comparing different samples of Galactic and LMC OB-type stars, Bowman et al. (2019b) highlighted that the morphology of the stochastic low frequency variability in massive stars is connected to the luminosity (i.e. mass and age) yet insensitive to the metallicity of the star. It is also thought that IGW are partly responsible, alongside heat-driven modes, for the turbulent motions inducing line-profile variations in OB-type stars (Aerts et al. 2009; Simón-Díaz et al. 2010; Aerts & Rogers 2015; Tkachenko et al. 2014; Simón-Díaz et al. 2017; Aerts et al. 2017b; Godart et al. 2017; Simón-Díaz et al. 2018). An alternative and non-mutually exclusive explanation for the detected low-frequency power excess could also be sub-surface convective associated with the iron opacity peak (Cantiello et al. 2009; Lecoanet et al. 2019), although this is not efficient in stars with a mass between 3 and 7 solar masses and strongly depends on the host star's metallicity (Cantiello & Braithwaite 2019), while such stars do reveal low-frequency variability due to a stochastic process (Bowman et al. 2019a; Pedersen 2020).

In this work we combine high-resolution spectroscopy, from the large-scale spectroscopic surveys IACOB (Simón-Díaz et al. 2011a,b; Simón-Díaz et al. 2015) and OWN (Barbá et al. 2010, 2014), with high-precision long term continuous photometry from TESS (Ricker et al. 2014) to study variability in OB-type stars. By populating the HRD we constrain the different types of variability seen in main sequence (from now defined as MS) O and B-stars as well as B-type supergiants, and compare them to theoretically predicted instability regions.

2. Methodology

TESS is currently observing many stars across the sky in consecutive sectors every month for at least ~ 27 d. Data are now available for all sectors (1-13) covered by the nominal TESS mission in the southern hemisphere. Until Sector 6 the number of Galactic OB-type stars observed was limited. In Sector 6 the southern part of the Galactic plane started to be surveyed by TESS. Sectors 6 to 8 thus contain a large variety of OB-type stars ranging from main sequence OB dwarfs to OB supergiants.

Our sample of stars is based on the list of Galactic OB stars for which the IACOB project has, at least, one high resolution spectrum available. Based on the coordinates of each star we scanned the southern hemisphere using the high-precision TESS pointing tool[2]. Every star in the IACOB database with at least one epoch, that falls on one of the TESS cameras was searched for in the TESS Candidate Target List (CTL, Stassun et al. 2018). Spectral types of B3 and earlier, for the V and IV luminosity classes, and B8 and earlier for luminosity classes I and II, are included here. Dwarf stars earlier than B3 have approximately 5 M$_\odot$ or higher, while the supergiant B8 stars, and earlier, are expected to be similar mass stars in a more advanced stage of evolution. The galactic distribution of the stars in our sample is shown in Fig. 1. The distribution of stars over the sectors is shown in Fig. 2.

2.1. TESS aperture photometry

TESS data in short cadence is assembled from the Mikulski Archive for Space Telescopes (MAST[3]) archive as target pixel

[1] This includes O- and early B-type main sequence stars as well as B-type supergiants.

[2] https://github.com/christopherburke/tess-point

[3] https://archive.stsci.edu/

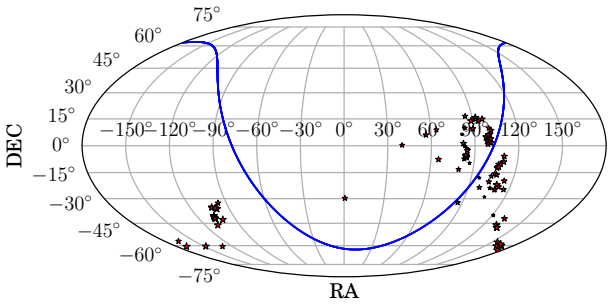

Fig. 1: Location of the stars in our sample in galactic coordinates. The galactic plane (in blue) is plotted as reference.

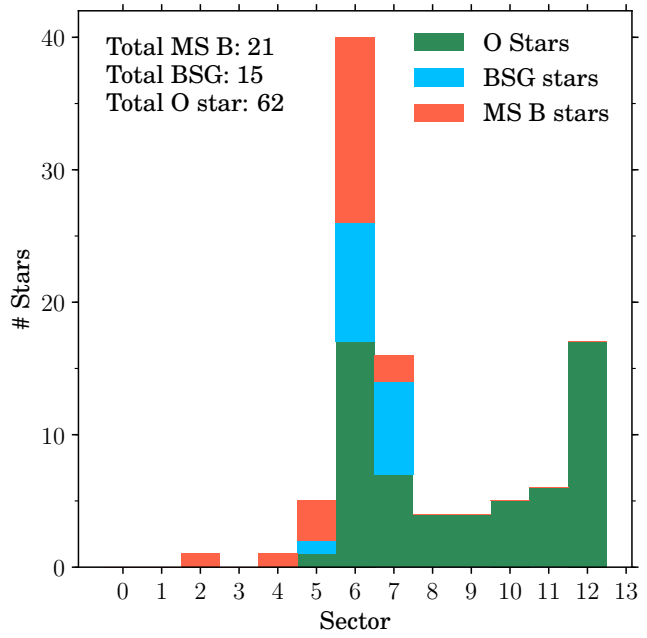

Fig. 2: Stacked histogram showing the distribution of the stars observed in each sector.

files (TPF) and as light curves (LC). The light curves are available in calibrated (PDCSAP, Pre-search Data Conditioning Simple Aperture Photometry) and pre-conditioned form (SAP, Simple Aperture Photometry). The TESS data reduction pipeline is tailored to stars with potential exoplanets (Jenkins et al. 2016). We therefore performed a case-by-case viewing of the aperture mask assigned by the TESS pipeline and the extracted light curve. If the mask selection was poor (i.e. wrong star, or large contamination by nearby stars) we extracted an optimised light curve following the methodology in Buysschaert et al. (2015, 2018b).

2.2. IACOB Spectroscopy

The stars considered in this work cover a wide range in mass ($\approx 5-80\,M_\odot$) and evolutionary stage. It is therefore important to locate them as accurately as possible in the HRD for any further interpretation of the detected variability as a function of mass and age.

We use the large database of high resolution spectra of Galactic OB-type stars compiled in the last decade. This mainly refers to the IACOB spectroscopic database, comprising spectra of Northern O and B-type stars obtained with the HERMES (Raskin et al. 2011) and FIES (Telting et al. 2014) spectrographs attached to the 1.2-m *Mercator* telescope, and the 2.6-m NOT telescope, respectively, but also includes high resolution observations of Southern O-type stars gathered by the OWN survey with the FEROS (Kaufer et al. 1997) instrument attached to the ESO/MPG 2.2-m telescope at the ESO La Silla observatory in Chile. For an important fraction of the stars under study the multi-epoch character of the observations compiled by these projects has allowed us to probe possible line-profile variability. In addition, we were able to identify stars with strong (variable) stellar winds and/or other type of circumstellar material which is physically related to the interpretation of the photometric variability. We classify the spectroscopic signatures following Holgado et al. (2018). The following cases are differentiated:

- *C*: constant, two or more spectra show no significant differences in line profile or radial velocity;
- *SB1, SB2*: spectroscopic binarity, if one or multiple components are detected, shifted in radial velocity;
- *WVa/WVe*: variability seen in the wind lines, i.e. H_α and/or HeII4686. We differentiate between variability in emission (WVe) and variability in absorption (WVa);
- *LPV*: any line profile variations not clearly assignable to any of the above cases;
- *S*: Only a single spectrum was available.

These signatures are assigned by viewing overplotted spectra. In addition we calculate the first two lowest-order line-profile moments (see Aerts et al. 1992, for a definition) over the multiple epochs, should the visual inspection be unclear. These correspond with equivalent width (EW) and radial velocity ($<v>$). We note that our variability assignments based on these spectroscopic metrics are mostly qualitative, and serve mainly to complement the interpretation of the TESS data. Several peculiar stars are considered separately: the Oe stars or stars showing signatures of a magnetosphere.

Additionally, we make use of parameters from a quantitative spectroscopic analysis to place the stars in the spectroscopic Hertzsprung-Russell diagram[4] (sHRD). The reduction, normalization, analysis and extraction of the spectroscopic parameters are discussed in Holgado et al. (2017, 2018), and Simón-Díaz et al. (2017) for the case of the O-, and B-type stars, respectively[5]. The stars included in our final sample and their spectroscopic properties are given in Table 1.

We note that despite we used all the spectroscopic variability classifiers indicated above during the analysis process, we do not show in Table 1 the C and S labels, and only quote those cases labelled as LPV in which clear variability is detected.

2.3. TESS photometric variability classification

We compute Lombs-Scargle periodograms (LS; Lomb 1976; Scargle 1982) to obtain an amplitude spectrum for each TESS

[4] This diagnostic diagram, first proposed by (Langer & Kudritzki 2014), and widely used in the literature since then (Castro et al. 2014; Simón-Díaz & Herrero 2014; Markova et al. 2018; Holgado et al. 2018; Castro et al. 2018), replaces the stellar luminosity by the parameter $\mathscr{L} := T_{\rm eff}^4/{\rm log}g$, hence removing the uncertainties resulting from the propagation of uncertainties in distance and reddening correction.

[5] The work by Holgado et al. (2017, 2018) extends and supersedes previous information on the O-type stars included in Simón-Díaz et al. (2017).

Table 1: Overview of the spectroscopic instruments used in this work.

Telescope	Instrument	Resolving power	Range [Å]
2.56m NOT	FIES	46000/25000	3750-7250
1.2m *Mercator*	HERMES	85000	3770-9000
2.2m ESO/MPG	FEROS	48000	3530-9210

light curve. Each TESS sector data set contains up to 27 d of near-continuous high-precision photometry, and stars in multiple sectors are concatenated. Ten stars in our sample have two available sectors in the 2-min cadence, instead of one. The frequency resolution of the amplitude spectra is defined as the reciprocal of the time-span: $1/\Delta T$. The 2-min cadence of the targets in the TESS CTL yields a Nyquist frequency of $\nu_{\rm Ny} = 359.995$ d^{-1}. Based on visual inspection of the light curves and their LS-periodograms we provide a variability classification based on the range of frequencies and amplitudes. Additionally all light curves are run through a frequency analysis, following the methodology described in Burssens et al. (2019), using the conservative significance criterion that the peak must have a signal-to-noise (S/N) above 4 using a 5 d^{-1} window for estimating the noise level. We refer to Appendix A for further details.

We differentiate between the following variability types:

- *β Cep*: coherent pressure modes with frequencies between approximately 3 and 20 d^{-1};
- *SPB*: coherent gravity modes with frequencies below approximately 4 d^{-1};
- *hybrid*: a combination of β Cep and SPB;
- *SLF*: stochastic low-frequency variability with broad amplitude excess, which is different from coherent modes, and has periods of several hours to days and amplitudes up to a few mmag;
- *EB*: eclipsing binary;
- *rot*: rotational variability caused by spots and/or stellar wind;
- *Contam./poor quality data (PQD)*: Light curve is contaminated by nearby star or instrumental periodicities dominate the LS-periodogram.

To assist the classification we estimate the possible rotation frequency range based on the measured v sin i, an average near-critical rotation velocity v= 450 km s^{-1}, and an assumed radius. The rotation frequency $\nu_{\rm rot}$ (in d^{-1}) is given by:

$$\nu_{\rm rot} \approx 0.02 {\rm v}_{\rm rot}({\rm R}_\odot/{\rm R}), \quad (1)$$

where $\rm v_{rot}$ is the equatorial velocity in km s^{-1} and $R/{\rm R}_\odot$ the radius of the star in solar units. The radii are taken from fundamental parameter studies by Martins et al. (2005) for the O-type stars, and Searle et al. (2008) for the blue supergiants (who incorporate results from the analysis by Crowther et al. 2006). These studies used non-LTE, line-blanketed atmosphere models computed with CMFGEN (Hillier & Miller 1998), which were compared to observations of representative stars. The derived fundamental parameters were used to calibrate the fundamental parameters for each spectral type by ways of an interpolation. Martins et al. (2005) report a standard deviation of $10-20$ %, and Searle et al. (2008) around 10 % on the calibrated radius. For the B dwarfs we use the tabulated values by Gray (2005).

Disentangling the contributions of rotational modulation and low frequency modes remains difficult as both may be simultaneously present. In this work we classified as potential rotational variables those stars where the main variability (or a significant contribution) is due to a single frequency and its (sub-)harmonics (following e.g. Buysschaert et al. 2018b; Sikora et al. 2019). As indicated above rotational variability is expected to be caused by spots and/or stellar wind.

We provide the results of the variability classification in Table 1. Uncertain classification is indicated by a question mark. In the case of pulsators this means that the 27 d TESS data set is insufficient to resolve the complex beating of g modes in the low-frequency regime. Therefore some degeneracy exists between the SLF and the SPB classification. The full results of the frequency analysis are given in Appendix A. There we provide an overview table (Table A.1), as well as full frequency lists of the multi-periodic stars discussed in the main text (Table A.2).

3. Results

We populate the sHRD in Fig. 3 where we combine the TESS photometric variability classification and the parameters from the spectroscopic analysis. On the left panels of Fig. 3, we sort the stars according to their spectral type, in the same manner as Table 1. On the right panels of Fig. 3, we sort the stars according to their variability classification.

To situate the approximate masses and evolutionary stages of the stars we compute evolutionary tracks for M $\in [3, 4, 5, 6, 7, 8, 10, 12, 15, 20, 25, 32, 40, 50, 60, 80]$ M$_\odot$ with the MESA stellar evolution code (Paxton et al. 2011, 2013, 2015, 2018, v.12115), for $Z_{\rm ini} = 0.014$, an initial hydrogen abundance $X_{\rm ini} = 0.71$, an exponential core overshoot of $f_{\rm ov} = 0.02$, and envelope mixing coefficient $\log D_{\rm mix} = 1.0$, the Nieva & Przybilla (2012) heavy element mixture, and the standard MESA OP opacity tables (Paxton et al. 2011). Using these tracks and the GYRE stellar oscillation code (Townsend & Teitler 2013; Townsend et al. 2018, v.5.2) we also calculate instability regions along the main sequence for both low-order p modes and high-order g modes for spherical degree $\ell = 0-2$ and $\ell = 1-2$, respectively. In this we solve for non-adiabatic oscillations (see appendix A in Townsend et al. 2018) at spaced intervals of $X_{\rm c} = 0.05$ starting from the Zero-Age Main Sequence (ZAMS) up to core hydrogen depletion, and analyse their stability. We consider azimuthal orders $-\ell \leq m \leq \ell$ and radial orders from n_{pg} from -50 to -1 for g modes and n_{pg} from 1 to 5 for p modes. The results of these computations are presented in the right panel of Fig. 3. In Section 4.1 we examine the effect of metallicity on the instability strips. The detailed MESA and GYRE set-ups are given in Appendix B.

It can be noticed that the highest density of stars in the sHRD is found in the O star domain, including MS stars with evolutionary masses in the range $\sim 20-80$ M$_\odot$. This is just a consequence of the origin of the compiled spectroscopic data sets being biased towards these stars. Since we are dealing with stars in the TESS Southern sectors, most of our spectra come from the OWN survey, which is mostly concentrated in the monitoring of Southern O-type stars. All the remaining B-type stars are drawn from the Northern IACOB survey, hence resulting in a much smaller overlap with the stars included in TESS Sectors 1 - 13. As a result, and despite the large number of B-type supergiants comprising the present version of the IACOB spectroscopic database, the sample of stars of these type considered in this work is very scarce, with no more than 7 B-type stars apparently located beyond the TAMS. The situation is much better for the case of the

HD	SpT		$\log T_{\rm eff}$	$\log \mathscr{L}/\mathscr{L}_{\odot}$	$v \sin i$	$v_{\rm mac}$	# sp.	Sp. Var. Type	TESS Var. Type
	O-type dwarfs and subgiants (V and IV)								
HD 96715	O4	V((f))z	4.66	4.10	59	86	2	...	SLF
HD 46223	O4	V((f))	4.62	4.16	60	91	7	...	SLF+SPB?
HD 155913	O4.5	Vn((f))	4.63	3.88	278	...	9	...	rot
HD 46150	O5	V((f))z	4.61	4.03	71	94	20	SB1?	SLF
HD 90273	ON7	V	4.59	3.95	55	55	1	...	SLF+SPB?
HD 110360	ON7	V	4.59	3.60	96	86	2	SB1	PQD
HD 47839	O7	V	4.58	3.70	43	65	113	SB1	SLF+β Cep
HD 46485	O7	V((f))nz var?	4.55	3.74	322	...	3	SB1?	EB
HD 53975	O7.5	Vz	4.56	3.74	181	...	5	SB1	SLF+rot
HD 41997	O7.5	Vn((f))	4.55	3.85	262	...	4	...	SLF+rot?
HD 152590	O7.5	Vz	4.58	3.79	48	56	10	SB1	EB
HD 46573	O7	V((f))z	4.56	3.93	77	81	5	SB1	SLF+rot?
HD 48279	O8	V	4.55	3.76	131	74	4	...	SLF+SPB?
HD 101191	O8	V	4.55	3.80	138	...	4	...	cont.
HD 46056	O8	Vn	4.55	3.58	370	...	4	...	PQD
HD 38666	O9.5	V	4.53	3.59	111	56	11	...	PQD
HD 36512	O9.7	V	4.51	3.44	13	33	23	SB1	SLF+rot
HD 123056	O9.5	IV(n)	4.50	3.70	193	...	9	SB1	SLF+SPB?
HD 76556	O6	IV(n)((f))p	4.58	3.80	239	...	4	...	SLF+SPB?
HD 74920	O7.5	IVn((f))	4.54	3.90	291	...	1	...	SLF+SPB?
HD 135591	O8	IV((f))	4.54	3.99	60	60	3	...	SLF
HD 326331	O8	IVn((f))	4.54	3.82	332	...	6	WVa	SLF
HD 37041	O9.5	IVp	4.51	3.01	191	...	30	SB1	SLF+SPB?
HD 48099	O5 V((f))z + O9: V		...	...	...	...	4	SB2	SLF+rot
HD 159176	O7 V((f)) + O7 V((f))		...	...	...	...	4	SB2	EB
HD 54662	O7 Vzvar?		...	...	...	...	12	SB2	SLF+SPB?
HD 57236	O8.5 V + ?		...	...	...	...	6	SB2	SLF+rot
HD 75759	O9 V + B0 V		...	...	...	...	6	SB2	SLF
HD 37468	O9.5 V + B0.5 V		...	...	...	...	80	SB2	cont.
	O-type giants, bright giants and supergiants (III, II and I)								
HD 66811	O4	I(n)fp	.. .	...	198	12	10	...	SLF+rot
HD 97253	O5	III(f)	4.59	4.16	70	105	2	WVa	SLF+SPB?
HD 93843	O5	III(fc)	4.57	4.15	58	120	4	WVa	SLF+rot
HD 156738	O6.5	III(f)	4.58	3.87	65	103	2	...	SLF
HD 36861	O8	III((f))	4.55	4.06	53	75	881	...	SLF
HD 150574	ON9	III(n)	4.52	3.87	252	...	1	...	SLF+SPB?
HD 152247	O9.2	III	4.51	3.94	82	96	7	SB1	SLF+rot
HD 55879	O9.7	III	4.49	3.85	26	60	9	...	SLF+SPB?
HD 154643	O9.7	III	4.49	3.85	101	78	5	SB1	SLF
HD 152233	O6	II(f)	4.58	4.01	62	105	9	SB1?	cont.
HD 57061	O9	II	4.51	4.01	57	93	9	WVa/SB1	EB
HD 36486	O9.5	II Nwk	4.51	3.99	121	96	65	SB1	EB
CPD -472963	O5	Ifc	4.57	4.16	67	110	5	WVa	SLF+SPB?
HD 57060	O7	Iafp var	...	...	...	...	12	WVe/SB1	EB
HD 156154	O7.5	Ib(f)	4.53	4.22	62	102	4	WVa	SLF+SPB?
HD 112244	O8.5	Iab(f)p	4.50	4.15	124	80	12	WVe/SB1?	SLF
HD 151804	O8	Iaf	4.45	4.33	72	73	2	WVe	SLF +SPB
HD 47129	O8	fp var	...	...	...	...	5	WVe/SB1	EB+rot?
HD 303492	O8.5	Iaf	4.45	4.29	87	55	4	WVe	SLF+SPB
HD 152249	OC9	Iab	4.49	4.15	71	70	19	WVe	SLF+SPB?
HD 152424	OC9.2	Ia	4.48	4.14	59	66	5	WVe/SB1	SLF+SPB

Table continued on the next page.

Table 1: Continued.

HD	SpT	log $T_{\rm eff}$	log $\mathscr{L}/\mathscr{L}_\odot$	v sin i	$v_{\rm mac}$	# sp.	Sp. Var. Type	TESS Var. Type
	O-type giants, bright giants and supergiants (III, II and I) (continued)							
HD 154368	O9.5 Iab	4.48	4.28	65	78	5	WVe	SLF+SPB?
HD 152003	O9.7 Iab Nwk	4.48	4.12	65	83	2	WVe	SLF+rot
HD 152147	O9.7 Ib Nwk	4.48	4.04	91	64	4	WVa/SB1	SLF+SPB?
HD 37043	O9 III + B1 III/IV	...	...	...	...	99	SB2	SLF+SPB?
	Early B-type dwarfs, subgiants and giants (V, IV, and III)							
HD 36960	B0.5 V	4.46	3.31	23	37	4	...	SLF
HD 37042	B0.7 V	4.47	3.06	33	13	25	...	SLF+rot
HD 36959	B1 V	4.41	2.82	11	14	2	...	contam.
HD 43112	B1 V	4.41	2.95	7	12	1	...	SLF+rot
HD 37303	B1.5 V	4.32	2.88	280	...	1	...	hybrid
HD 35912	B2 V	4.26	2.44	11	21	2	LPV	SPB
HD 48977	B2.5 V	4.25	2.61	26	8	1	LPV/SB2?	SPB
HD 23466	B3 V	4.20	2.51	75	100	1	...	EB
HD 34816	B0.5 IV	4.46	3.22	25		1	...	rot
HD 46328	B0.5 IV	4.40	3.28	7	20	2	LPV/SB1?	β Cep
HD 50707	B1 IV	4.38	3.31	29	46	2	LPV/SB1?	β Cep
HD 37481	B1.5 IV	4.34	2.78	74	21	2	...	hybrid
HD 16582	B2 IV	4.34	2.94	9	19	1	...	β Cep
HD 37209	B2 IV	4.38	2.76	50	15	2	...	hybrid
HD 26912	B3 IV	4.20	2.61	53	30	1	...	SPB
HD 37711	B3 IV	4.21	2.61	68	51	3	LPV/SB1?	SPB
HD 57539	B3 IV	4.13	2.54	162	13	1	...	SPB
HD 41753	B3 IV	4.23	2.61	25	40	1	...	SPB
HD 224990	B5 IV	4.13	2.33	20	40	1	...	SPB?
HD 37018	B1 V + ?	...	...	...	...	33	SB2	SLF+rot
	B-type giants, bright giants and supergiants (LCs III, II, and I)							
HD 48434	B0 III	4.48	3.93	48	82	3	WVa	SLF
HD 61068	B2 III	4.39	3.08	12	23	2	LPV/SB1?	β Cep
HD 35468	B2 III	4.29	2.99	53	27	5	...	SLF+rot
HD 44743	B1 II-III	4.37	3.20	24	40	6	LPV/SB1?	β Cep
HD 54764	B1 II	4.30	3.97	123	87	3	...	SLF+rot
HD 52089	B2 II	4.34	3.60	26	50	21	...	SLF+rot
HD 62747	B2 II	4.34	3.36	98	29	2	SB1	EB
HD 51309	B3 II	4.20	3.64	27	43	11	...	SLF+SPB
HD 46769	B5 II	4.11	3.16	70	23	25	...	SLF+rot
HD 27563	B7 II	4.16	2.61	34	26	1	...	SLF+SPB
HD 53244	B8 II	4.14	2.74	36	21	3	...	SLF+rot
HD 37128	B0 Ia	4.47	4.05	55	85	281	WVe	SLF+SPB?
HD 38771	B0.5 Ia	4.47	4.06	53	83	247	WVe	SLF+SPB
HD 53138	B3 Iab	4.23	4.13	37	56	12	WVe	SLF+SPB
HD 39985	B9 Ib	4.11	2.34	26	28	7	...	SLF+rot

Table continued on the next page.

B-type stars populating the MS. In this case, we have a relatively good coverage of stars in the mass range 6 – 20 $M_\odot$.

We highlight in Table 3 (and the left panel of Fig. 3 for the case of SB1 systems) those stars identified as spectroscopic binaries. In the same table, we identify as separated groups those stars with a confirmed detection of a magnetic field, or which are classified as Oe/Be stars (see Sect. 3.4), and highlight those stars for which we have detected line profile variability in H_α. All these identifiers add complementary information of interest for the correct interpretation of the TESS light curves.

Table 2 provides a global summary of the number of spectroscopic binaries, stars with detected magnetic fields and Oe/Be

Table 1: Continued.

HD	SpT		$\log T_{\rm eff}$	$\log \mathscr{L}/\mathscr{L}_\odot$	$v \sin i$	$v_{\rm mac}$	# sp.	Sp. Var. Type	TESS Var. Type
				Magnetic O- and B-type stars					
HD 37022	O7	Vp	...	...	23	68	67	...	cont.
HD 37061	O9	V	4.45	3.01	191	93	4	SB1	rot
HD 37742	O9.2	Ib var Nwk	4.47	4.15	122	97	177	WVe/SB1	SLF
HD 57682	O9.2	IV	4.54	3.62	12	38	5	...	SLF+rot?
HD 54879	O9.7	V	4.52	3.16	7	10	8	...	SLF+rot
HD 37479	B2	Vp	...	...	...	...	2	...	rot
				Oe and Be stars					
HD 39680	O6	V:[n]pevar	...	...	101	31	4	...	SLF+SPB?
HD 45314	O9:	npe	...	...	128	4	5	...	SLF+SPB?
HD 58978	B0	IV:e	...	...	...	...	2	...	β Cep

Header: $v \sin i$ and $v_{\rm mac}$ are given in units of km s^{-1}, # sp. indicates the number of available spectra, Sp. Var. Type and TESS Var. Type indicate the spectroscopic and photometric variability classifications respectively.
TESS Variability types: EB (Eclipsing binary), rot (Rotational modulation), SPB (low frequency pulsation modes), β Cep (high frequency pulsation modes), SLF (stochastic low frequency signal), PQD (poor quality data), or cont. (contaminated). A question mark indicates that the TESS light curve is insufficient to disentangle the contribution of g-modes, rotation effects and SLF.
Spectroscopic Variability types: SB1/SB2 (Single/double line spectroscopic binary), LPV (Line profile variability in photospheric lines), WVa/WVe (Variability of the H_α line in absorption/emission).

Table 2: Global overview of the number of spectroscopic binaries, stars with detected magnetic fields and Oe/Be stars found in our working sample. The numbers in brackets indicates the total number of O- and B-type stars.

	SB1	SB1?	SB2	SB2?	Mag.	Oe/Be
O-type (61)	19	4	7	0	6	2
B-type (38)	2	4	2	1	1	1

stars in our working sample. We also note a few cases (identified as LPV/SB1? and LPV/SB2?) in which the detected spectroscopic variability is more likely associated with the effect of β Cep- and SPB-type pulsations on the shape of the line profiles[6] than with orbital motion in a single or double line binary system. Also, it is interesting to note that most of the stars identified as eclipsing binaries (EB) from the inspection of the TESS light curves are also labelled as SB1 or SB2 systems. In the next sections we provide more detailed comments about various groups of interest regarding the detected type of variability identified in the TESS light curves.

3.1. High frequency pulsators: β Cep stars

Our sample contains five bright previously studied β Cep stars, i.e. HD 44743 (β CMa), HD 46328 (ζ^1 CMa), HD 50707 (15 CMa), HD 61068 (PT Pup) and HD 16582 (δ Cet). We reconfirm their variable behaviour, typical of the β Cep pulsators, see Fig. 4.

All the stars in this group have a low projected rotational velocity ($v \sin i \leq 30$ km s^{-1}). In addition, line profiles of metal lines in these stars are importantly affected by pulsational broadening, as indicated by the large $v_{\rm mac}/v \sin i$ ratio. Interestingly, as previously known, in all those targets from the list above for which we have multi-epoch spectroscopy we detect line-profile variability that could lead to the misinterpretation of the stars as single line spectroscopic binaries, while this variability actually comes from the effect of the pulsation. This highlights the importance of combining TESS photometry and spectroscopy when studying massive stars.

As indicated in the right panel of Fig. 3, the five β Cep stars are located well inside the low order p-mode instability domain (see also further notes in Sect. 4). They are found in the latter part of the MS, indicating considerable evolution beyond the ZAMS and their evolutionary masses range between approximately 9 and 14 $M_\odot$.

HD 44743 (B1 II-III) has three identified modes which allowed asteroseismic modelling (Shobbrook 1973a; Aerts et al. 1994; Shobbrook et al. 2006; Mazumdar et al. 2006). From the TESS data set we recover only two of these known pulsation modes, in addition to seven new frequencies. This includes the harmonic of the dominant pulsation frequency, four additional high frequency modes and two frequencies < 1 d^{-1} that we attribute to rotational modulation given that they are harmonics of one another. We measure no significant difference in the amplitude ratio of the two modes with respect to Shobbrook et al. (2006), implying that there have been no significant amplitude variations over time. We note an approximately 45% reduction in pulsation mode amplitude from the Stromgren v band to the redder TESS detector band-pass.

For HD 46328 (B0.5 IV) we extract a total of six frequencies from the one sector of TESS data (second row of Fig. 4). This includes five sub-harmonics/harmonics of the dominant frequency. This conforms to findings by McNamara (1955); Shobbrook (1973b); Heynderickx (1992); Heynderickx et al. (1994); Saesen et al. (2006); Shultz et al. (2017, 2018) for this high-amplitude mono-periodic β Cep star.

[6] Those cases labelled as SB1? are most likely binaries; however, our spectroscopic data set does not allow to clearly confirm its binary nature.

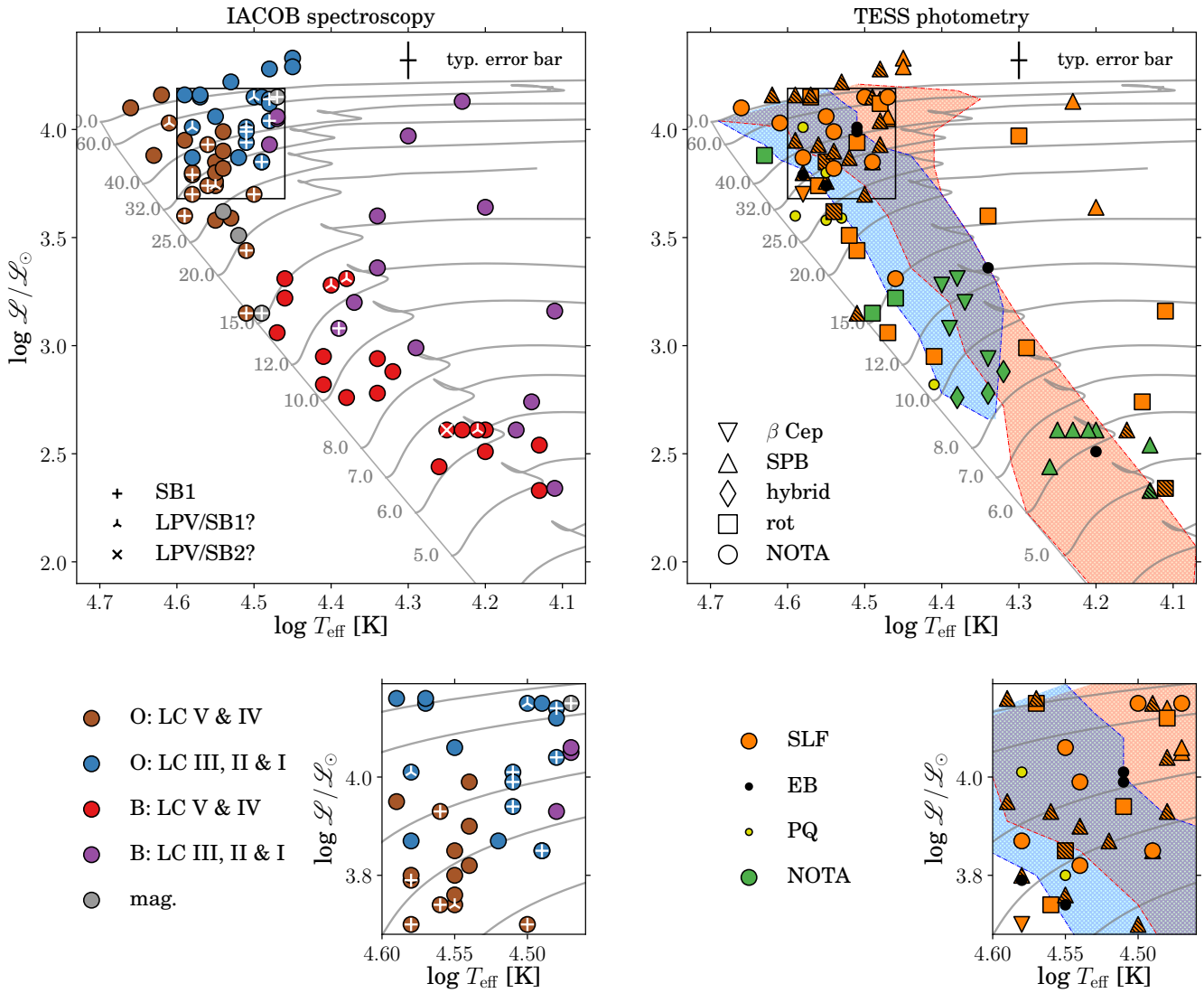

Fig. 3: sHRD including all the stars in our sample with determined spectroscopic parameters. On the left panels the stars are sorted following spectral classification criteria (see also Table 1). A zoom-in of the dense regions is marked by the black quadrant. Stars identified as single line spectroscopic binaries (SB1) or line profile variables due to the effect of pulsations (LPV/SB1? and LPV/SB2?) are highlighted. On the panels to the right the stars are sorted according to the information provided by the TESS photometric data. The different markers indicate different stable variability seen in the light curves. NOTA indicates "None Of The Above". Hatched symbols mark stars where the exact variability character of the star is uncertain. The colours indicates if the light curve shows stochastic low frequency variability or not (SLF/NOTA), eclipses (EB), or is of poor quality (PQ). Evolutionary tracks are given in grey on both sides. On the right we also plot the calculated instability strips, blue for the p-modes ($\ell = 0-2$) and orange for g-modes ($\ell = 1-2$).

For HD 50707 (B1 IV) we extract a total of 27 frequencies from the two sector TESS data set (third row of Fig. 4), including two harmonics of the dominant peak. The dominant frequencies conform to previous findings by Shobbrook (1973b); Heynderickx (1992); Shobbrook et al. (2006). We recover the radial mode and triplet measured by Shobbrook et al. (2006). Several other closely spaced higher frequencies ($6 < \nu < 10$ d^{-1}) are seen but none of them show similar frequency spacings. Interestingly, Shobbrook et al. (2006) find that their f_2 has changed in amplitude (ratio of the dominant peak over $A_1/A_2 \approx 1.4$ in Stromgren v), by comparing to the data in Shobbrook (1973b) (ratio of the dominant peak over $A_1/A_2 \approx 3.2$ in Johnson V). In our analysis we find $A_1/A_3 \approx 2.73$, almost twice the ratio in Shobbrook et al. (2006). The other frequencies show no significant variation in amplitude ratios. For the coherent modes we notice an approximately 26% reduction in amplitude from the Stromgren v band to the TESS detector band-pass. This is significantly different to the amplitude reduction measured in the other β Cep star in our sample that was studied by Shobbrook et al. (2006), HD 44743. This implies amplitude variations over time unconnected to the photometric instruments. These changes in amplitude ratios and the amplitudes themselves may point towards intrinsic non-linearity in the mode behaviour (see e.g. Degroote et al. 2009; Bowman et al. 2016), such as resonant coupling of pulsation modes (Dziembowski 1982; Buchler et al. 1995, 1997). We also mention the presence of significant frequencies

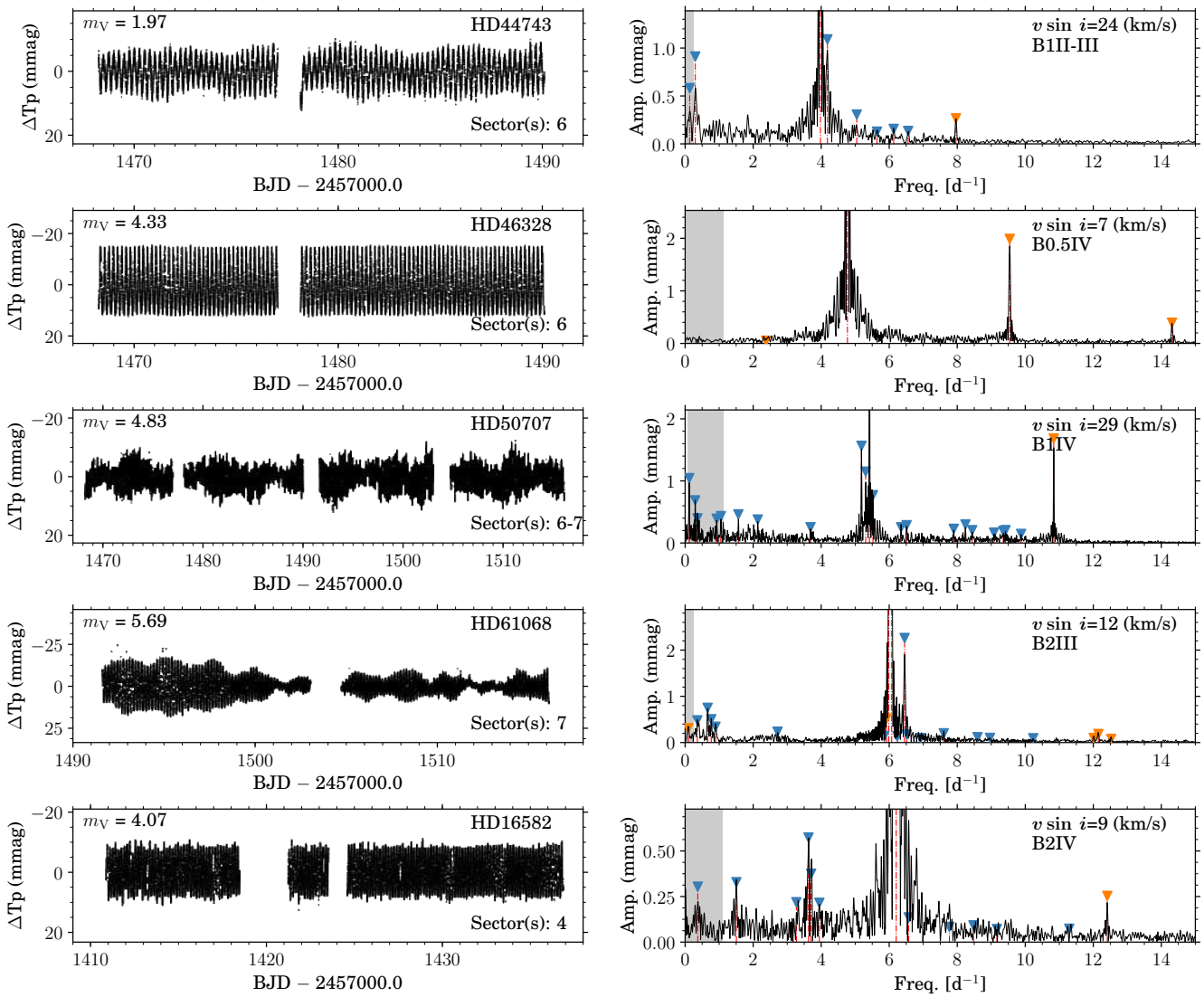

Fig. 4: The MS B-type stars showing coherent p mode pulsations. Light curves (*left panels*) and their corresponding LS-periodogram (*right panels*) for HD 44743 (β CMa), HD 46328 (ζ^1 CMa), HD 50707 (15 CMa), HD 61068 (PT Pup), HD 16582 (δ Cet). No significant variability is seen beyond 15 d^{-1}. The amplitudes in the LS-periodogram is cut-off at the second most significant peak to highlight the low amplitude frequencies. In HD 61068 we use the third most significant peak. We mark the extracted frequency peaks, with blue markers indicating frequencies satisfying our significance criterion. Orange markers indicated possible combinations/harmonics of the dominant frequency (in terms of amplitude) and second dominant frequency. The grey band indicates the approximate frequency range where the effects of rotation may be expected (see Section 2.3), calculated based on the v sin i and v = 450 km s^{-1}, if the radius corresponding to the spectral type and v sin i are available for that particular star.

outside the estimated rotation modulation range but still below 2.5 d^{-1}. This indicates that they are g modes and HD 50707 could be a possible hybrid pulsator.

HD 61068 (B2 III), also known as PT Pup, has two reported frequencies that vary in relative amplitude on long time scales (Lesh & Wesselius 1979; Shobbrook 1981; Heynderickx 1992; Maisonneuve 2011). We extract nineteen additional frequencies from the one sector TESS data set (fourth row of Fig. 4). This includes harmonics of the two dominant frequencies, additional high frequencies and a few frequencies below < 1 d^{-1}. It is unclear whether the latter are due to rotational modulation or heat-driven modes. The dominant frequencies measured in the TESS data are within 1σ of previous findings (fourth row of Fig. 4, on the right). The dominant frequencies ν_1 and ν_2 are of almost equal amplitude in contrast with previous findings. This amplitude variation may be related to beating effects given their close proximity. Heynderickx (1992) and Maisonneuve (2011) identified our $\nu_2 = 5.9875(6)$ d^{-1} as a non-radial mode, either $\ell = 1$ or 2. We identify two low amplitude frequencies, $\nu_5 = 5.922(1)$ and $\nu_{14} = 5.853(3)$ d^{-1} which could form a rotational multiplet with ν_2. A similar frequency spacing is seen between $\nu_3 = 6.4530(5)$ d^{-1} and low amplitude frequency $\nu_{13} = 6.520(3)$ d^{-1}. In the asymptotic regime (see i.e. Section 3.8 in Aerts et al. 2010) this could indicate of $P_{\rm rot} = 14 \pm 2$ d, which agrees with the measured low v sin i. However, after prewhitening the residuals still show many unresolved frequencies, which does not allow us to exclude the $\ell > 1$ scenario for both ν_2 and ν_3.

For HD 16582 (B2 IV), or δ Cet, we extract fourteen frequencies from the one sector TESS data set (fifth row of Fig. 4) including a high amplitude dominant frequency and two of its harmonics. This conforms to the history of observations of δ Cet (e.g McNamara 1953, 1955; Mohan 1981; Peters et al. 1987; Jerzykiewicz et al. 1988, see Stankov & Handler 2005 for an overview), which has long been considered monoperiodic. In a more recent investigation Aerts et al. (2006) detected an additional three frequencies (f_2 = 3.737(2), f_3 = 3.673(2) and f_4 = 0.318(2) d^{-1}) and the harmonic of the dominant frequency, using 18.7 d of MOST data. We measure ν_2 = 3.628(1) d^{-1} and ν_3 = 3.705(2) d^{-1} instead, indicating a significant decrease in frequency with time. The lower frequency g mode is not found by us in the TESS data but we do find a possible harmonic ν_4 = 1.507(2) d^{-1}. Pulsation periods of β Cep stars are known to decrease in frequency with time due to stellar evolution (see e.g Eggleton & Percy 1973; Jerzykiewicz 1999; Neilson & Ignace 2015). However, the frequency changes in ν_2 and ν_3 are much larger than those predicted by stellar evolution models on the short timescale of approximately 13 y (e.g Eggleton & Percy (1973); Neilson & Ignace (2015)). Conversely, we measure no difference within the frequency resolution between our measurement of the dominant frequency and the last measurement by Aerts et al. (2006), which is in line with period change estimates for δ Cet (Jerzykiewicz 1999). Follow-up measurements of ν_2 and ν_3 with high-precision photometry are necessary to verify the stability of these frequencies.

3.2. Low-frequency pulsators: SPB stars

In total there are five previously unknown SPB stars in our sample (HD 57539, HD 35912, HD 41753, HD 26912 and HD 37711), and one known (HD 48977). The TESS light curves and their periodograms are given in Fig. 5.

All these stars except HD 57539 are located inside the instability domain associated with high-order g modes (see right panel in Fig. 3, and further notes in Sect. 4). As in the case of the five β Cep in our working sample (Sect. 3.1), they are also found in the second part of the MS, but have lower evolutionary masses (approximately $6-7$ M$_\odot$).

We detected likely signatures of spectroscopic binarity in two of the stars (HD 37711 and HD 48977, labelled in Table 1 as LPV/SB1? and LPV/SB2?, respectively) although given the low number of available spectra, we cannot discard that the detected spectroscopic variability is produced by the SPB-type pulsations. We also note that three out of the six stars have a projected rotational velocity larger than 50 km s^{-1}. Interestingly, HD 57539 (the star which is located outside of our computed instability strip) has a much larger v sin i compared to the other five stars, and the main pulsation frequencies detected in its LS-periodogram are located at higher frequencies. We provide further notes about this (and the other 5 stars) below. Lastly, we do note that the macroturbulent broadening contribution (relative to the rotational broadening one) seems to be smaller in the SPB stars than in the case of the β Cep stars in our sample.

For HD 57539 (B3 IV) no variability was detected with ASAS-3 photometry (Frémat et al. 2006; Gutiérrez-Soto et al. 2007). We extract fifteen frequencies from the TESS data set (first row in Fig. 5). The low frequency regime shows residual variability after frequency extraction indicating that many more unresolved pulsation modes are still present. The dominant frequency group falls inside the estimated rotational modulation range indicating rotation could be partly responsible for the observed variability. Interestingly, the spectroscopic parameters of HD 57539 indicate it is highly evolved and thus falls outside the calculated instability strips (see also Section 4.1). This could be the effect of an extended MS due to fast rotation (see e.g. Brott et al. 2011), and hence an extended instability domain.

HD 35912 (B2 V) is known to be weakly magnetic (Bychkov et al. 2003) and using this property Bychkov et al. (2005) derived a rotation period of $P_{\rm rot}$ = 0.89786 d. We measure eleven frequencies in the one sector TESS data set (second row in Fig. 5). The fourth dominant frequency could correspond to the rotation period, ν_4 = 1.146(1) d. We note equal spacing between the four frequencies but they are unlikely part of the same rotational multiplet, given the rotation period derived by Bychkov et al. (2005) unless that the star exhibits strong differential radial rotation. We explain the frequencies as heat-driven g modes given the high amplitudes.

HD 41753 (B3 IV), is part of a binary system with a period of 131.2 d (Eggleton & Tokovinin 2008). We extract nineteen frequencies from the TESS data set (third row in Fig. 5) with two the dominant frequencies of significantly higher than the rest. Despite the large number of frequencies we do not detect any patterns/splittings that allow for mode identification. We attribute the variability to g modes ($0.5<\nu<2.5$) and rotational modulation (< 0.5 d^{-1}) given the estimated frequency range.

HD 48977 (B2.5 V) is a known spectroscopic binary (Karlsson 1969) and SPB star (Koen & Eyer 2002; Stankov & Handler 2005; Telting et al. 2006; Thoul et al. 2013; Bowman et al. 2019a). We extract eleven frequencies from the TESS data set (fourth row in Fig. 5), which is significantly less than in the CoRoT light curve (55, Thoul et al. 2013). The amplitude of the dominant frequency in the CoRoT light curve is A = 2025 ± 125 ppm (Thoul et al. 2013). We find an amplitude of A = 2582 ± 185 ppm (or 2.8(2) mmag). Since the TESS passband is redder than the one of CoRoT, one would expect smaller (of order 30%) pulsation amplitudes in OB-type stars observed by TESS compared to CoRoT. The similar CoRoT and TESS amplitude implies long-term amplitude modulation and beating among unresolved frequencies.

HD 26912 (B3 IV) was classified as a constant star by Percy & Lane (1977), however they only investigated short-term variability. We extract eighteen frequencies from the TESS data set (fifth row in Fig. 5). The dominant frequency has several possible (sub-)harmonics, but the other frequencies are independent. No patterns or multiplets are apparent inhibiting mode identification.

HD 37711 (B3 IV) is a known visual binary (Eggleton & Tokovinin 2008). We extract fifteen frequencies from the TESS data set (sixth row in Fig. 5), including several possible harmonics of the dominant frequency. Given the estimated rotational modulation range the observed variability is likely a combination of rotation and heat-driven g modes.

3.3. Hybrid pulsators

We identify in our sample three previously unknown hybrid pulsators among the MS B-type stars: HD 37303, HD 37481, and HD 37209. We show their light curves and LS-periodograms in Fig. 6. We do not plot the spectra as they are either single epoch or show no significant variability.

As expected, there are located in the region between the detected β Cep and SPB stars, with evolutionary masses in the range approximately $8-10$ M$_\odot$. HD 37303 has a relatively large projected rotational velocity ($v \sin i = 280$ km s^{-1}), while the other two have more moderated values of $v \sin i$ ($\approx 50-75$ km s^{-1}). Interestingly, the macroturbulent broadening contri-

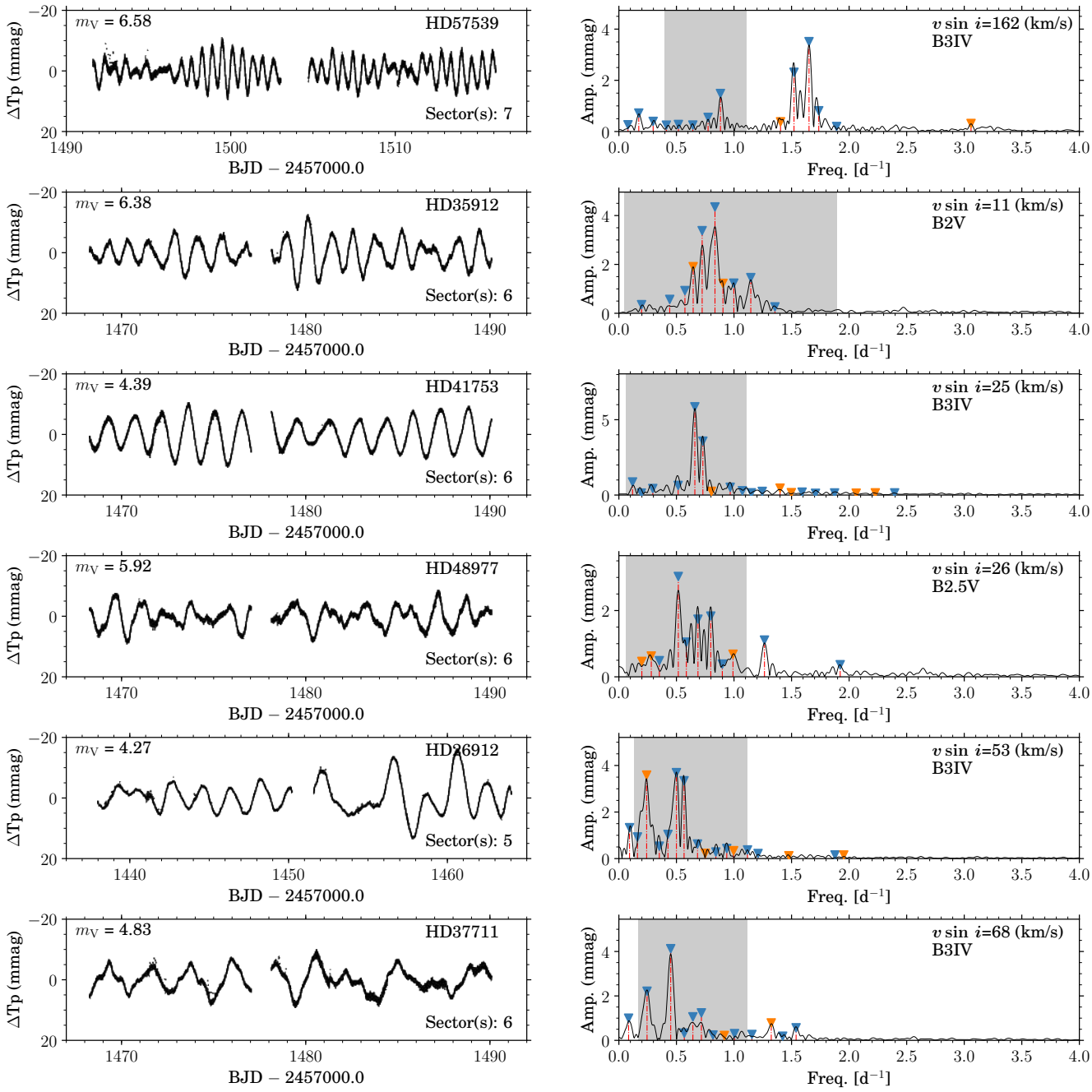

Fig. 5: Light curves (*left*) and their corresponding LS-periodograms for HD 57539, HD 35912, HD 41753, HD 48977, HD 26912 and HD 37711. No significant variability is seen beyond 4 d^{-1}. The markers in the LS-periodograms have the same meaning as in Fig. 4

bution (relative to the rotational broadening one) is small in these three stars.

HD 37303 (B1.5 V) is known to be variable on a short timescale (Percy & Lane 1977). It was considered SB2 by Morrell & Levato (1991a) but this could not be confirmed by Eggleton & Tokovinin (2008). We extract 48 frequencies (see the top row of Fig. 6, both in the low and high frequency regime. The dominant frequency is indicative of a young β Cep star. Many of the lower-amplitude frequencies are part of multiplets, see the clear quadruplets at approximately 8 and 10 d^{-1} and the sextuplet at 16 d^{-1}. They are not all equally spaced within each multiplet but two distinct spacings repeat: a larger one $\approx$ 0.24 – 0.30 d^{-1} and a smaller one $\approx$ 0.16 – 0.17 d^{-1}. The high rotational velocity ($v \sin i$=280 km s^{-1}) could be responsible for this pattern. The rich frequency spectrum and frequency spacing makes HD 37303 the most interesting hybrid candidate for future asteroseismic modelling, provided that the modes can be identified.

The variability of HD 37481 (B1.5 IV) has not been studied before. We extract sixteen frequencies (see middle row of Fig. 6), half of which in the low frequency regime (< 2 d^{-1}), making HD 37481 a hybrid pulsator. The low frequencies form a triplet: ν_1 = 1.1052(8), ν_2 = 1.260(1), and ν_4 = 1.432(1) d^{-1}. A possible triplet is also seen in the high frequency regime: ν_{14} = 8.125(3), ν_{12} = 8.246(2), and ν_5 = 8.346(2) d^{-1}, with a slightly smaller

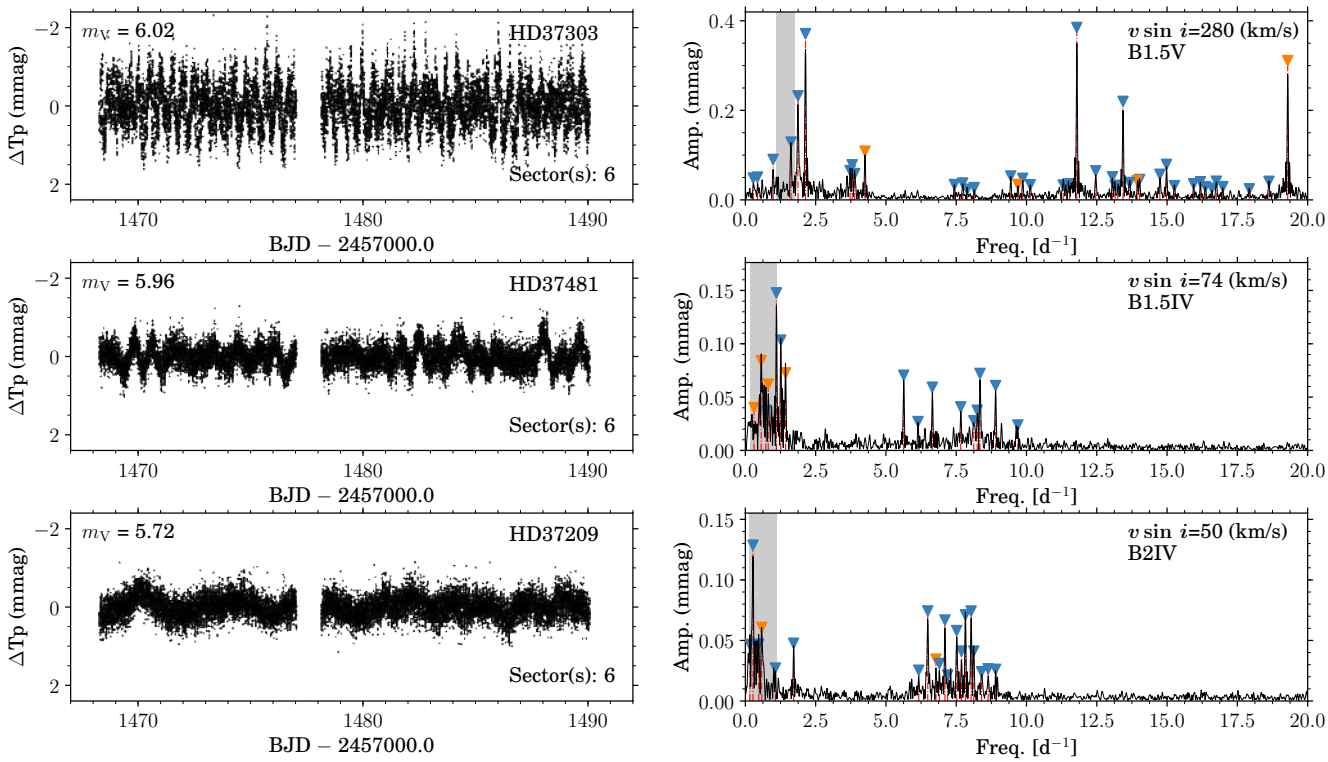

Fig. 6: Light curves (*left*) and their corresponding LS-periodogram (*right*) for HD 37303, HD 37481, and HD 37209. The markers in the LS-periodograms have the same meaning as in Fig. 4.

average spacing, ≈ 0.16 vs. 0.11 d^{-1}. If these are rotational multiplets this would imply a slightly faster rotation in the envelope than the core, assuming they are heat-driven g and p modes respectively. However the presence of (unresolved) residual variability does not allow us to conclude unambiguously that these are in fact rotational triplets. Before mode identification is possible, more photometric data is required to deduce additional significant frequencies.

HD 37209 (B2 IV) was suspected to be variable on a short time scale by Percy & Lane (1977). We extract twenty frequencies from the TESS data set across the low and high frequency regime (see bottom row of Fig. 6). Based on our estimated frequency range (the grey area in the bottom right panel Fig. 6), it is possible that the dominant low frequency variability is due to rotational modulation. However the presence of additional low frequency peaks is indicative of heat-driven g modes. The high frequencies are part of a frequency group, and the residuals indicate more variability is present. HD 37209 is clearly a hybrid pulsator but despite the high number of significant frequencies we identify no patterns or splittings.

3.4. Peculiar stars

3.4.1. Be and Oe stars

One Be star and two Oe stars are included in our sample: HD 58978, HD 39680, and HD 45314. The TESS LS-periodograms, and the He I λ5875 and H$_\alpha$ lines are given in Fig. 7, in the left and right panels respectively.

HD 58978 (FY CMa, B0 IV:e) is a Be star with a hot sdO sub-dwarf companion (Rivinius et al. 2004; Peters et al. 2008) with low frequency (< 0.38 d^{-1}) periodicities in HIPPARCOS photometry (Lefèvre et al. 2009). We extract 30 frequencies from the one sector TESS data set, none of which have been previously reported. Distinct frequency groups are seen, typical of pulsating highly non-linear pulsating Be stars (e.g. Kurtz et al. 2015). We plot the TESS LS-periodogram in Fig. 7 (first row), along with the HeI λ5875 and the H$_\alpha$ lines for two epochs separated over two years. H$_\alpha$ shows variable double-peaked emission over both epochs, suggesting a disk, while HeI λ5875 shows clear line-profile variations. The lines are very broad making the star a fast rotator which is common in observed Be stars. In the case of FY CMa the fast rotation is a result of the past mass transfer spin-up (Peters et al. 2008). It remains to be seen what the variability contribution of the subdwarf O-type star is, given that OB subdwarfs are known to exhibit heat-driven p modes (Charpinet et al. 1997; Kilkenny 2007; Randall et al. 2016). The origin of the dominant variability is still likely from the Be star given that the light contribution of the subdwarf O star is approximately two orders of magnitude lower (Peters et al. 2008). We do not detect any patterns or spacings but the discovery of a large number of high frequency modes makes HD 58978 an interesting candidate to model. That is, if the modes can be identified which in the case of this emission-line star is likely only possible with additional continuous photometry.

HD 39680 (O6 V:[n]pevar) is a known emission-line star (Conti & Leep 1974; Frost & Conti 1976; Negueruela et al. 2004; Sota et al. 2011). This emission is also seen in the multi-epoch IACOB spectroscopy, as shown in the top right in Fig. 7. Both He I λ5875 and H$_\alpha$ reveal double peak emission, which is variable over the five randomly selected epochs in the available spectroscopic data set. We extract three frequencies from the one sector TESS data set, but additional residual variability is still clearly visible. The lowest frequency peak could be due to ro-

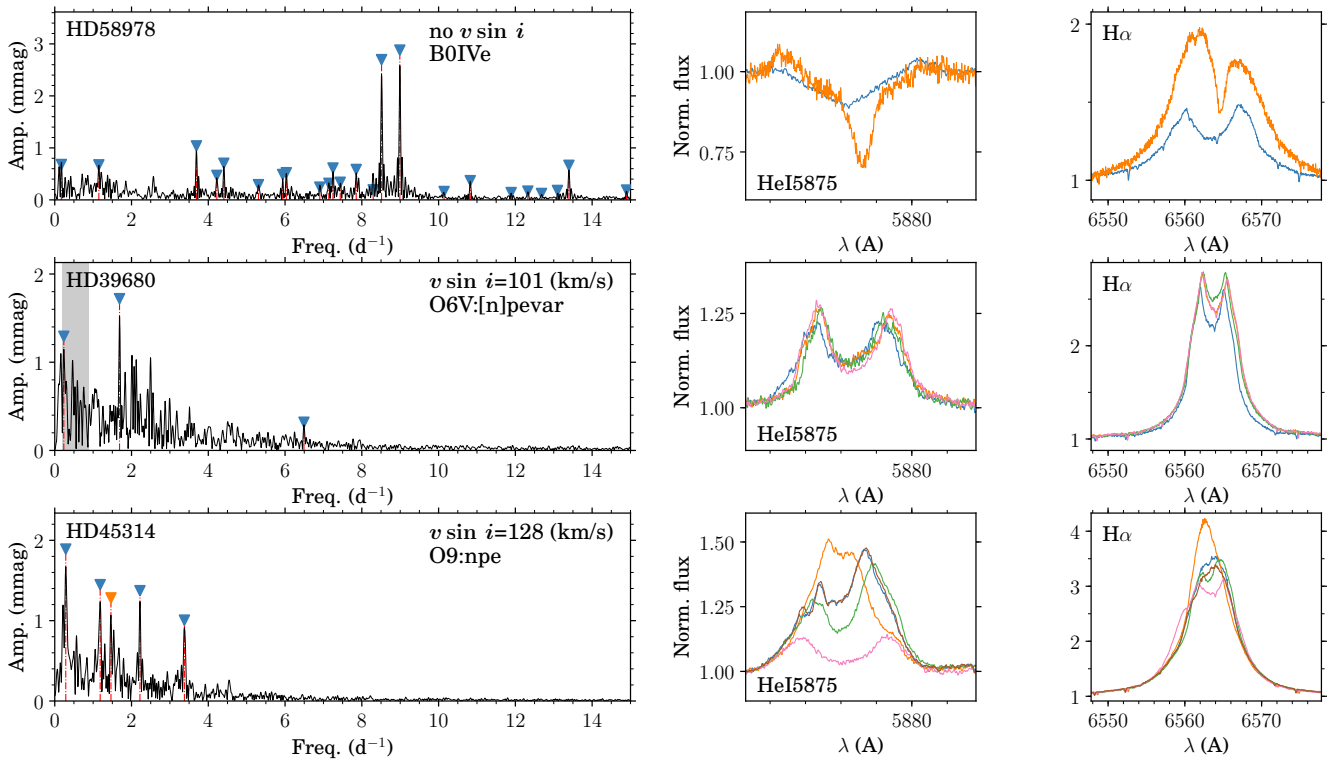

Fig. 7: LS-periodogram up to 15 d^{-1} (*left*) and two spectroscopic lines (*right*, He I λ5875 and H$_\alpha$) for five epochs from days to months to a year, for emission-line stars HD 58978, HD 39680, and HD 45314.

tational modulation but the large presence of variability outside the estimated grey frequency range in Fig. 7 indicates the presence of heat-driven g modes. The dense frequency groupings are reminiscent of those seen in pulsating Be stars (i.e. Huat et al. 2009).

HD 45314 (O9: npe) is classified in the literature as a γ Cas star because of its unusually hard and bright X-ray emission (Rauw et al. 2013, 2018). We extract five frequencies from the one sector TESS data set, and additional residual variability remains visible in the low frequency region (< 5 d^{-1}, see bottom row Fig. 7). Both He I λ5875 and H$_\alpha$ are seen in emission, transitioning between single and multi-peaked which was also seen by Rauw et al. (2018).

3.4.2. Magnetic O- and B-type stars

We have identified stars distributed across the whole spectroscopic HR diagram whose TESS light curves show signatures that could be associated with rotational modulation (see square symbols in the right panel of Fig. 3). In this section we briefly discuss those stars known to be magnetic that should contain strong contributions of rotational modulation in their LS-periodogram. An example where rotational modulation likely caused by stellar wind is discussed in Section 3.7.

We have six stars with a clear magnetic field detection in the literature; namely, HD 37061 (Shultz et al. 2019), HD 57682 (Grunhut et al. 2009, 2012), HD 54879 (Castro et al. 2015; Shenar et al. 2017; Hubrig et al. 2019), HD 37022 (Donati et al. 2002; Wade et al. 2006), HD 37742 (Bouret et al. 2008; Blazère et al. 2015), and HD 37479 (Landstreet & Borra 1978; Oksala et al. 2012). In all LS-periodograms dominant singular frequencies are visible in the low frequency regime (ranging between

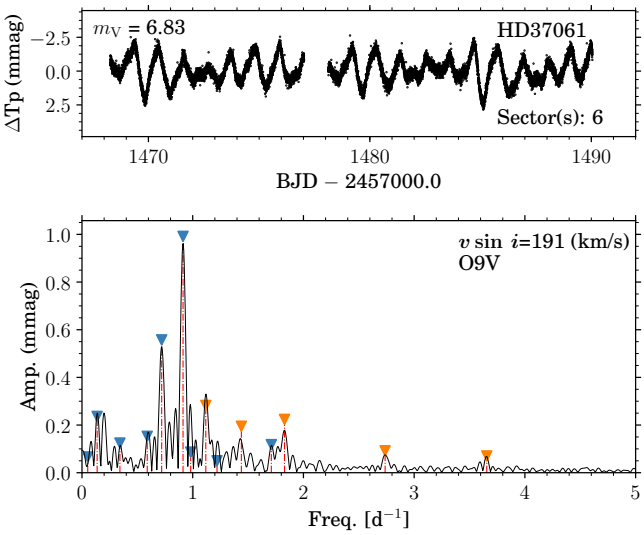

Fig. 8: Light curve (*Top*) and LS-periodogram (*Bottom*) of HD 37061, or NU Ori. The markers in the LS-periodogram have the same meaning as in Fig. 4

0.31 and 1.67 d^{-1}, with amplitudes between 0.11 and 6.6 mmag). These are likely linked to spots induced by large magnetic fields on the surface that cause brightness variations due to rotation of the star (David-Uraz et al. 2019). The dominant frequencies are therefore thought to be the rotation frequency or a (sub-)harmonic thereof. This is in agreement with the predicted frequency ranges based on the v sin i.

We show an example in Fig. 8, where we present the light curve and periodogram of HD 37061 (O9 V), or NU Ori. NU Ori is a massive binary system with four known components: a spectroscopic inner binary Aa and Ab (Abt et al. 1991; Morrell & Levato 1991b), and visual binary components B and C (Köhler et al. 2006; Grellmann et al. 2013). Given the large TESS pixel size all components are present in the mask (separation < 1 arcsecond), and hence in the extracted light curve. The measured large-scale magnetic field of ≈ 8 kG was though to originate from the primary Aa by Petit et al. (2008) but this was contested by Shultz et al. (2019), who show that it is the C component instead. We extract 14 frequencies, many of which are combinations/harmonics of the first and second dominant frequency. The dominant frequency $\nu_1 = 0.9126(4)$ d^{-1} is consistent with the rotational period $P_{\rm rot} = 1.09468(7)$ d measured from the recent magnetic field measurements by Shultz et al. (2019) for NU Ori C. Interestingly, ν_1 is the central frequency of a triplet: 0.7197(5), 0.9126(4), 1.1183(9) d^{-1}, with an average splitting of $\Delta\nu = 0.1994(6)$ d^{-1}. This could be the result of an inclination effect ($i_{\rm rot} = 38 \pm 5°$, Shultz et al. 2019) but this cannot be confirmed given the available data. This example illustrates that even a single sector TESS data set can be promising in studying the variability in magnetic OB-type stars as is clear from recent studies on magnetic A and B-type stars (David-Uraz et al. 2019; Sikora et al. 2019), but also magnetic O-type stars (Barron et al. 2020).

3.5. Binaries

We find nine eclipsing binaries in our sample (see last column in Table 1), including three new systems. Seven systems including one or two O-type stars and another two including one or two B-type components. All of them have also been identified as SB1 or SB2 systems by means of the available spectroscopy. These EB systems imply about one third of the total sample of spectroscopic binaries comprising our working sample. As the focus of this paper is on the intrinsic variability of OB-type stars we only discuss the newly eclipsing systems shortly: HD 159176, HD 46485 and HD 23466. Their TESS light curves, and LS-periodograms are given in Fig. 9.

The light curve of HD 159176 (O7 V((f)) + O7 V((f)), top row on the left of Fig. 9) shows complex behaviour with ellipsoidal variations which have been reported in the past (Thomas 1975; Linder et al. 2007). The dominant frequency $\nu = 0.5929(5)$ d^{-1} (on the right of top row in Fig. 9) is due to the binary orbit. The second dominant frequency, $\nu_2 = 1.1200(6)$ d^{-1} is not a harmonic of the first but rather the ellipsoidal variation seen in the light curve. All higher amplitude frequency peaks are harmonics of ν_1 and ν_2, however low amplitude combination frequencies of the form $n\nu_1 \pm m\nu_2$ are also seen. Low frequency variability remains in the residuals after peak extraction. The complex variability may also partially come from the complex wind-wind interaction observed for HD 159176 (De Becker et al. 2004), but we do not find signature of emission in the H_α line in any of the two components.

The binarity of HD 46485 (O7 V((f))nz var?) has remained unconfirmed (Sana et al. 2014; Cazorla et al. 2017). We only see lines from one of the components in our spectra, these lines being very broad ($v \sin i = 320$ km s^{-1}) The light curve (middle row of Fig. 9) shows clear ellipsoidal variability. We extract the dominant frequency, $\nu = 0.1451(4)$ d, and many of its harmonics. After removing all (sub-)harmonics some variability remains in the periodogram, which could be related to rotational modulation of one of the components ($v \sin i$ of 320 km s^{-1}) given the expected frequency range

HD 23466 (B3 V) is a known spectroscopic binary (Pourbaix et al. 2004; Eggleton & Tokovinin 2008). We only see lines from one of the components in our spectra but we cannot discard the star to be a SB2 since we have only epoch available for this star. We find in the LS-periodogram a dominant frequency of $\nu = 0.405(1)$ d^{-1}, which is due to the ellipsoidal variation, and a second dominant frequency that corresponds to the binary orbit $\nu_2 = 0.466(2)$ d^{-1}. Moreover, long time-scale variability occurs in between these eclipses, that could either be a third component or pulsations. However, after pre-whitening all harmonics of the dominant frequencies the residual frequencies are largely unresolved.

While it is beyond the scope of this paper to discuss in more detail other individual systems labelled as EB, we highlight here results we consider of interest for further investigation. Only one of the nine stars detected as EB by TESS has been found to be a clear double line spectroscopic binary. The other eight are interesting candidates to be massive star binaries including a OB-type star and compact object companion[7] (Langer et al. subm.) and likely progenitors of gravitational wave emitters (de Mink & Belczynski 2015).

3.6. Upper-main sequence stars

As illustrated in Fig. 3, most of the stars in our sample identified as *classical* β Cep, SPB and hybrid pulsators are located on the MS below the 15 $M_\odot$ evolutionary tracks, and are mostly classified as B-type dwarfs, subgiants or giants. In this section, we concentrate on the top right part of the sHRD, comprising MS stars with masses above ∼20 $M_\odot$ and including all O-type stars of different luminosity classes and two early B-type supergiants (HD 37128 and HD 38771).

Out of the 56 O-type stars and early B-type supergiants not labelled as magnetic or Oe stars, six light curves are either contaminated by nearby stars, saturated or showed signs of instrumental systematics, and seven show clear binary eclipses (see Sect. 3.5). In all (but one) of the remaining 42 TESS light curves, we detect signatures of stochastic low-frequency variability (similar to e.g Ramiaramanantsoa et al. 2018; Bowman et al. 2019a,b; Pedersen et al. 2019) and, similarly to the K2 sample of OB stars studied by Bowman et al. (2019b), frequency peaks which could be associated with coherent SPB pulsation modes and/or rotational modulation are seen in some of them (see examples in Fig. 11).

We provide below some more extended comments about some of these stars. However, before entering into details, we stress that the interpretation and analysis of the light curves of O-type stars and B supergiants is more complex than in the case of MS B-type stars due to the following facts:

- Even discarding SB2 and EB systems, large percentage of the O-type stars in our sample have been identified as SB1. Despite that the companion must be faint, we cannot discard some type of contamination by this lower mass companion in the light curve. This is the case, for example of HD 47839 (15 Mon), one of the O-type stars traditionally used as standard for spectral classification (defining the O7 V spectral class), but which is know to be part of a long period binary system (∼25 years, Gies et al. 1994) including a fast rotating B-type star companion. Despite this faint companion is barely detected even in our high-quality spectra, a

[7] If the presence of a faint lower mass star companion can be discarded.

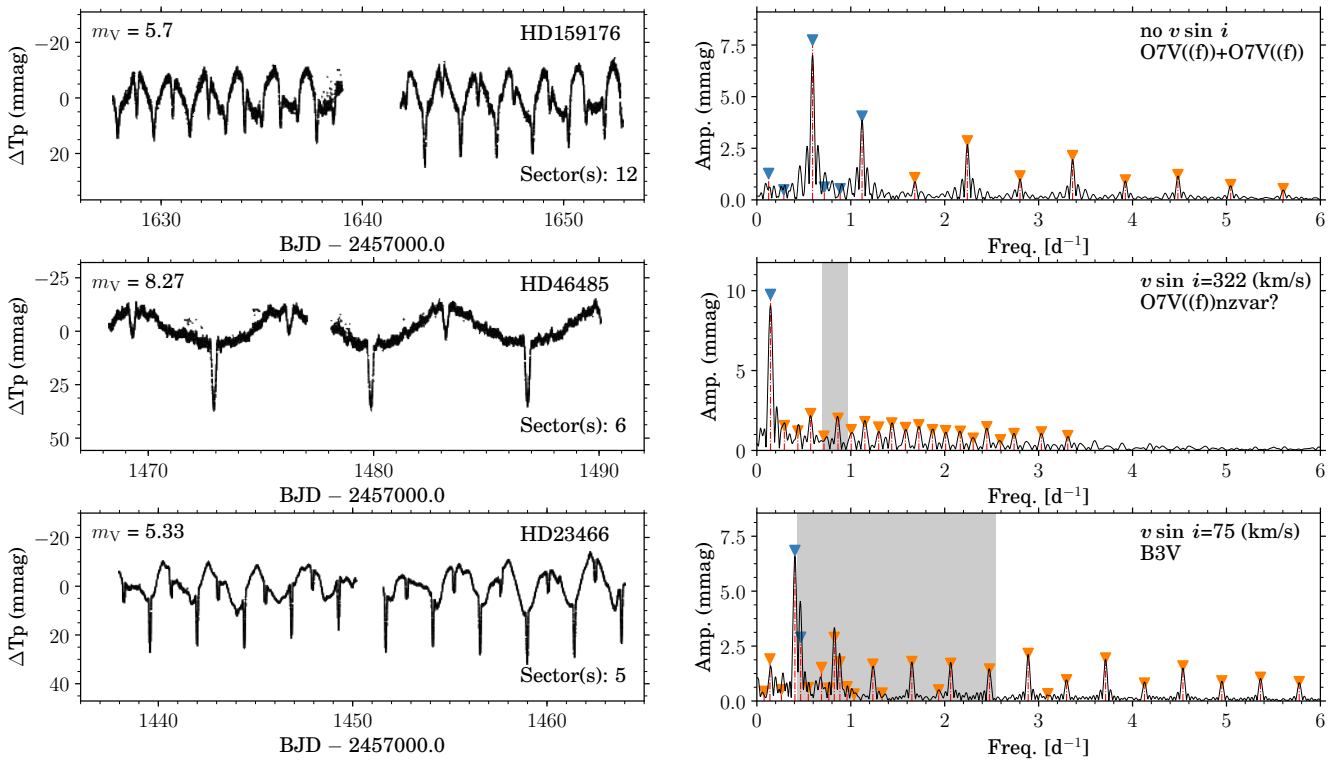

Fig. 9: TESS light curve, and LS-periodogram for newly found eclipsing binaries, HD 159176, HD 46485 and HD 23466. The markers in the LS-periodogram have the same meaning as in Fig. 4.

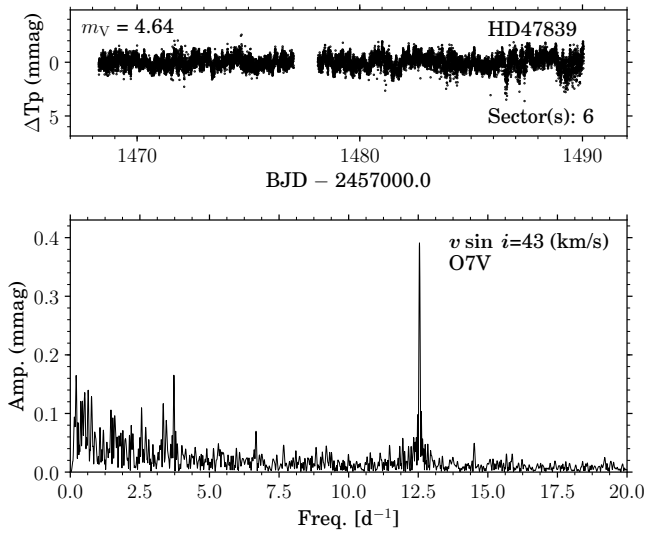

Fig. 10: Light curve (*Top*) and LS-periodogram (*Bottom*) of HD 47839, or 15 Mon. The markers in the LS-periodogram have the same meaning as in Fig. 4.

group of high-frequency peaks clearly stands out in the LS-periodogram which likely corresponds to the B-type companion and not the bright O7 V star (see Fig. 10). In these regards, we note that up 40% (11%) of the O-type stars in our sample have been identified as SB1 (SB2) systems.

– Part of the detected low-frequency variability could be in part be associated with different types of wind variability. O-type stars and luminous B supergiants can develop strong winds which leave their imprints in the H_α (and some other) lines. As illustrated in Fig. 11, and quoted in Table 1, many of the O- and early B-type supergiants show a varying H_α line in emission, hence implying that the wind is intrinsically varying on time-scales similar to g modes and/or the existence of large-scale, co-rotating wind structures. These phenomena are expected to leave signatures in the low frequency part of the LS-periodograms.

– Some of the stars not labelled as spectroscopic binaries may actually be and we have not detected them using our spectroscopic dataset (see, e.g., HD 97253 below).

Having this in mind, we now discuss some illustrative examples of the type of variability detected in these type of stars below: HD 97253, HD 151804, HD 3034925, HD 37128, HD 38771 (Fig. 11).

HD 97253 is a O5III(f) star (Sota et al. 2014) and a known spectroscopic binary (Gies 1987; Mason et al. 2009; Chini et al. 2012; Sana et al. 2014). The TESS light curve is clearly multiperiodic and we extract four frequencies. Additional (unresolved) variability is clearly still present in the residuals. In addition, the variability is not constrained to the estimated rotational modulation range, indicating that pulsational variability plays a significant role.

HD 151804 is an O8Iaf star (Sota et al. 2014) with a variable wind (Fullerton et al. 1992; Prinja et al. 1996; Crowther & Bohannan 1997). Fifteen frequencies are extracted from the TESS data set, including several (sub-)harmonics of the dominant frequency (see middle row of Fig. 11). If the dominant frequency and its (sub-)harmonics are related to the rotational wind variation, then the other frequencies are likely pulsation

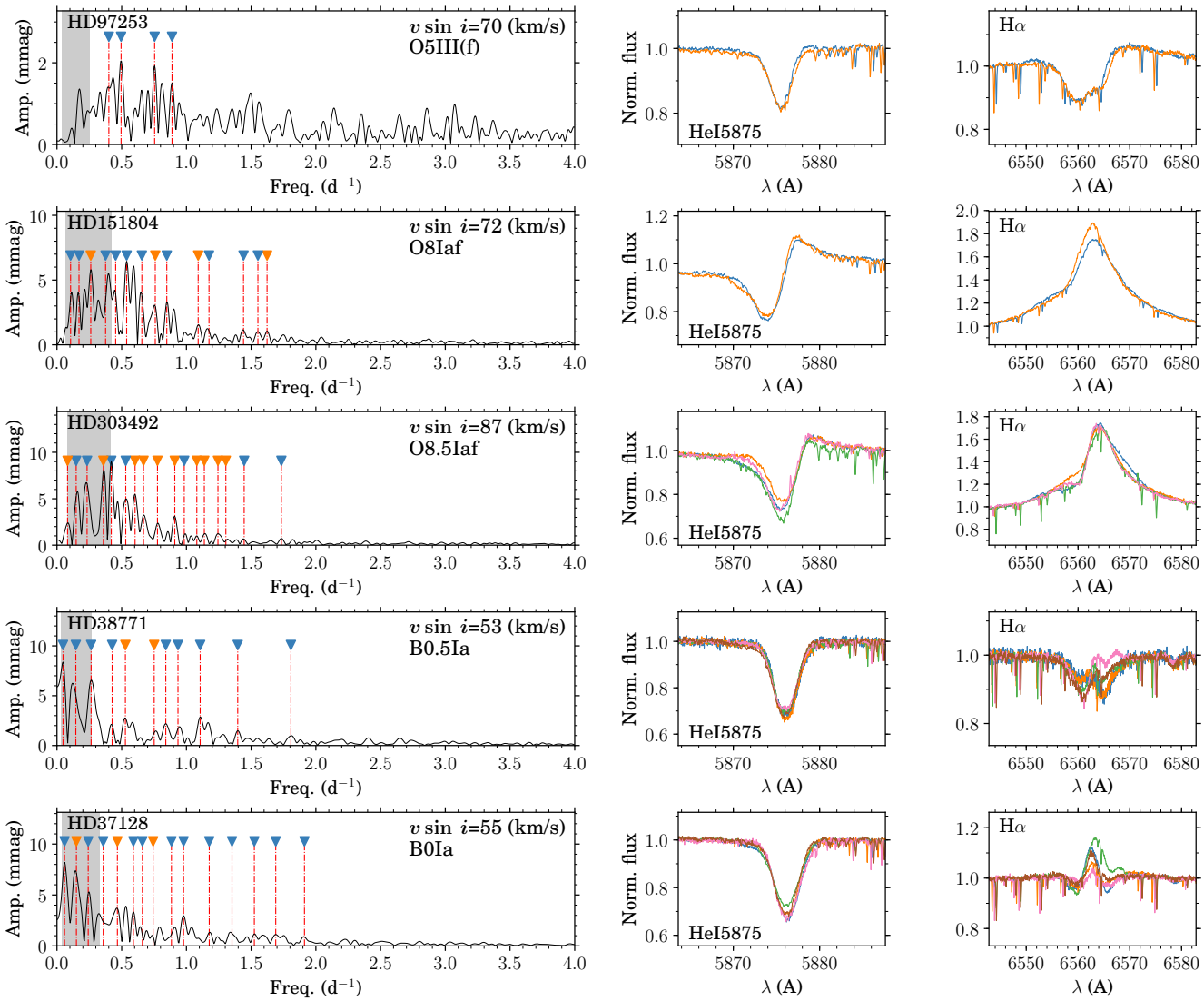

Fig. 11: TESS light curves and LS-periodograms for upper-MS stars, HD 97253, HD 151804, HD 303492, HD 38771 and HD 37128. The markers in the LS-periodogram have the same meaning as in Fig. 4. Due to the high density of frequencies the markers are placed at the same level in each individual star for clarity.

modes. However no frequency/period patterns are apparent making mode identification impossible given the current available data.

HD 303492 is an O8.5Iaf star (Sota et al. 2014) and known visual binary (Sana et al. 2014). Seventeen frequencies are extracted from the one sector TESS data set, many of which are combinations of the three dominant frequencies (bottom row of Fig. 11). The high mode density makes it difficult to conclude whether these are real or chance matches due to the limited frequency resolution. Three frequencies form a potential triplet: $\nu_7 = 0.531(2), \nu_4 = 0.603(2)$ and $\nu_6 = 0.669(1)$ d^{-1}. In addition, a frequency approximately matching this splitting is measured: $\nu_9 = 0.0817(9)$ d^{-1}. However, two members are potential low order combinations, making the rotational multiplet interpretation uncertain.

HD 37128, also known as ϵ Ori, has a variable wind (Blomme et al. 2002; Prinja et al. 2004; Crowther et al. 2006; David-Uraz et al. 2014; Puebla et al. 2016; Krtička & Feldmeier 2018). The LS-periodogram shows clear stochastic low frequency variability up to 5 d^{-1}, and we extract fifteen frequencies (top row in Fig. 12), including several possible combination frequencies. Given the estimated rotational modulation frequency range, the dominant frequency (ν_1=0.059(2) d^{-1}) could be related to rotation. The low value of the dominant frequency and the limited frequency resolution make it difficult to assess the true amount of combinations, as many could be due to chance. H$_\alpha$ shows variable emission in all (randomly selected) spectroscopic epochs, showing either a variable wind or a static wind combined with rotation. The HeI λ5875 line shows line profile variability, that is likely to have a similar origin as the variability in the photometry. This line is formed partially in the wind such that we can expect the stellar wind of ϵ Ori to play a significant role in its variability, much like in B1Ia star HD 2905 (Simón-Díaz et al. 2018), and in O9.5Iab star HD 188209, although to a lesser extent (Aerts et al. 2017a). The low-frequency variability in photometry outside of the grey region in Fig. 12 cannot be caused by rotational modulation, and has been inferred

to be caused by IGWs in OB-type stars (Blomme et al. 2011; Aerts & Rogers 2015; Bowman et al. 2019a,b).

HD 38771, also known as κ Ori, has a variable wind (Haucke et al. 2018, and references therein). We extract eleven frequencies, of which two harmonics of the second dominant frequency (second row of Fig. 12). Several of the measured frequencies correspond to previously measured periodicities. Prinja et al. (2004) find three spectroscopic periodicities of which we recover two: $f \approx 0.53$ d^{-1} which we find as a harmonic of the second dominant frequency ($\nu_2 = 0.264(2)$ d^{-1}), and $f \approx 0.154$ d^{-1} which could be our $\nu_3 = 0.146(2)$ d^{-1}. Morel et al. (2004) finds two photometric periodicities, $f \approx 0.21$ and $f \approx 0.96$ d^{-1}. The latter could be the same frequency as our $\nu_7 = 0.935(3)$ d^{-1}. However it remains difficult to conclude that these are in fact stable coherent pulsation modes given the limited frequency resolution. The dominant variability in the photometry could also be partly or fully stochastic in nature, i.e. a combination of IGWs with a stellar wind.

3.7. Post-main sequence stars

There are nine stars (all of them classified as B-type and luminosity class I or II) located beyond the MS[8], see Fig. 3: HD 54764, HD 53138, HD 51309, HD 46769, HD 53244, HD 27563, HD 57539, HD 39985, HD 52059. All of them (except one, HD 57539, the SPB star with a $v \sin i = 160$ km s^{-1}, see notes about this star in Sect. 3.2) exhibit stochastic low-frequency variability in the LS-periodograms (see some examples in Fig. 12). In addition, we extract one or multiple frequencies which could be associated with SPB-type coherent modes and/or rotational modulation. We discuss three examples where multiperiodicity is clear (HD 53138, HD 51309, HD 27563) and one where stellar rotation/wind is likely responsible for the variability (HD 46769).

HD 53138 (B3Iab), also known as o^2 CMa is a B3Ia supergiant with known irregular variations in the H_α line with periods between 4 and 45 d (Morel et al. 2004; Lefever et al. 2007; Haucke et al. 2018). Photometric variability is now seen in o^2 CMa as a stochastic low frequency variability < 2 d^{-1} (third row of Fig. 12). We extract 13 frequencies from the one sector TESS data set, two of which are likely harmonics of the dominant frequency. Two of these are approximately equal to the HIPPARCOS periodicities found by Lefever et al. (2007): our $\nu_7 = 0.0412(8)$ d^{-1} corresponds to their $f_1 \approx 0.041$ d^{-1}, and our $\nu_2 = 2\nu_1 = 0.250(1)$ d^{-1} could also be consistent with their $f_2 \approx 0.27$ d^{-1}. Note that the amplitudes are $1-2$ orders of magnitude lower between the TESS and HIPPARCOS data sets. A potential rotational quintuplet is seen: 0.250(1), 0.339(1), 0.436(1), 0.5111(8), 0.608(1) d^{-1} but given that two members are found as harmonics of the dominant frequency this is unlikely.

HD 51309 (B3II), also known as ι CMa, is known to be variable, and considered a possible SPB supergiant (Balona & Engelbrecht 1985; Stankov & Handler 2005; Saio et al. 2006). We extract 30 frequencies from the two sector TESS data set (third row of Fig. 12). A few possible combination frequencies are found but their interpretation is complicated by the limited frequency resolution. Our frequency $\nu_{14} = 0.756(1)$ d^{-1} could be related to the periodicity measured by Balona & Engelbrecht (1985), i.e. $\nu \approx 0.717$ d^{-1}. The frequencies are likely of pulsational origin, given that the degree of wind variability seen in the spectroscopic lines is small (but not insignificant). Balona & Engelbrecht (1985) also noted the irregular variations on a timescale longer than this periodicity, which is confirmed here.

HD 27563 (B7II) has known variability with a measured period of 4 d by Mathys et al. (1986) who classified it as multi-periodic or pseudo-periodic. Using additional data Manfroid (1989) suggested multi-periodicity is present. We extract fifteen frequencies from the TESS data set (fourth row of Fig. 12). The dominant frequency $\nu = 0.248(1)$ d^{-1} conforms to the period detected by Mathys et al. (1986), and has two harmonics. The presence of additional frequencies in the TESS data set confirms the suggestion by Manfroid (1989). However, given the low frequency resolution and low amplitudes it remains difficult to disentangle the contributions of the stochastic low frequency variability and the heat-driven pulsations.

HD 46769 (B5II) was studied in-depth by Aerts et al. (2013) using 23 d of CoRoT, detecting a dominant period of 4.84 d and several (sub-)harmonics. No significant variability was found in the residuals, and the variability was therefore explained as due to rotational modulation instead of pulsations. A low frequency power excess was measured by Bowman et al. (2019a) in the same data set, that was interpreted as granulation from sub-surface convection or internal gravity waves. Our measurements conform to these results within the frequency resolution: we extract five frequencies, all (sub-)harmonics of the dominant frequency $\nu_1 = 0.2249(8)$ d^{-1}.

As a final note in this section, we remind that the low number of B-type post-MS stars in our sample is just a consequence of the availability in our spectroscopic database of stars of this type located in the Southern hemisphere (see further notes in Sect. 3). The density of targets in this region is envisaged to considerably increase in further studies considering stars in the Northern TESS sectors. See, e.g. the number of B-type post-MS stars surveyed by the IACOB project in Simón-Díaz et al. (2017).

4. Discussion

Despite the relatively short data sets that hinder mode identification, the TESS data is sufficient to characterise different types of pulsation variability. When combined with high-resolution spectroscopy such as the one from the IACOB and OWN surveys there is potential to assess stellar variability over a large mass and evolutionary range. In a first instance we compare the variable stars to theoretical instability strips calculated for early-type stars. In a second instance we explore how the variability changes of evolutionary state from main sequence O-type stars to more evolved B-type supergiants.

4.1. Variables in the instability strip

We computed non-rotating evolutionary tracks and instability strips for three metallicities: $Z_{\rm ini} = 0.010, 0.014, 0.020$. In the case of heat-driven pulsators, increasing the iron-group abundances increases the opacity, which also increases the driving of modes (Gautschy & Saio 1993; Dziembowski & Pamiatnykh 1993; Dziembowski et al. 1993). As such, the excitation of modes is very sensitive to the heavy element abundance. Overall, our instability strips conform to those in the literature (Pamyatnykh 1999; Saio et al. 2006; Miglio et al. 2007; Walczak et al. 2015; Paxton et al. 2015; Godart et al. 2017). In Fig. 13 we compare the observed positions of the multiperiodic pulsators discussed in Sections 3.1, 3.2, and 3.3 to the computed instability strips.

[8] As resulting from our evolutionary model computations. The location of the TAMS is very sensitive to the input parameters of the stellar model: metallicity, overshooting and rotation.

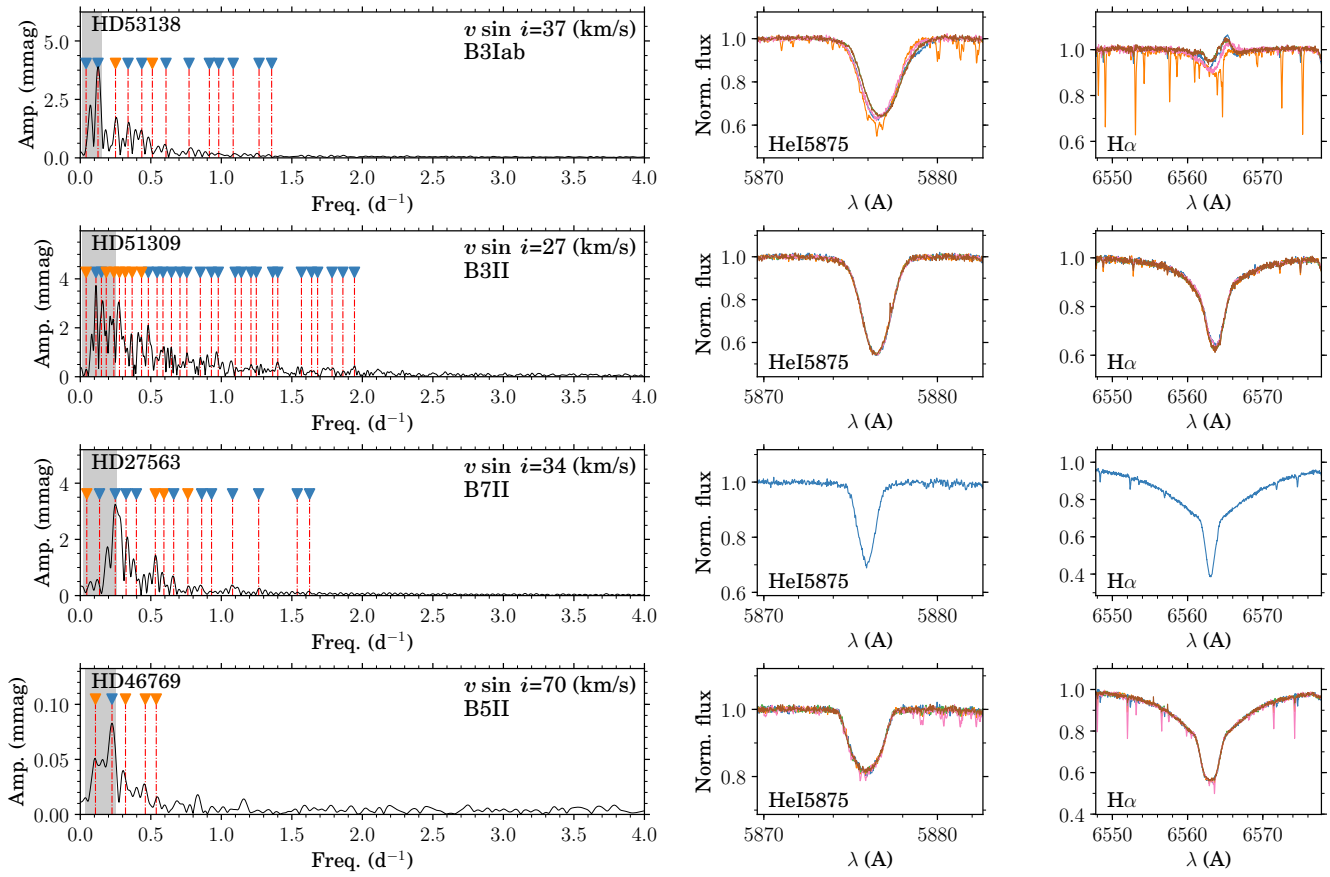

Fig. 12: TESS light curves and two spectroscopic lines for post-MS stars, HD 53138, HD 51309, HD 27563 and HD 46769. The markers in the LS-periodogram have the same meaning as in Fig. 4. Due to the high density of frequencies the markers are placed at the same level in each individual star for clarity.

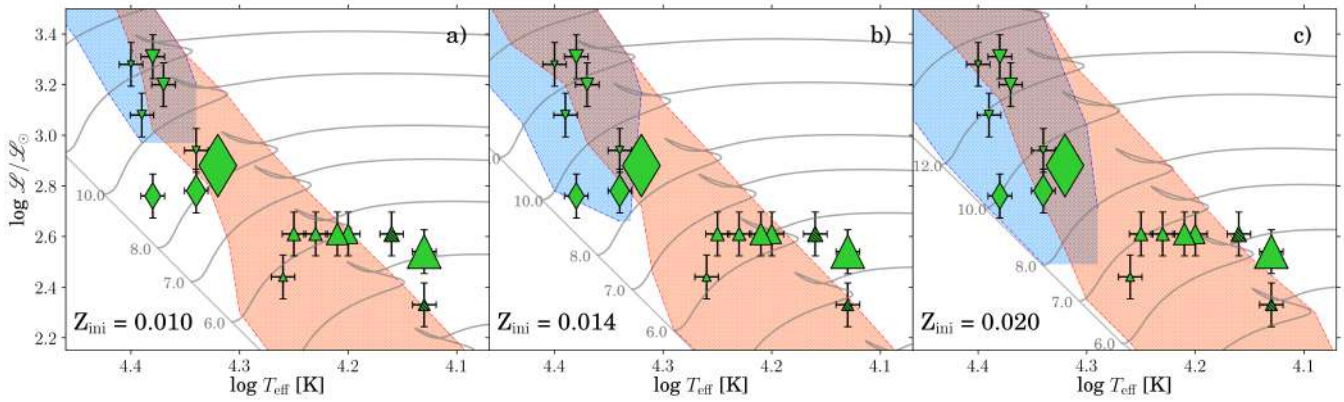

Fig. 13: Comparison of the pulsating B-type stars with the theoretical instability strips for $\ell = 0 - 2$ and three different metallicities $Z_{\rm ini} = 0.010, 0.014, 0.020$. β Cep stars are marked by downward triangles, SPB stars by upward triangles and hybrids pulsators by diamonds. The size of the symbol is proportional to the projected rotational velocity of the star which ranges between $v \sin i = 7 - 280$ km s^{-1}. Hatched symbols mark stars where the exact variability character of the star is uncertain.

The panels in Fig. 13 show the p mode instability domain ($n_{pg} > 0$) in blue for three different metallicities. The blue edge is confined to later evolutionary stages in the low metallicity regime (a), but extends (b) and finally meets the ZAMS for increasing metallicity (c), as expected (Pamyatnykh 1999). For the stars showing possible p mode pulsations (β Cep and hybrids) a metallicity of $Z_{\rm ini} = 0.014$ is sufficient to explain the occurrence of high frequency pulsation modes. The g mode instability domain ($n_{pg} < 0$) is shown in dark orange. The effect of increasing the metallicity is seen as the extension of the blue edge towards the ZAMS for increasing mass starting from the 5 $M_\odot$ model. The g modes in B2 IV hybrid HD 37209 cannot be explained by any increase in the metallicity. Rotation may be invoked to explain this. A similar case can be made for SPB star HD 57539

that appears to be post-MS in our evolutionary calculations. In a study by Szewczuk & Daszyńska-Daszkiewicz (2017) on the effect of rotation on the g mode instability region they found that the strip widens and moves to hotter and more massive stars. Moreover, they argue that rotation has a larger effect than the collective influence of initial hydrogen abundance, metallicity, overshooting and opacity.

We show the instability strips for different metallicities in the higher mass regime in the upper panels in Fig. 14. Again the extent of the strip is similar to what is found in previous work, i.e. Paxton et al. (2015) reaching 25 $M_\odot$ or Godart et al. (2017) for $Z_{\rm ini} = 0.015$. Compared to the latter we note the main difference is that the red edge of our p mode instability regime does not extend all the way to the red edge of the MS, even for high metallicity, because we only consider modes up to $\ell = 2$ while these authors computed high-degree modes as well. For visual clarity we only plot the O-type stars and BSGs that are identified as candidate pulsators in addition to stars with stochastic low frequency variability. The effect of increasing the metallicity is similar to what was seen in Fig. 13. However no high frequency modes were detected, except in the case of 15 Mon (HD 47839), where the high frequency mode more likely originates from the lower mass B-type companion (see Section 3.6).

The blue edge of the g mode instability strip (dark orange) is less sensitive to the metallicity value (a,b,c) but the blue edge still increases in temperature. Several of the stars that show stochastic low frequency variability, fall out of the instability region for coherent p and g modes in all metallicity regimes. Again rotation may be invoked to explain this, but we note that hydrodynamical simulations of massive stars suggest that pulsation frequencies can also be excited by core convection (Edelmann et al. (2019), Horst et al. submitted). In the cases of the more evolved stars, seen in the upper right of each panel in Fig. 14, the pulsations are predicted to be g modes, as the red edge of the p mode instability domain does not reach the TAMS. This conforms to the frequency ranges of variability observed in these stars.

For simplicity we only considered three discrete metallicities. This can only give a rough placement of the strips. For a more in-depth analysis a wider variety of input parameters need to be considered: i.e. rotation, interior mixing, opacity tables (as was already made clear in the seminal work by Pamyatnykh 1999 and later by Szewczuk & Daszyńska-Daszkiewicz 2017).

4.2. High mass (>25 $M_\odot$) evolutionary sequence

We selected several O and BSG stars in the high-mass regime to trace the variability for a hypothetical evolving high-mass star. We plot the stars in Fig. 15. On the top panel we show the sHRD with four stars following the same approximate evolutionary path between $40-60$ $M_\odot$, with different ages. The numbering corresponds to the rows of panels below, where we plot their LS-periodogram and two spectroscopic lines, HeI λ5875 and H_α. The light curve of each star is approximately 27 d. Star 3 and Star 4 show LPV and variable emission in H_α, indicative of the strong stellar wind. This is interesting with respect to the origin of the variability: clearly various physical mechanisms are responsible.

An immediate feature of the stars in Fig. 15 is the decrease in frequency (increase in period) of the dominant variability as one advances on the evolutionary tracks, as seen in the LS-periodogram and the inset light curve (right panels in Fig. 15). In Star 1 the stochastic low frequency variability only reaches the noise level around 10 d^{-1}, while in Star 4 the stochastic variability is constrained to lower frequencies. The increasing radius of an evolving star is responsible for the decreasing frequency. Another effect is the increase in the relative amplitude of the variability as the star ages, seen as the markers in the top panel of Fig. 15 that scale with the peak-to-peak variability in the light curve.

5. Summary

By combining TESS data and multi-epoch high-resolution spectroscopy gathered by the IACOB and OWN surveys, we provided a variability classification for a sample of OB-type stars in the southern hemisphere based on visual inspections followed by a frequency analysis. Each star is interesting in its own right, and we discussed several examples aided by the available spectroscopic parameters/variability. The low frequency resolution of only one or two TESS Sectors makes the identification of individual pulsation modes, combination frequencies and rotational multiplets/patterns difficult, especially in the low frequency regime (see Sections 3.2 and 3.3) and in stars with significant stochastic low frequency variability (see Sections 3.6 and Sections 3.7).

The fast rotating SPB star HD 57539 falls outside the theoretical non-rotating instability strips and modelling it is an interesting test for current theoretical understanding of pulsations in fast rotating stars. We find three new hybrid pulsators in our sample (HD 37481, HD 37303 and HD 37209), one of which (HD 37209) falls outside the g mode instability strip. Hybrid pulsators have much potential as they allow us to probe different regions in the star simultaneously. HD 37303 has significant modelling potential given that the large number of frequencies and potential multiplets provide possible means of mode identification.

The newly-discovered pulsating Be star HD 58978 has many modes, which would allow for a better understanding of this Be+sdO system. Additionally we find two Oe stars (HD 39680 and HD 45314) with g mode pulsations in distinct frequency groups indicative of non-linear pulsations in a rapidly-rotating star. Frequency groups have also been observed in Oe star ζ Oph and interpreted as a combination of radial and non-radial pulsations by Howarth et al. (2014). The occurrence of these frequency groups is interesting to compare to Be stars, that are known to exhibit similar frequency groups (see i.e. Neiner et al. 2009, 2012; Kurtz et al. 2015; Semaan et al. 2018, for later B-type stars). The presence of frequency groups in these two Oe stars observed with TESS supports the possible link between pulsations and the Oe/Be phenomenon. Although we could not clearly detect pulsations in the three new eclipsing binaries (HD 159176, HD 46485 and HD 23466), HD 23466 is a promising candidate for in-depth analysis to determine the origin of the complex variability.

Several blue supergiants (i.e. HD 51309 and HD 27563) show frequencies that are unrelated to the wind variability, and which are likely pulsation modes, similar to those observed photometrically in e.g. B2Ib/II star HD 163899 (Saio et al. 2006), and O9.5Iab star HD 188209 (Aerts et al. 2017a). Additionally, two O supergiants (HD 151805 and HD 303492) show a dense frequency group in the low frequency regime. HD 303492 shows a potential triplet, making it a good candidate for further investigation. For detailed asteroseismic studies of these evolved stars additional long term spectroscopy and photometry is needed to properly identify the pulsation modes observed in the TESS photometry.

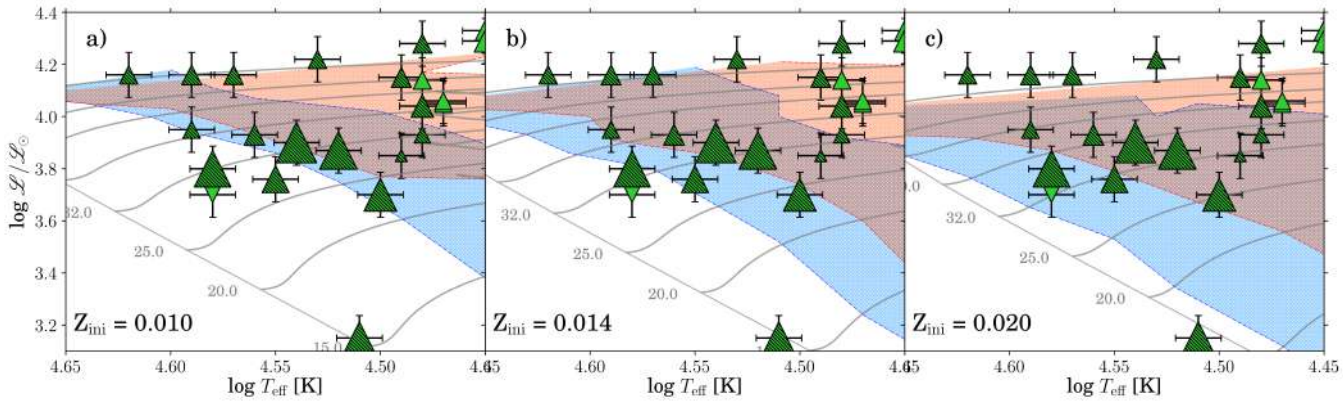

Fig. 14: Comparison of the candidate pulsating O-type stars with the theoretical instability strips for $\ell = 0 - 2$ and three different metallicities $Z_{ini} = 0.010, 0.014, 0.020$. Same figure style as Fig. 13. The size of the symbol is proportional to the projected rotational velocity of the star which ranges between $v \sin i = 26-291$ km s^{-1}. Hatched symbols mark stars where the exact variability character of the star is uncertain.

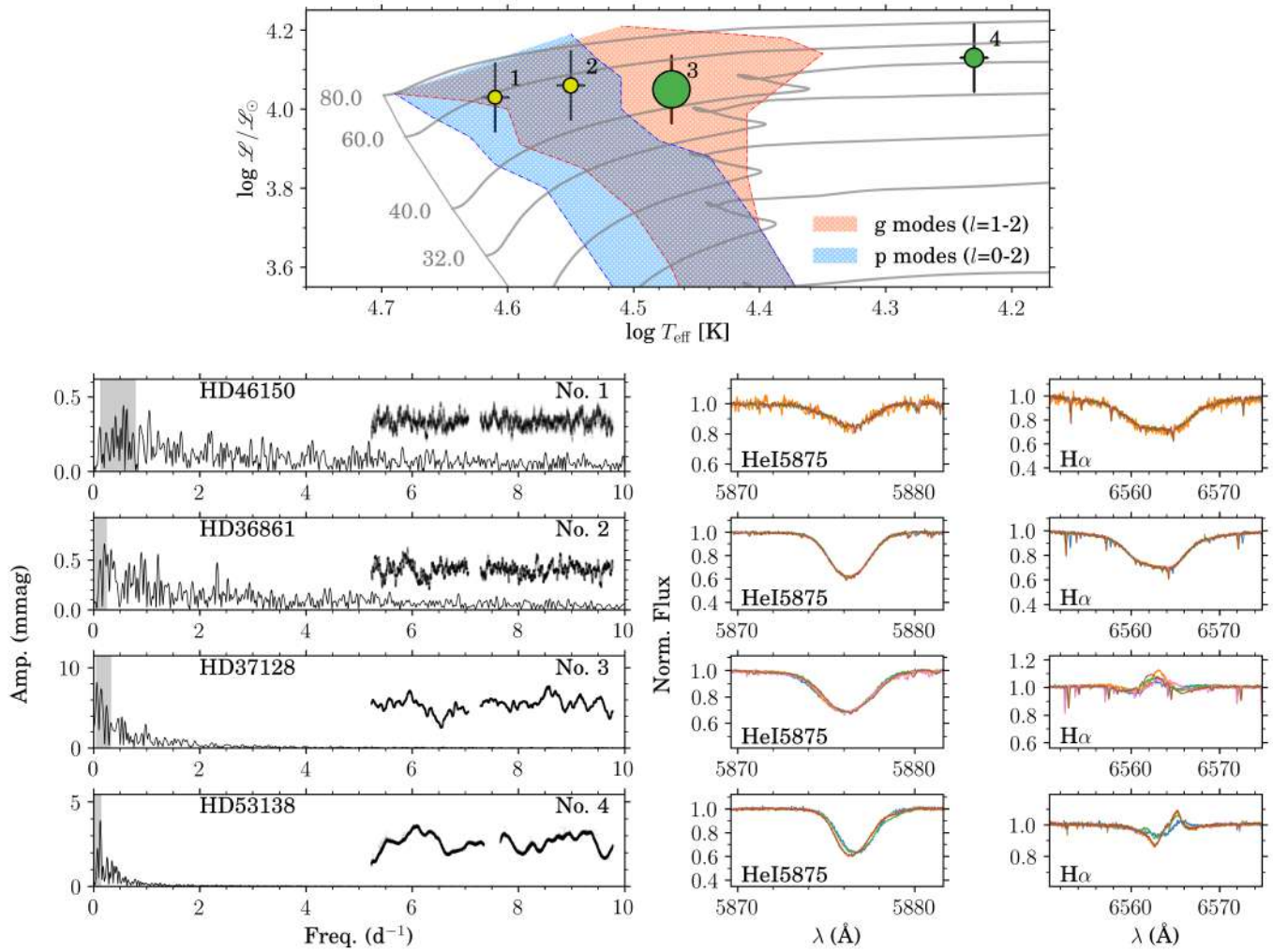

Fig. 15: High mass evolutionary sequence. *Top:* spectroscopic Hertzsprung-Russell diagram with size of the symbols the peak-to-peak value of the light curve (between 7.7 and 63.8 mmag). We include the evolutionary tracks in gray and the instability strips for $Z_{in} = 0.014$. *Bottom:* For each star marked with a number in the top panel, the LS-periodogram (*left*), and two spectroscopic lines (HeI λ5875 and H_α, *right*) over multiple epochs are given. The grey region in the LS-periodogram marks the approximate range where rotation related frequencies are expected (see Section 2.3). On the inset of the LS-periodogram we show the TESS light curve (not to scale).

The one sector TESS light curves are generally sufficient to put some constraints on the type of variability. However, the computed instability strips were not able to fully explain the range of observed variability in OB type stars. The stars falling outside the instability strips are mostly fast-rotating, indicating that instability strips with rotation are needed to make detailed comparisons between such strips and large samples (see also Szewczuk & Daszyńska-Daszkiewicz (2017)). This illustrates that variability classification of OB-type stars in large numbers is necessary to accurately constrain the observational instability boundaries. The current ongoing TESS observations in the northern sky will surely further aid in this venture. To cover wider ranges in the upper part of the HRD, there is also large potential in extracting OB-type star light curves from the TESS Full Frame Images, and combining this with complementary spectroscopy from upcoming all-sky spectroscopic surveys such as SDSS-V (Kollmeier et al. 2017).

By tracing the variability for a hypothetical massive star we saw observational confirmation of stellar evolution: the dominant variability decreases in frequency (increases in period), and increases in amplitude, as the star ages. This is a starting point to understand the structure and evolution of massive stars through their photometric variability and pulsations. In all the newly-found potential pulsating stars additional continuous space photometry, multi-colour photometry or high-resolution multi-epoch spectroscopy is advised to achieve mode identification. To constrain the physics of the interiors of massive stars multidimensional theoretical instability strips (i.e. in rotation, metallicity, overshooting, and envelope mixing) should be considered. However, to achieve this efficiently, the top-down method in this work should be reversed. First, the selection of optimal candidates from long-term continuous photometry (i.e. the TESS Continuous Viewing Zone and Kepler/K2) that allow for mode identification through period/frequency patterns is needed. Only then these are to be followed-up with spectroscopy, and asteroseismic modelling. See for example the ensemble modelling approaches taken for low-mass stars (i.e. Chaplin et al. 2014; Yu et al. 2018), and intermediate-mass stars (i.e. Mombarg et al. 2019; Ouazzani et al. 2019), that have allowed to put constraints on interior physics such as overshooting, angular momentum transport, and chemical mixing.

Acknowledgements. SB is thankful to the staff of the IAC for the possibility of and kind hospitality during his research visit there, which made this joint project possible. SB and MM are grateful to Rich Townsend for his inspiring and highly didactical tutorial on mode excitation during the 2019 MESA summer school and for his continuous efforts to upgrade the GYRE pulsation code for the benefit of the asteroseismology community. The MESA developers are also thanked for their efforts. The research leading to these results has received funding from the European Research Council (ERC) under the European Union's Horizon 2020 research and innovation program (grant agreement No. 670519: MAMSIE). S-SD acknowledges support from the Spanish Government Ministerio de Ciencia, Innovación y Universidades through grants PGC-2018-091 3741-B-C22. This research has made use of the SIMBAD database, operated at CDS, Strasbourg, France. Some/all of the data presented in this paper were obtained from the Mikulski Archive for Space Telescopes (MAST). STScI is operated by the Association of Universities for Research in Astronomy, Inc., under NASA contract NAS5-26555. The computational resources and services used in this work were provided by the VSC (Flemish Supercomputer Center), funded by the Research Foundation - Flanders (FWO) and the Flemish Government – department EWI.

References

Abt, H. A., Wang, R., & Cardona, O. 1991, ApJ, 367, 155
Aerts, C. 2019, arXiv e-prints, In press, arXiv:1912.12300
Aerts, C., Christensen-Dalsgaard, J., & Kurtz, D. W. 2010, Asteroseismology (Springer)
Aerts, C., de Pauw, M., & Waelkens, C. 1992, A&A, 266, 294
Aerts, C., Marchenko, S. V., Matthews, J. M., et al. 2006, ApJ, 642, 470
Aerts, C., Mathis, S., & Rogers, T. 2019, ARA&A, in press, arXiv:1809.07779
Aerts, C., Puls, J., Godart, M., & Dupret, M.-A. 2009, A&A, 508, 409
Aerts, C. & Rogers, T. M. 2015, ApJ, 806, L33
Aerts, C., Símon-Díaz, S., Bloemen, S., et al. 2017a, A&A, 602, A32
Aerts, C., Simón-Díaz, S., Catala, C., et al. 2013, A&A, 557, A114
Aerts, C., Van Reeth, T., & Tkachenko, A. 2017b, ApJ, 847, L7
Aerts, C., Waelkens, C., & de Pauw, M. 1994, A&A, 286, 136
Augustson, K. C. & Mathis, S. 2019, ApJ, 874, 83
Auvergne, M., Bodin, P., Boisnard, L., et al. 2009, A&A, 506, 411
Baade, D., Pigulski, A., Rivinius, T., et al. 2018, A&A, 610, A70
Baade, D., Rivinius, T., Pigulski, A., et al. 2016, A&A, 588, A56
Balona, L. A. & Engelbrecht, C. A. 1985, MNRAS, 214, 559
Barbá, R., Gamen, R., Arias, J. I., et al. 2014, in Revista Mexicana de Astronomia y Astrofisica Conference Series, Vol. 44, Revista Mexicana de Astronomia y Astrofisica Conference Series, 148–148
Barbá, R. H., Gamen, R., Arias, J. I., et al. 2010, in Revista Mexicana de Astronomia y Astrofisica Conference Series, Vol. 38, Revista Mexicana de Astronomia y Astrofisica Conference Series, 30–32
Barron, J., Wade, G. A., Bowman, D. M., et al. 2020, arXiv e-prints, arXiv:2001.04534
Bestenlehner, J. M., Gräfener, G., Vink, J. S., et al. 2014, A&A, 570, A38
Blazère, A., Neiner, C., Tkachenko, A., Bouret, J. C., & Rivinius, T. 2015, A&A, 582, A110
Blomme, R., Mahy, L., Catala, C., et al. 2011, A&A, 533, A4
Blomme, R., Prinja, R. K., Runacres, M. C., & Colley, S. 2002, A&A, 382, 921
Borucki, W. J., Koch, D., Basri, G., et al. 2010, Science, 327, 977
Bouret, J. C., Donati, J. F., Martins, F., et al. 2008, MNRAS, 389, 75
Bowman, D. M., Aerts, C., Johnston, C., et al. 2019a, A&A, 621, A135
Bowman, D. M., Burssens, S., Pedersen, M. G., et al. 2019b, Nature Astronomy, 3, 760
Bowman, D. M., Kurtz, D. W., Breger, M., Murphy, S. J., & Holdsworth, D. L. 2016, MNRAS, 460, 1970
Breger, M., Stich, J., Garrido, R., et al. 1993, A&A, 271, 482
Briquet, M., Aerts, C., Baglin, A., et al. 2011, A&A, 527, A112
Brott, I., de Mink, S. E., Cantiello, M., et al. 2011, A&A, 530, A115
Buchler, J. R., Goupil, M. J., & Hansen, C. J. 1997, A&A, 321, 159
Buchler, J. R., Goupil, M. J., & Serre, T. 1995, A&A, 296, 405
Burssens, S., Bowman, D. M., Aerts, C., et al. 2019, MNRAS, 489, 1304
Buysschaert, B., Aerts, C., Bloemen, S., et al. 2015, MNRAS, 453, 89
Buysschaert, B., Aerts, C., Bowman, D. M., et al. 2018a, A&A, 616, A148
Buysschaert, B., Neiner, C., Martin, A. J., et al. 2018b, MNRAS, 478, 2777
Bychkov, V. D., Bychkova, L. V., & Madej, J. 2003, A&A, 407, 631
Bychkov, V. D., Bychkova, L. V., & Madej, J. 2005, A&A, 430, 1143
Cantiello, M. & Braithwaite, J. 2019, ApJ, 883, 106
Cantiello, M., Langer, N., Brott, I., et al. 2009, A&A, 499, 279
Castro, N., Fossati, L., Hubrig, S., et al. 2015, A&A, 581, A81
Castro, N., Fossati, L., Langer, N., et al. 2014, A&A, 570, L13
Castro, N., Oey, M. S., Fossati, L., & Langer, N. 2018, ApJ, 868, 57
Cazorla, C., Morel, T., Nazé, Y., et al. 2017, A&A, 603, A56
Chaplin, W. J., Basu, S., Huber, D., et al. 2014, ApJS, 210, 1
Charpinet, S., Fontaine, G., Brassard, P., et al. 1997, ApJ, 483, L123
Chieffi, A. & Limongi, M. 2013, ApJ, 764, 21
Chini, R., Hoffmeister, V. H., Nasseri, A., Stahl, O., & Zinnecker, H. 2012, MNRAS, 424, 1925
Conti, P. S. & Leep, E. M. 1974, ApJ, 193, 113
Crowther, P. A. & Bohannan, B. 1997, A&A, 317, 532
Crowther, P. A., Lennon, D. J., & Walborn, N. R. 2006, A&A, 446, 279
David-Uraz, A., Neiner, C., Sikora, J., et al. 2019, MNRAS, 487, 304
David-Uraz, A., Wade, G. A., Petit, V., et al. 2014, MNRAS, 444, 429
De Becker, M., Rauw, G., Pittard, J. M., et al. 2004, A&A, 416, 221
De Cat, P. & Aerts, C. 2002, A&A, 393, 965
de Mink, S. E. & Belczynski, K. 2015, ApJ, 814, 58
Degroote, P., Briquet, M., Catala, C., et al. 2009, A&A, 506, 111
Donati, J. F., Babel, J., Harries, T. J., et al. 2002, MNRAS, 333, 55
Dufton, P. L., Langer, N., Dunstall, P. R., et al. 2013, A&A, 550, A109
Dufton, P. L., Thompson, A., Crowther, P. A., et al. 2018, A&A, 615, A101
Dziembowski, W. 1982, Acta Astron., 32, 147
Dziembowski, W. A., Moskalik, P., & Pamyatnykh, A. A. 1993, MNRAS, 265, 588
Dziembowski, W. A. & Pamiatnykh, A. A. 1993, MNRAS, 262, 204
Edelmann, P. V. F., Ratnasingam, R. P., Pedersen, M. G., et al. 2019, ApJ, 876, 4
Eggleton, P. P. & Percy, J. R. 1973, MNRAS, 161, 421
Eggleton, P. P. & Tokovinin, A. A. 2008, MNRAS, 389, 869
Ekström, S., Georgy, C., Eggenberger, P., et al. 2012, A&A, 537, A146
Evans, C. J., Smartt, S. J., Lee, J.-K., et al. 2005, A&A, 437, 467
Evans, C. J., Taylor, W. D., Hénault-Brunet, V., et al. 2011, A&A, 530, A108
Frémat, Y., Neiner, C., Hubert, A. M., et al. 2006, A&A, 451, 1053
Frost, E. B. 1902, ApJ, 15

Frost, S. A. & Conti, P. S. 1976, in IAU Symposium, Vol. 70, Be and Shell Stars, ed. A. Slettebak, 139
Fullerton, A. W., Gies, D. R., & Bolton, C. T. 1992, ApJ, 390, 650
Gaia Collaboration, Brown, A. G. A., Vallenari, A., et al. 2018, A&A, 616, A1
Gaia Collaboration, Prusti, T., de Bruijne, J. H. J., et al. 2016, A&A, 595, A1
Gautschy, A. & Saio, H. 1993, MNRAS, 262, 213
Georgy, C., Ekström, S., Meynet, G., et al. 2012, A&A, 542, A29
Gies, D. R. 1987, ApJS, 64, 545
Gies, D. R., Fullerton, A. W., Bolton, C. T., et al. 1994, ApJ, 422, 823
Godart, M., Simón-Díaz, S., Herrero, A., et al. 2017, A&A, 597, A23
Gray, D. F. 2005, The Observation and Analysis of Stellar Photospheres
Grellmann, R., Preibisch, T., Ratzka, T., et al. 2013, A&A, 550, A82
Grunhut, J. H., Wade, G. A., Marcolino, W. L. F., et al. 2009, MNRAS, 400, L94
Grunhut, J. H., Wade, G. A., Neiner, C., et al. 2017, MNRAS, 465, 2432
Grunhut, J. H., Wade, G. A., Sundqvist, J. O., et al. 2012, MNRAS, 426, 2208
Gutiérrez-Soto, J., Fabregat, J., Suso, J., et al. 2007, A&A, 476, 927
Handler, G., Jerzykiewicz, M., Rodríguez, E., et al. 2006, MNRAS, 365, 327
Handler, G., Pigulski, A., Daszyńska-Daszkiewicz, J., et al. 2019, ApJ, 873, L4
Haucke, M., Cidale, L. S., Venero, R. O. J., et al. 2018, A&A, 614, A91
Heynderickx, D. 1992, A&AS, 96, 207
Heynderickx, D., Waelkens, C., & Smeyers, P. 1994, A&AS, 105, 447
Hillier, D. J. & Miller, D. L. 1998, ApJ, 496, 407
Holgado, G., Simón-Díaz, S., & Barbá, R. 2017, in IAU Symposium, Vol. 329, The Lives and Death-Throes of Massive Stars, ed. J. J. Eldridge, J. C. Bray, L. A. S. McClelland, & L. Xiao, 407–407
Holgado, G., Simón-Díaz, S., Barbá, R. H., et al. 2018, A&A, 613, A65
Howarth, I. D., Goss, K. J. F., Stevens, I. R., Chaplin, W. J., & Elsworth, Y. 2014, MNRAS, 440, 1674
Howell, S. B., Sobeck, C., Haas, M., et al. 2014, PASP, 126, 398
Huat, A.-L., Hubert, A.-M., Baudin, F., et al. 2009, A&A, 506, 95
Hubrig, S., Küker, M., Järvinen, S. P., et al. 2019, MNRAS, 484, 4495
Jenkins, J. M., Twicken, J. D., McCauliff, S., et al. 2016, in Proc. SPIE, Vol. 9913, Software and Cyberinfrastructure for Astronomy IV, 99133E
Jerzykiewicz, M. 1999, New A Rev., 43, 455
Jerzykiewicz, M., Sterken, C., & Kubiak, M. 1988, A&AS, 72, 449
Karlsson, B. 1969, Arkiv for Astronomi, 5, 241
Kaufer, A., Wolf, B., Andersen, J., & Pasquini, L. 1997, The Messenger, 89, 1
Kilkenny, D. 2007, Communications in Asteroseismology, 150, 234
Koen, C. & Eyer, L. 2002, MNRAS, 331, 45
Köhler, R., Petr-Gotzens, M. G., McCaughrean, M. J., et al. 2006, A&A, 458, 461
Kollmeier, J. A., Zasowski, G., Rix, H.-W., et al. 2017, arXiv e-prints, arXiv:1711.03234
Krtička, J. & Feldmeier, A. 2018, A&A, 617, A121
Kurtz, D. W., Saio, H., Takata, M., et al. 2014, MNRAS, 444, 102
Kurtz, D. W., Shibahashi, H., Murphy, S. J., Bedding, T. R., & Bowman, D. M. 2015, MNRAS, 450, 3015
Landstreet, J. D. & Borra, E. F. 1978, ApJ, 224, L5
Langer, N. 2012, ARA&A, 50, 107
Langer, N. & Kudritzki, R. P. 2014, A&A, 564, A52
Lecoanet, D., Cantiello, M., Quataert, E., et al. 2019, ApJ, 886, L15
Lefever, K., Puls, J., & Aerts, C. 2007, A&A, 463, 1093
Lefèvre, L., Marchenko, S. V., Moffat, A. F. J., & Acker, A. 2009, A&A, 507, 1141
Lesh, J. R. & Wesselius, P. R. 1979, A&A, 79, 115
Li, G., Bedding, T. R., Murphy, S. J., et al. 2019, MNRAS, 482, 1757
Linder, N., Rauw, G., Sana, H., De Becker, M., & Gosset, E. 2007, A&A, 474, 193
Lomb, N. R. 1976, Ap&SS, 39, 447
Maisonneuve, F. 2011, PhD thesis, -
Manfroid, J. 1989, Information Bulletin on Variable Stars, 3297, 1
Markova, N., Puls, J., & Langer, N. 2018, A&A, 613, A12
Martins, F. & Palacios, A. 2013, A&A, 560, A16
Martins, F., Schaerer, D., & Hillier, D. J. 2005, A&A, 436, 1049
Mason, B. D., Hartkopf, W. I., Gies, D. R., Henry, T. J., & Helsel, J. W. 2009, AJ, 137, 3358
Mathys, G., Manfroid, J., & Renson, P. 1986, A&AS, 63, 403
Mazumdar, A., Briquet, M., Desmet, M., & Aerts, C. 2006, A&A, 459, 589
McNamara, D. H. 1953, PASP, 65, 286
McNamara, D. H. 1955, ApJ, 122, 95
Miglio, A., Montalbán, J., & Dupret, M.-A. 2007, Communications in Asteroseismology, 151, 48
Mohan, V. 1981, Ap&SS, 76, 83
Mombarg, J. S. G., Van Reeth, T., Pedersen, M. G., et al. 2019, MNRAS, 485, 3248
Moravveji, E. 2016, MNRAS, 455, L67
Moravveji, E., Aerts, C., Pápics, P. I., Triana, S. A., & Vandoren, B. 2015, A&A, 580, A27
Moravveji, E., Townsend, R. H. D., Aerts, C., & Mathis, S. 2016, ApJ, 823, 130
Morel, T., Marchenko, S. V., Pati, A. K., et al. 2004, MNRAS, 351, 552
Morrell, N. & Levato, H. 1991a, ApJS, 75, 965
Morrell, N. & Levato, H. 1991b, ApJS, 75, 965
Moskalik, P. & Dziembowski, W. A. 1992, A&A, 256, L5
Negueruela, I., Steele, I. A., & Bernabeu, G. 2004, Astronomische Nachrichten, 325, 749
Neilson, H. R. & Ignace, R. 2015, A&A, 584, A58
Neiner, C., Gutiérrez-Soto, J., Baudin, F., et al. 2009, A&A, 506, 143
Neiner, C., Mathis, S., Saio, H., & Lee, U. 2013, in Astronomical Society of the Pacific Conference Series, Vol. 479, Progress in Physics of the Sun and Stars: A New Era in Helio- and Asteroseismology, ed. H. Shibahashi & A. E. Lynas-Gray, 319
Neiner, C., Mathis, S., Saio, H., et al. 2012, A&A, 539, A90
Nieva, M. F. & Przybilla, N. 2012, A&A, 539, A143
Oksala, M. E., Wade, G. A., Townsend, R. H. D., et al. 2012, MNRAS, 419, 959
Ouazzani, R. M., Marques, J. P., Goupil, M. J., et al. 2019, A&A, 626, A121
Pamyatnykh, A. A. 1999, Acta Astron., 49, 119
Pápics, P. I. 2012, Astronomische Nachrichten, 333, 1053
Pápics, P. I., Briquet, M., Baglin, A., et al. 2012, A&A, 542, A55
Pápics, P. I., Tkachenko, A., Van Reeth, T., et al. 2017, A&A, 598, A74
Paxton, B., Bildsten, L., Dotter, A., et al. 2011, ApJS, 192, 3
Paxton, B., Cantiello, M., Arras, P., et al. 2013, ApJS, 208, 4
Paxton, B., Marchant, P., Schwab, J., et al. 2015, ApJS, 220, 15
Paxton, B., Schwab, J., Bauer, E. B., et al. 2018, ApJS, 234, 34
Pedersen, M. G. 2020, PhD thesis, KU Leuven, In Press
Pedersen, M. G., Chowdhury, S., Johnston, C., et al. 2019, ApJ, 872, L9
Percy, J. R. & Lane, M. C. 1977, AJ, 82, 353
Peters, G. J., Gies, D. R., Grundstrom, E. D., & McSwain, M. V. 2008, ApJ, 686, 1280
Peters, G. J., Ogawa, H. S., Judge, K. S., & Judge, D. L. 1987, ApJ, 314, 261
Petit, V., Wade, G. A., Drissen, L., Montmerle, T., & Alecian, E. 2008, MNRAS, 387, L23
Petit, V., Wade, G. A., Schneider, F. R. N., et al. 2019, MNRAS, 489, 5669
Porter, J. M. & Rivinius, T. 2003, PASP, 115, 1153
Pourbaix, D., Tokovinin, A. A., Batten, A. H., et al. 2004, A&A, 424, 727
Prinja, R. K., Fullerton, A. W., & Crowther, P. A. 1996, A&A, 311, 264
Prinja, R. K., Rivinius, T., Stahl, O., et al. 2004, A&A, 418, 727
Puebla, R. E., Hillier, D. J., Zsargó, J., Cohen, D. H., & Leutenegger, M. A. 2016, MNRAS, 456, 2907
Ramiaramanantsoa, T., Ratnasingam, R., Shenar, T., et al. 2018, MNRAS, 480, 972
Ramírez-Agudelo, O. H., Sana, H., de Mink, S. E., et al. 2015, A&A, 580, A92
Ramírez-Agudelo, O. H., Simón-Díaz, S., Sana, H., et al. 2013, A&A, 560, A29
Randall, S. K., Calamida, A., Fontaine, G., et al. 2016, A&A, 589, A1
Raskin, G., van Winckel, H., Hensberge, H., et al. 2011, A&A, 526, A69
Rauw, G., Nazé, Y., Smith, M. A., et al. 2018, A&A, 615, A44
Rauw, G., Nazé, Y., Spano, M., Morel, T., & ud-Doula, A. 2013, A&A, 555, L9
Ricker, G. R., Winn, J. N., Vanderspek, R., et al. 2014, in Proc. SPIE, Vol. 9143, Space Telescopes and Instrumentation 2014: Optical, Infrared, and Millimeter Wave, 914320
Rivinius, T., Baade, D., & Carciofi, A. C. 2016, A&A, 593, A106
Rivinius, T., Štefl, S., Maintz, M., Stahl, O., & Baade, D. 2004, A&A, 427, 307
Rogers, T. M. 2015, ApJ, 815, L30
Rogers, T. M., Lin, D. N. C., McElwaine, J. N., & Lau, H. H. B. 2013, ApJ, 772, 21
Rogers, T. M. & McElwaine, J. N. 2017, ApJ, 848, L1
Saesen, S., Briquet, M., & Aerts, C. 2006, Communications in Asteroseismology, 147, 109
Saio, H., Kuschnig, R., Gautschy, A., et al. 2006, ApJ, 650, 1111
Salmon, S., Montalbán, J., Morel, T., et al. 2012, MNRAS, 422, 3460
Sana, H., de Mink, S. E., de Koter, A., et al. 2012, Science, 337, 444
Sana, H., Le Bouquin, J.-B., Lacour, S., et al. 2014, ApJS, 215, 15
Scargle, J. D. 1982, ApJ, 263, 835
Schmid, V. S. & Aerts, C. 2016, A&A, 592, A116
Schwarzenberg-Czerny, A. 2003, in Astronomical Society of the Pacific Conference Series, Vol. 292, Interplay of Periodic, Cyclic and Stochastic Variability in Selected Areas of the H-R Diagram, ed. C. Sterken, 383
Searle, S. C., Prinja, R. K., Massa, D., & Ryans, R. 2008, A&A, 481, 777
Semaan, T., Hubert, A. M., Zorec, J., et al. 2018, A&A, 613, A70
Shenar, T., Oskinova, L. M., Järvinen, S. P., et al. 2017, A&A, 606, A91
Shobbrook, R. R. 1973a, MNRAS, 161, 257
Shobbrook, R. R. 1973b, MNRAS, 162, 25
Shobbrook, R. R. 1981, MNRAS, 196, 129
Shobbrook, R. R., Handler, G., Lorenz, D., & Mogorosi, D. 2006, MNRAS, 369, 171
Shultz, M., Kochukhov, O., Wade, G. A., & Rivinius, T. 2018, MNRAS, 478, L39
Shultz, M., Le Bouquin, J. B., Rivinius, T., et al. 2019, MNRAS, 482, 3950
Shultz, M., Wade, G. A., Rivinius, T., et al. 2017, MNRAS, 471, 2286
Sikora, J., David-Uraz, A., Chowdhury, S., et al. 2019, MNRAS, 487, 4695
Simón-Díaz, S., Aerts, C., Urbaneja, M. A., et al. 2018, A&A, 612, A40

Simón-Díaz, S., Castro, N., Garcia, M., Herrero, A., & Markova, N. 2011a, Bulletin de la Societe Royale des Sciences de Liege, 80, 514
Simón-Díaz, S., Castro, N., Herrero, A., et al. 2011b, in Journal of Physics Conference Series, Vol. 328, Journal of Physics Conference Series, 012021
Simón-Díaz, S., Godart, M., Castro, N., et al. 2017, A&A, 597, A22
Simón-Díaz, S. & Herrero, A. 2014, A&A, 562, A135
Simón-Díaz, S., Herrero, A., Uytterhoeven, K., et al. 2010, ApJ, 720, L174
Simón-Díaz, S., Negueruela, I., Maíz Apellániz, J., et al. 2015, in Highlights of Spanish Astrophysics VIII, ed. A. J. Cenarro, F. Figueras, C. Hernández-Monteagudo, J. Trujillo Bueno, & L. Valdivielso, 576–581
Sota, A., Apellániz, J. M., Morrell, N. I., et al. 2014, The Astrophysical Journal Supplement Series, 211, 10
Sota, A., Maíz Apellániz, J., Walborn, N. R., et al. 2011, ApJS, 193, 24
Stankov, A. & Handler, G. 2005, ApJS, 158, 193
Stassun, K. G., Oelkers, R. J., Pepper, J., et al. 2018, AJ, 156, 102
Szewczuk, W. & Daszyńska-Daszkiewicz, J. 2017, MNRAS, 469, 13
Szewczuk, W. & Daszyńska-Daszkiewicz, J. 2018, MNRAS, 478, 2243
Telting, J. H., Avila, G., Buchhave, L., et al. 2014, Astronomische Nachrichten, 335, 41
Telting, J. H., Schrijvers, C., Ilyin, I. V., et al. 2006, A&A, 452, 945
Thomas, J. C. 1975, in BAAS, Vol. 7, 533
Thoul, A., Degroote, P., Catala, C., et al. 2013, A&A, 551, A12
Tkachenko, A., Degroote, P., Aerts, C., et al. 2014, MNRAS, 438, 3093
Townsend, R. H. D., Goldstein, J., & Zweibel, E. G. 2018, MNRAS, 475, 879
Townsend, R. H. D., Owocki, S. P., & Howarth, I. D. 2004, MNRAS, 350, 189
Townsend, R. H. D. & Teitler, S. A. 2013, MNRAS, 435, 3406
Van Reeth, T., Tkachenko, A., Aerts, C., et al. 2015, ApJS, 218, 27
Vink, J. S. 2018, A&A, 619, A54
Vink, J. S., Muijres, L. E., Anthonisse, B., et al. 2011, A&A, 531, A132
Wade, G. A., Fullerton, A. W., Donati, J. F., et al. 2006, A&A, 451, 195
Wade, G. A., Neiner, C., Alecian, E., et al. 2016, MNRAS, 456, 2
Waelkens, C. 1991, A&A, 246, 453
Walczak, P., Fontes, C. J., Colgan, J., Kilcrease, D. P., & Guzik, J. A. 2015, A&A, 580, L9
Walker, G., Matthews, J., Kuschnig, R., et al. 2003, PASP, 115, 1023
Yu, J., Huber, D., Bedding, T. R., et al. 2018, ApJS, 236, 42

Appendix A: Frequency analysis

For the frequency analysis we perform *iterative pre-whitening* following the method described in Degroote et al. (2009) and improved by Pápics et al. (2012). At each step in this iterative process the LS-periodogram is calculated followed by a search for the frequency with the highest amplitude. This frequency, together with previous frequencies, is then used to preform a non-linear squares fit on the light curve using a sinusoidal model. Each iteration this model is subtracted from the light curve and the next frequency is searched for. The algorithm is repeated until the signal to noise ratio (S/N) centred around the newly found peak falls below 4 in a 5 d^{-1} window, following Breger et al. (1993).

When the significance criterion is reached the frequency list is processed further. This includes removing frequencies that are unresolved to one another, using the Loumos & Deeming criterion, $1.5/\Delta T$ for a light curve of length ΔT. The time span ΔT (d) is calculated using the first and last day of observation, not accounting for the intermittent gap that is present in the middle of every light curve. This due to a pause of 1.09 d in data collection during perigree passage while downloading data. We note that Sector 6 provides the shortest light curves in the whole sample, just 21.77 d of data were collected ($1/\Delta T = 0.046$ d^{-1}). This is due to the first ≈ 3 d being used to collect calibration data[9].

We further search for potential combination frequencies and harmonics. This involves selecting the two highest amplitude frequencies and looking for other frequencies of the form $nv_i + mv_j$ with orders $n, m \in [-3, 3]$ in an automatic way. We use the frequency resolution ($1/\Delta T$) as the matching criterion. We process these matches further by evaluating the likehood that higher order combinations are real based on the presence of lower order combinations, given that the chance occurrence of a match increases with the order (Pápics 2012).

We summarise the global results of the frequency analysis in Table A.1. In Column 3 we give the frequency resolution in d^{-1} of that particular light curve. Column 4 and 5 give the dominant frequency and its associated amplitude. The number in brackets in the frequency and amplitude columns gives the error on the last digit. This error is calculated based on the non-linear squares fit, and we further employ a correction factor to compensate for the correlated nature of the data. We use the correction factor by Schwarzenberg-Czerny (2003), calculated following Degroote et al. (2009). The signal to noise of that particular frequency is given in Column 6. In Column 7 we provide notes for that particular star: *ND* (non-detection) if the dominant frequency is below a S/N of 4, *IV* (invalid) if the light curve is of poor quality or contaminated, an asterisk (*) if the frequency analysis is discussed in more detail in the main text.

The full frequency lists of the intrinsic variable stars discussed in Section 3 are given in Table A.2. The number in brackets in the frequency, amplitude and phase columns gives the error on the last digit. In the last column we add notes to highlight potential combinations/harmonics or multiplet membership. The latter are indicated as follows: tp/tp? (triplet) or mp/mp? (multiplet) followed by a number if more than one was detected.

[9] see the TESS-DR8 release notes for more information, https://archive.stsci.edu/missions/tess/doc/tess_drn/tess_sector_06_drn08_v02.pdf

Table A.1: Summary of the frequency analysis of the stars considered in this work.

HD	TIC	$1/\Delta T$ (d^{-1})	ν_{dom} (d^{-1})	A_{dom} (mmag)	S/N	Var. Type	Notes
			O-type dwarfs and subgiants (V and IV)				
HD 96715	306491594	0.018	0.4780(7)	0.33(2)	4.18	SLF	
HD 46223	234881667	0.046	0.181(2)	0.81(5)	4.45	SLF+SPB?	
HD 155913	216662610	0.040	1.637(1)	1.55(7)	6.4	rot	
HD 46150	234840662	0.046	0.563(2)	0.44(3)	3.63	SLF	ND
HD 90273	464295672	0.041	0.582(1)	0.65(4)	4.17	SLF+SPB?	
HD 110360	433738620	0.039	1.2370(5)	0.80(2)	8.66	PQD	IV
HD 47839	220322383	0.046	12.5436(7)	0.39(1)	19.12	SLF+β Cep	
HD 46485	234933888	0.046	0.1453(4)	8.9(1)	15.43	EB	*
HD 53975	148506724	0.041	0.1698(5)	1.11(3)	11.58	SLF+rot	
HD 41997	294114621	0.046	1.220(2)	2.5(2)	5.53	SLF+rot?	
HD 152590	341258182	0.040	0.444(3)	25(3)	5.95	EB	
HD 46573	234947719	0.046	0.349(2)	0.99(6)	4.07	SLF+rot?	
HD 48279	234009943	0.046	1.213(2)	0.69(4)	4.1	SLF+SPB?	
HD 101191	319936861	0.018	0.9551(2)	1.89(4)	13.25	cont.	
HD 46056	234834992	0.046	6.040(2)	0.29(2)	4.55	sys	IV
HD 38666	100589904	0.019	0.8350(3)	0.168(4)	8.74	PQD	IV
HD 36512	34512896	0.046	0.3066(7)	0.193(5)	10.38	SLF+rot	
HD 123056	330281456	0.039	0.4756(7)	2.23(7)	9.3	SLF+SPB?	
HD 76556	30135331	0.041	0.235(2)	3.0(2)	6.19	SLF+SPB?	
HD 74920	430625455	0.020	1.568(1)	1.0(1)	3.93	SLF+SPB?	ND
HD 135591	455675248	0.036	0.625(2)	0.89(8)	5.68	SLF	
HD 326331	339568114	0.040	0.188(2)	2.5(3)	4.27	SLF	
HD 37041	427395049	0.046	0.376(1)	0.106(5)	5.19	SLF+SPB?	
HD 48099	231154751	0.046	0.6559(10)	1.00(4)	7.44	SLF+rot	
HD 159176	102643159	0.040	0.5929(5)	7.0(2)	15.35	EB	*
HD 54662	177717406	0.041	0.710(1)	0.19(1)	3.58	SLF+SPB?	ND
HD 57236	5051420	0.041	0.2547(4)	0.57(1)	14.2	SLF+rot	
HD 75759	29207816	0.020	0.1752(3)	0.159(5)	6.47	SLF	
HD 37468	11286198[†]	0.046	1.6785(9)	1.49(5)	10.67	cont.	IV
			O-type giants, bright giants and supergiants (III, II and I)				
HD 66811	133422778	0.041	0.566(2)	3.0(3)	6.55	SLF+rot	
HD 97253	467065657	0.039	0.495(2)	2.2(2)	4.75	SLF+SPB?	*
HD 93843	465012898	0.018	0.3444(3)	4.9(1)	14.9	SLF+rot	
HD 156738	195288472	0.040	0.894(2)	1.01(8)	3.94	SLF	ND
HD 36861	436103278	0.046	0.205(3)	0.75(10)	4.04	SLF	
HD 150574	234648113	0.040	0.560(2)	2.5(2)	4.08	SLF+SPB?	
HD 152247	339570292	0.040	0.1586(9)	3.3(1)	7.89	SLF+rot	
HD 55879	178489528	0.041	0.155(1)	0.34(2)	4.15	SLF+SPB?	
HD 154643	43284243	0.040	0.109(2)	0.96(7)	4.36	SLF	
HD 152233	339565205	0.040	0.226(1)	8.8(5)	7.45	cont.	IV
HD 57061	106347931	0.041	1.5604(8)	19.3(7)	20.35	EB	
HD 36486	50743469	0.046	0.3494(10)	8.7(3)	14.02	EB	
CPD -472963	30653985	0.020	0.523(1)	2.3(2)	5.33	SLF+SPB?	
HD 57060	106349204[†]	0.041	0.4553(7)	186(6)	31.61	EB	
HD 156154	152659955	0.040	0.237(2)	4.9(4)	6.89	SLF+SPB?	
HD 112244	406050497	0.039	0.314(3)	8(1)	7.29	SLF	
HD 151804	337793038	0.040	0.538(1)	7.7(5)	8.88	SLF+SPB	*
HD 47129	220197273	0.046	1.646(2)	18(1)	12.35	EB+rot?	
HD 303492	459532732	0.039	0.233(2)	7.6(7)	9.57	SLF+SPB	*
HD 152249	339567904	0.040	0.504(2)	4.8(4)	4.92	SLF+SPB?	
HD 152424	247267245	0.040	0.423(3)	10(1)	8.11	SLF+SPB	
HD 154368	41792209	0.040	0.788(2)	5.2(4)	6.14	SLF+SPB?	
HD 152003	338640317	0.040	0.111(2)	10.1(8)	8.46	SLF+rot	
HD 152147	246953610	0.040	0.242(3)	7.1(8)	7.12	SLF+SPB?	
HD 37043	427395774	0.046	0.203(3)	1.6(2)	5.45	SLF+SPB?	

Table continued on the next page.

Table A.1: Continued.

HD	TIC	$1/\Delta T$ (d^{-1})	ν_{dom} (d^{-1})	A_{dom} (mmag)	S/N	Var. Type	Notes
			Early B-type dwarfs, subgiants and giants (V, IV, and III)				
HD 36960	427373484	0.046	1.0024(10)	0.106(4)	6.36	SLF	
HD 37042	427395058	0.046	0.317(1)	0.163(8)	4.79	SLF+rot	
HD 36959	427373476	0.046	0.299(1)	0.51(3)	5.83	cont.	IV
HD 43112	434384707	0.046	0.311(3)	0.031(3)	5.79	SLF+rot	
HD 37303	332856560	0.046	11.7889(8)	0.35(1)	15.29	hybrid	*
HD 35912	464839773	0.046	0.835(1)	4.0(2)	14.08	SPB	*
HD 48977	202148345†	0.046	0.516(2)	2.8(2)	12.0	SPB	*
HD 23466	426588729	0.038	0.405(1)	6.2(4)	13.69	EB	*
HD 34816	442871031	0.038	0.7922(2)	1.54(1)	29.19	rot	
HD 46328	47763235†	0.046	4.7715(1)	12.91(8)	30.65	β Cep	*
HD 50707	78897024	0.021	5.4187(2)	3.87(8)	30.64	β Cep	*
HD 37481	332913301	0.046	1.1052(8)	0.134(4)	8.74	hybrid	*
HD 16582	328161938	0.039	6.20598(9)	8.20(3)	27.88	β Cep	*
HD 37209	388935529	0.046	0.2709(9)	0.117(4)	11.02	hybrid	*
HD 26912	283793973	0.038	0.500(3)	3.4(4)	15.43	SPB	*
HD 37711	59215060	0.046	0.4503(7)	3.8(1)	18.57	SPB	*
HD 57539	10176636	0.041	1.6517(7)	3.2(1)	16.16	SPB	*
HD 41753	151464886†	0.046	0.6600(8)	5.3(2)	23.8	SPB	*
HD224990	313934087	0.036	0.5733(3)	0.504(7)	19.72	SPB/rot?	
HD37018	427393354	0.046	0.8320(8)	0.145(4)	8.87	SLF+rot	
			B-type giants, bright giants and supergiants (III, II, and I)				
HD 48434	234052684†	0.046	0.034(3)	6.5(7)	7.09	SLF+SPB?	
HD 61068	349043273	0.041	6.072(1)	5.5(3)	18.98	β Cep	*
HD 35468	365572007	0.046	0.2762(8)	0.214(7)	8.69	SLF+rot	
HD 44743	34590771†	0.046	3.9784(1)	5.86(3)	25.78	β Cep	*
HD 54764	95513457	0.041	0.490(1)	5.2(3)	9.12	SLF+rot	
HD 52089	63198307	0.021	0.2340(4)	0.78(3)	8.45	SLF+rot	
HD 62747	126586580	0.041	0.510(2)	12(1)	10.75	EB	
HD 51309	146908355	0.021	0.1500(8)	3.6(2)	10.34	SLF+SPB	*
HD 46769	281148636	0.046	0.2249(8)	0.087(3)	11.71	SLF+rot	
HD 27563	37777866	0.038	0.248(1)	3.0(2)	18.33	SLF+SPB?	
HD 53244	148109427	0.041	0.1598(2)	0.760(8)	29.4	SLF+rot	
HD 38771	66651575†	0.046	0.047(2)	8.4(7)	12.55	SLF+SPB	*
HD 37128	427451176†	0.046	0.059(2)	11.4(10)	11.07	SLF+SPB	*
HD 53138	80466973	0.041	0.1257(6)	3.37(9)	22.44	SLF+SPB	
HD 39985	102281507	0.046	0.2865(8)	0.104(3)	11.48	SLF+rot	
			Magnetic O- and B-type stars				
HD 37022	427394772	0.046	0.307(2)	1.08(9)	7.28	cont.	IV
HD 37061	427393920	0.046	0.9126(4)	0.90(1)	16.33	rot	*
HD 37742	11360636†	0.046	0.549(2)	4.1(4)	6.69	SLF	
HD 57682	187458882	0.041	0.2870(7)	0.44(1)	6.65	SLF+rot?	
HD 54879	177860391	0.041	1.002(1)	0.111(5)	7.15	SLF+rot	
HD 37479	11286209	0.046	1.6786(8)	6.6(2)	11.88	rot	
			Oe and Be stars				
HD 39680	91791971	0.046	1.688(2)	1.6(1)	4.55	SLF+SPB?	*
HD 45314	438306275	0.046	0.287(2)	1.7(1)	5.79	SLF+SPB?	*
HD 58978	139385056	0.041	8.990(1)	2.6(2)	14.58	β Cep	*

†: Light curve was extracted using our own method.

Table A.2: Detailed frequency analysis of multiperiodic pulsators. Errors on the last value are given in the brackets.

HD	Freq. #	ν (d^{-1})	A (mmag)	ϕ [-0.5, 0.5]	S/N	Notes
			β Cep stars			
HD 44743	ν_1	3.9784(1)	5.86(3)	-0.147(5)	25.8	
	ν_2	4.1832(5)	0.99(2)	0.26(2)	12.1	
	ν_3	0.2986(6)	0.83(2)	0.39(2)	6.3	
	ν_4	0.1339(8)	0.53(2)	0.14(3)	4.7	
	ν_5	5.046(2)	0.28(2)	0.32(7)	6.3	
	ν_6	7.962(2)	0.24(2)	-0.43(8)	6.3	$2\nu_1$
	ν_7	6.132(3)	0.14(2)	-0.4(1)	4.0	
	ν_8	6.556(3)	0.12(2)	-0.5(1)	4.0	
	ν_9	5.642(3)	0.12(2)	-0.5(1)	4.0	
HD 46328	ν_1	4.7715(1)	12.91(8)	0.373(6)	30.6	
	ν_2	9.5430(1)	1.808(9)	0.023(5)	30.4	$2\nu_1$
	ν_3	14.3144(4)	0.358(5)	-0.14(1)	27.4	$3\nu_1$
	ν_4	19.085(1)	0.080(5)	-0.31(6)	6.1	$4\nu_1$
	ν_5	2.380(2)	0.045(4)	0.38(8)	4.1	$1/2\nu_1$
	ν_6	23.860(7)	0.017(5)	-0.5(3)	6.1	$5\nu_1$
HD 50707	ν_1	5.4187(2)	3.87(8)	0.24(2)	30.6	
	ν_2	10.8370(5)	1.53(6)	0.47(4)	27.8	$2\nu_1$
	ν_3	5.1842(4)	1.42(5)	0.29(4)	16.9	tp
	ν_4	5.3083(5)	1.04(5)	-0.19(4)	14.9	tp
	ν_5	0.1208(5)	0.95(4)	0.30(4)	9.7	
	ν_6	5.5229(7)	0.70(4)	-0.26(6)	9.6	tp
	ν_7	0.2950(6)	0.62(3)	0.27(6)	7.2	
	ν_8	1.5652(9)	0.42(3)	0.28(8)	4.3	
	ν_9	1.0506(9)	0.39(3)	0.02(8)	4.5	
	ν_{10}	0.3609(9)	0.36(3)	0.28(8)	4.2	
	ν_{11}	0.9281(9)	0.36(3)	-0.00(8)	4.1	
	ν_{12}	2.135(1)	0.34(3)	0.40(9)	4.4	
	ν_{13}	8.241(1)	0.27(3)	-0.5(1)	4.3	
	ν_{14}	6.511(2)	0.26(3)	0.3(1)	4.3	
	ν_{15}	3.686(2)	0.23(3)	-0.3(1)	4.4	
	ν_{16}	6.349(2)	0.23(3)	0.2(1)	4.3	
	ν_{17}	7.896(2)	0.21(3)	-0.1(2)	4.3	
	ν_{18}	9.420(2)	0.19(3)	-0.5(2)	4.3	
	ν_{19}	8.440(2)	0.19(3)	-0.3(2)	4.3	
	ν_{20}	9.353(2)	0.18(3)	0.2(2)	4.3	
	ν_{21}	9.083(2)	0.15(3)	0.0(2)	4.1	
	ν_{22}	9.877(3)	0.13(3)	-0.4(2)	4.1	
	ν_{23}	16.021(6)	0.08(4)	0.2(5)	9.7	
	ν_{24}	21.672(9)	0.05(4)	-0.2(8)	9.7	$4\nu_1$
	ν_{25}	16.25(1)	0.04(4)	-0.2(9)	7.2	$3\nu_1$
	ν_{26}	18.41(2)	0.02(3)	0.0(2)	4.2	
	ν_{27}	24.34(2)	0.02(3)	0.0(2)	4.1	
HD 61068	ν_1	6.072(1)	5.5(3)	-0.34(5)	19.0	
	ν_2	5.9875(6)	5.4(1)	0.02(3)	21.4	mp1?
	ν_3	6.4530(5)	2.06(5)	0.29(2)	18.9	mp2?
	ν_4	0.6615(8)	0.68(3)	-0.45(4)	8.6	
	ν_5	5.922(1)	0.47(3)	-0.08(6)	8.6	mp1?
	ν_6	0.768(1)	0.46(2)	0.37(5)	5.8	
	ν_7	0.359(1)	0.44(2)	-0.35(5)	5.6	
	ν_8	0.893(1)	0.31(2)	0.20(5)	4.3	
	ν_9	0.091(1)	0.28(2)	-0.22(6)	4.3	$\nu_1 - \nu_2$
	ν_{10}	2.718(2)	0.21(2)	0.38(8)	4.2	
	ν_{11}	7.602(3)	0.18(3)	-0.3(1)	5.8	
	ν_{12}	12.149(4)	0.17(3)	-0.4(2)	8.6	$2\nu_1$

Table continued on the next page.

Table A.2: Continued.

HD	Freq. #	ν (d^{-1})	A (mmag)	ϕ [-0.5, 0.5]	S/N	Notes
			β Cep stars (continued)			
HD 61068	ν_{13}	6.520(3)	0.16(2)	-0.3(1)	4.3	mp2?
	ν_{14}	5.853(3)	0.13(2)	-0.1(1)	4.3	mp1?
	ν_{15}	6.240(4)	0.13(2)	-0.3(2)	5.8	
	ν_{16}	8.598(4)	0.11(2)	-0.3(2)	4.3	
	ν_{17}	8.963(4)	0.09(2)	0.3(2)	4.3	
	ν_{18}	12.011(6)	0.09(3)	-0.2(3)	5.8	$2\nu_2$
	ν_{19}	6.924(4)	0.09(2)	-0.2(2)	4.3	
	ν_{20}	10.234(5)	0.08(2)	0.3(2)	4.3	
	ν_{21}	12.526(7)	0.07(2)	0.3(3)	5.6	$\nu_1 + \nu_3$
HD 16582	ν_1	6.20598(9)	8.20(3)	0.428(4)	27.9	
	ν_2	3.628(1)	0.52(3)	-0.25(5)	7.4	
	ν_3	3.705(2)	0.34(3)	-0.37(8)	5.9	
	ν_4	1.507(2)	0.30(2)	-0.18(8)	4.7	
	ν_5	0.372(1)	0.28(2)	0.08(7)	4.4	
	ν_6	12.412(3)	0.23(3)	0.0(1)	7.4	$2\nu_1$
	ν_7	3.271(2)	0.20(2)	0.19(10)	4.3	
	ν_8	3.947(2)	0.20(2)	0.0(1)	4.2	
	ν_9	6.571(4)	0.12(2)	0.2(2)	4.7	
	ν_{10}	8.476(5)	0.08(2)	0.3(2)	4.3	
	ν_{11}	7.770(6)	0.08(2)	0.1(3)	4.3	
	ν_{12}	11.293(8)	0.07(2)	0.3(4)	4.7	
	ν_{13}	9.167(7)	0.07(2)	0.1(3)	4.3	
	ν_{14}	18.62(2)	0.02(2)	-0.1(10)	4.4	$3\nu_1$
			SPB stars			
HD 35912	ν_1	0.835(1)	4.0(2)	-0.15(5)	14.1	
	ν_2	0.723(1)	3.1(2)	0.39(5)	12.7	
	ν_3	0.645(1)	1.73(9)	0.03(5)	8.6	$2\nu_2 - \nu_1$
	ν_4	1.146(1)	1.33(7)	0.36(5)	7.1	
	ν_5	0.998(2)	1.12(7)	-0.16(6)	7.7	
	ν_6	0.904(1)	1.11(5)	-0.06(4)	7.9	$2\nu_1 - \nu_2$
	ν_7	0.574(1)	0.84(4)	-0.04(5)	6.4	
	ν_8	0.442(2)	0.52(4)	-0.20(7)	5.7	
	ν_9	0.197(2)	0.32(2)	0.37(6)	4.2	
	ν_{10}	1.356(4)	0.24(3)	0.4(1)	4.7	
	ν_{11}	4.345(6)	0.20(5)	-0.1(2)	5.8	
HD 26912	ν_1	0.500(3)	3.4(4)	-0.5(1)	15.4	
	ν_2	0.241(2)	3.3(3)	0.31(8)	15.2	$1/2\nu_1$
	ν_3	0.566(1)	3.0(2)	-0.02(6)	15.6	
	ν_4	0.093(1)	1.21(7)	-0.45(6)	10.2	
	ν_5	0.426(1)	0.94(6)	-0.14(6)	10.0	
	ν_6	0.162(1)	0.84(4)	-0.19(5)	9.5	
	ν_7	0.683(1)	0.57(3)	0.15(6)	7.3	
	ν_8	0.351(1)	0.48(3)	0.06(5)	7.1	
	ν_9	0.937(2)	0.39(3)	0.49(8)	7.1	
	ν_{10}	0.060(1)	0.34(2)	0.32(5)	6.4	
	ν_{11}	1.118(1)	0.34(2)	-0.10(7)	6.4	
	ν_{12}	0.9970(10)	0.31(1)	0.46(5)	6.0	$2\nu_1$
	ν_{13}	0.842(2)	0.26(2)	-0.12(8)	6.7	
	ν_{14}	0.751(1)	0.21(1)	0.45(5)	5.0	$3/2\nu_1$
	ν_{15}	1.209(1)	0.20(1)	-0.45(6)	4.7	
	ν_{16}	1.878(1)	0.142(10)	-0.44(7)	4.1	
	ν_{17}	1.954(1)	0.139(10)	-0.48(7)	4.2	$4\nu_1$
	ν_{18}	1.476(1)	0.110(7)	-0.25(6)	4.1	$3\nu_1$

Table continued on the next page.

Table A.2: Continued.

HD	Freq. #	ν (d^{-1})	A (mmag)	ϕ [-0.5, 0.5]	S/N	Notes
			SPB stars (continued)			
HD 57539	ν_1	1.6517(7)	3.2(1)	-0.27(3)	16.2	
	ν_2	1.5213(7)	2.10(7)	-0.24(3)	13.5	
	ν_3	0.8823(7)	1.35(4)	-0.04(3)	9.6	
	ν_4	1.7363(8)	0.74(3)	0.10(3)	7.1	
	ν_5	0.1728(8)	0.65(2)	0.37(3)	6.8	
	ν_6	0.7750(9)	0.50(2)	0.09(4)	5.7	
	ν_7	0.298(1)	0.36(2)	0.46(5)	5.0	
	ν_8	1.404(1)	0.34(2)	0.48(5)	4.6	$2\nu_2 - \nu_1$
	ν_9	3.059(2)	0.28(2)	-0.48(8)	5.5	$2\nu_2$
	ν_{10}	0.5173(10)	0.25(1)	0.36(4)	4.0	
	ν_{11}	0.079(1)	0.24(1)	0.15(5)	4.1	
	ν_{12}	0.642(1)	0.23(1)	-0.04(5)	4.0	
	ν_{13}	0.4126(9)	0.226(9)	0.49(4)	4.1	
	ν_{14}	1.892(1)	0.18(1)	-0.15(6)	4.0	
	ν_{15}	18.77(1)	0.02(1)	-0.4(6)	4.1	
HD 48977	ν_1	0.516(2)	2.8(2)	0.01(6)	12.0	
	ν_2	0.798(1)	1.67(10)	-0.39(6)	12.0	
	ν_3	0.687(1)	1.58(7)	-0.18(4)	10.5	
	ν_4	1.265(1)	1.01(5)	-0.13(5)	7.5	
	ν_5	0.586(1)	0.95(4)	0.17(5)	6.7	
	ν_6	0.991(1)	0.62(3)	0.23(5)	5.9	$2\nu_1$
	ν_7	0.282(1)	0.57(3)	-0.17(5)	6.2	$\nu_2 - \nu_1$
	ν_8	0.3516(10)	0.44(2)	-0.23(4)	5.3	
	ν_9	0.200(1)	0.42(2)	-0.28(5)	5.7	$2\nu_1 - \nu_2$
	ν_{10}	0.898(1)	0.35(2)	-0.13(4)	4.9	
	ν_{11}	1.923(2)	0.33(2)	0.35(6)	5.0	
HD 37711	ν_1	0.4503(7)	3.8(1)	0.27(3)	18.6	
	ν_2	0.245(1)	2.01(9)	-0.39(4)	12.2	
	ν_3	0.717(1)	1.12(5)	0.10(4)	6.9	
	ν_4	0.643(1)	0.96(4)	-0.09(4)	7.5	
	ν_5	0.0846(8)	0.91(3)	-0.15(3)	7.1	
	ν_6	1.324(2)	0.71(5)	0.45(8)	6.2	$3\nu_1$
	ν_7	1.539(1)	0.51(3)	0.14(5)	7.1	
	ν_8	0.5685(8)	0.296(9)	-0.27(3)	4.6	
	ν_9	1.005(1)	0.28(1)	0.21(5)	5.4	
	ν_{10}	1.156(1)	0.24(1)	-0.40(5)	4.6	
	ν_{11}	0.8178(10)	0.218(8)	0.22(4)	5.1	
	ν_{12}	0.916(1)	0.20(1)	0.24(5)	4.1	$2\nu_1$
	ν_{13}	1.423(2)	0.17(1)	0.10(7)	4.2	
HD 41753	ν_1	0.6600(8)	5.3(2)	0.25(3)	23.8	
	ν_2	0.7297(3)	3.25(4)	-0.16(1)	17.8	
	ν_3	0.1189(9)	0.79(3)	0.47(4)	7.9	
	ν_4	0.515(1)	0.58(3)	0.04(4)	7.4	
	ν_5	0.967(1)	0.47(2)	-0.21(4)	6.3	
	ν_6	1.401(1)	0.42(2)	-0.09(4)	6.2	$\nu_1 + \nu_2$
	ν_7	0.2946(10)	0.39(1)	0.01(4)	6.4	
	ν_8	1.073(1)	0.26(1)	0.00(4)	4.2	
	ν_9	0.8042(8)	0.222(7)	0.00(3)	4.3	$2\nu_2 - \nu_1$
	ν_{10}	1.246(1)	0.219(10)	0.27(4)	4.4	
	ν_{11}	1.592(1)	0.175(9)	0.06(5)	4.2	
	ν_{12}	1.498(1)	0.143(7)	-0.17(5)	4.1	
	ν_{13}	1.151(2)	0.13(1)	-0.40(10)	4.6	
	ν_{14}	2.228(2)	0.13(1)	-0.11(9)	4.0	$3\nu_2$
	ν_{15}	2.395(2)	0.13(1)	0.07(9)	4.1	
	ν_{16}	1.874(1)	0.126(7)	0.32(5)	4.3	

Table continued on the next page.

Table A.2: Continued.

HD	Freq. #	ν (d^{-1})	A (mmag)	ϕ [-0.5, 0.5]	S/N	Notes
			SPB stars (continued)			
HD 41753	ν_{17}	0.195(1)	0.118(5)	-0.23(4)	4.3	
	ν_{18}	2.061(1)	0.113(6)	-0.38(6)	4.3	$2\nu_1 + \nu_1$
	ν_{19}	1.708(3)	0.10(1)	-0.3(1)	4.2	
			Hybrids			
HD 37303	ν_1	11.7889(8)	0.35(1)	0.01(3)	15.3	
	ν_2	2.1388(6)	0.338(8)	-0.15(2)	11.5	
	ν_3	19.292(1)	0.28(1)	0.18(5)	15.3	$2\nu_1 - 2\nu_2$
	ν_4	1.8722(8)	0.211(7)	-0.27(3)	8.6	
	ν_5	13.433(1)	0.20(1)	-0.15(5)	11.5	
	ν_6	1.625(1)	0.117(6)	-0.02(5)	5.7	
	ν_7	4.256(2)	0.099(7)	0.25(7)	5.3	$2\nu_2$
	ν_8	0.989(1)	0.082(5)	0.13(6)	4.5	
	ν_9	14.980(2)	0.072(6)	-0.46(9)	5.7	
	ν_{10}	3.801(2)	0.071(6)	0.39(8)	4.0	
	ν_{11}	3.726(2)	0.059(5)	0.36(9)	4.2	
	ν_{12}	12.463(3)	0.059(6)	0.1(1)	4.0	
	ν_{13}	3.890(2)	0.053(5)	0.24(9)	4.4	
	ν_{14}	14.745(3)	0.052(6)	-0.1(1)	4.0	
	ν_{15}	23.630(3)	0.049(6)	-0.3(1)	5.7	
	ν_{16}	9.439(3)	0.048(6)	0.3(1)	4.0	mp2?
	ν_{17}	26.309(3)	0.047(6)	-0.1(1)	5.7	
	ν_{18}	13.056(3)	0.047(6)	-0.3(1)	4.2	
	ν_{19}	0.432(2)	0.046(4)	0.50(8)	4.1	
	ν_{20}	0.281(2)	0.044(4)	-0.10(8)	4.2	
	ν_{21}	9.864(3)	0.044(6)	-0.5(1)	4.0	
	ν_{22}	14.024(3)	0.041(6)	0.5(1)	4.2	
	ν_{23}	13.933(3)	0.039(5)	0.0(1)	4.4	$\nu_1 + \nu_2$
	ν_{24}	16.753(4)	0.038(6)	-0.1(1)	4.2	mp3?
	ν_{25}	18.624(4)	0.038(6)	-0.3(1)	4.2	
	ν_{26}	16.186(4)	0.037(5)	-0.4(1)	4.4	mp3?
	ν_{27}	13.664(4)	0.035(5)	0.0(1)	4.4	
	ν_{28}	7.730(4)	0.034(6)	-0.2(2)	4.0	mp1?
	ν_{29}	15.945(4)	0.033(5)	-0.1(2)	4.4	mp3?
	ν_{30}	11.538(4)	0.033(5)	0.4(2)	4.4	
	ν_{31}	25.426(4)	0.032(5)	0.5(1)	4.6	
	ν_{32}	24.895(4)	0.031(5)	0.4(2)	4.6	
	ν_{33}	7.436(4)	0.031(5)	0.1(2)	4.4	mp1?
	ν_{34}	9.695(4)	0.031(5)	0.1(2)	4.4	$\nu_1 - \nu_2$, mp2?
	ν_{35}	10.133(4)	0.031(5)	0.3(2)	4.4	mp2?
	ν_{36}	22.578(4)	0.031(5)	0.1(2)	4.6	
	ν_{37}	11.305(4)	0.030(5)	0.1(2)	4.4	
	ν_{38}	25.997(4)	0.030(5)	0.2(2)	4.6	
	ν_{39}	13.152(4)	0.030(5)	-0.1(2)	4.4	
	ν_{40}	15.261(4)	0.029(5)	-0.3(2)	4.4	
	ν_{41}	23.319(4)	0.028(5)	-0.3(2)	4.5	
	ν_{42}	16.985(5)	0.027(5)	0.4(2)	4.5	mp3?
	ν_{43}	16.363(5)	0.027(5)	0.4(2)	4.5	
	ν_{44}	13.248(5)	0.026(5)	0.3(2)	4.4	
	ν_{45}	8.140(5)	0.025(5)	-0.2(2)	4.4	
	ν_{46}	16.596(5)	0.024(5)	-0.3(2)	4.6	mp3?
	ν_{47}	17.926(5)	0.022(5)	-0.1(2)	4.6	
	ν_{48}	7.889(6)	0.022(5)	-0.2(2)	4.6	mp1?
HD 37481	ν_1	1.1052(8)	0.134(4)	0.07(3)	8.7	mp1?
	ν_2	1.260(1)	0.094(4)	-0.19(4)	7.0	mp1?
	ν_3	0.563(1)	0.077(3)	-0.30(5)	7.0	$1/2\nu_1$
	ν_4	1.432(1)	0.066(3)	0.48(5)	5.9	mp1?

Table continued on the next page.

Table A.2: Continued.

HD	Freq. #	ν (d^{-1})	A (mmag)	ϕ [-0.5, 0.5]	S/N	Notes
			Hybrids (continued)			
HD 37481	ν_5	8.346(2)	0.066(5)	0.16(7)	8.7	mp2?
	ν_6	5.632(2)	0.064(5)	-0.12(7)	8.7	
	ν_7	0.815(1)	0.056(3)	-0.29(5)	5.4	
	ν_8	8.901(2)	0.055(4)	-0.25(8)	8.8	
	ν_9	6.651(2)	0.054(4)	-0.16(8)	8.8	
	ν_{10}	7.661(3)	0.037(4)	0.47(10)	7.0	
	ν_{11}	0.309(2)	0.037(3)	-0.45(7)	4.1	$2\nu_2 - 2\nu_1$
	ν_{12}	8.246(2)	0.034(3)	-0.36(10)	5.8	mp2?
	ν_{13}	0.728(2)	0.034(3)	0.30(9)	4.8	
	ν_{14}	8.125(3)	0.025(3)	0.3(1)	5.4	mp2?
	ν_{15}	6.141(3)	0.025(3)	-0.3(1)	4.8	
	ν_{16}	9.691(4)	0.022(3)	0.1(1)	4.8	
HD 37209	ν_1	0.2709(9)	0.117(4)	0.23(3)	11.0	
	ν_2	6.488(1)	0.068(4)	0.17(5)	6.6	
	ν_3	8.031(1)	0.068(4)	0.06(5)	6.3	
	ν_4	7.827(1)	0.065(4)	0.08(6)	6.2	
	ν_5	7.098(1)	0.061(3)	0.16(6)	6.9	
	ν_6	0.583(1)	0.055(3)	-0.36(5)	6.2	$2\nu_1$
	ν_7	7.517(2)	0.053(3)	0.48(6)	6.9	
	ν_8	1.717(2)	0.043(3)	-0.10(7)	6.1	
	ν_9	0.478(2)	0.043(3)	-0.35(6)	5.4	
	ν_{10}	0.159(2)	0.043(3)	0.47(7)	5.7	
	ν_{11}	7.686(2)	0.037(3)	-0.19(9)	6.9	
	ν_{12}	8.126(2)	0.037(3)	-0.30(9)	6.9	
	ν_{13}	6.779(3)	0.031(3)	0.3(1)	6.9	$\nu_1 + \nu_2$
	ν_{14}	6.902(3)	0.028(3)	0.05(10)	5.3	
	ν_{15}	1.068(3)	0.025(3)	0.0(1)	4.6	
	ν_{16}	8.637(3)	0.024(3)	0.4(1)	5.3	
	ν_{17}	8.900(3)	0.024(3)	0.0(1)	5.3	
	ν_{18}	6.168(3)	0.023(3)	0.1(1)	5.3	
	ν_{19}	8.401(3)	0.022(3)	0.3(1)	4.6	
	ν_{20}	7.196(3)	0.019(3)	0.4(1)	4.3	
			Be/Oe stars			
HD 58978	ν_1	8.990(1)	2.6(2)	-0.28(6)	14.6	
	ν_2	8.514(1)	2.5(1)	-0.26(5)	18.1	
	ν_3	3.691(2)	0.9(1)	0.4(1)	6.6	
	ν_4	4.405(4)	0.6(1)	0.1(2)	4.4	
	ν_5	0.172(3)	0.62(7)	0.2(1)	4.9	
	ν_6	1.148(3)	0.61(7)	-0.1(1)	4.8	
	ν_7	13.395(4)	0.6(1)	0.0(2)	6.6	
	ν_8	7.249(4)	0.56(9)	0.2(2)	4.7	
	ν_9	7.854(4)	0.53(10)	-0.4(2)	4.7	
	ν_{10}	6.032(4)	0.47(9)	0.1(2)	4.7	
	ν_{11}	5.938(4)	0.44(8)	0.2(2)	4.9	
	ν_{12}	4.222(5)	0.43(9)	0.0(2)	4.7	
	ν_{13}	10.825(8)	0.3(1)	0.5(3)	6.6	
	ν_{14}	7.437(6)	0.31(8)	0.4(3)	4.9	
	ν_{15}	7.141(6)	0.29(8)	-0.3(3)	4.9	
	ν_{16}	7.390(6)	0.29(8)	0.3(3)	4.9	
	ν_{17}	5.307(6)	0.27(8)	0.2(3)	4.9	
	ν_{18}	6.905(8)	0.22(8)	-0.1(3)	4.9	
	ν_{19}	8.296(10)	0.18(8)	-0.1(4)	4.9	
	ν_{20}	14.90(1)	0.17(9)	0.3(5)	4.7	
	ν_{21}	13.10(1)	0.16(9)	-0.4(5)	4.7	
	ν_{22}	12.33(1)	0.15(8)	-0.3(5)	4.9	
	ν_{23}	10.14(1)	0.15(8)	0.2(5)	4.9	

Table continued on the next page.

Table A.2: Continued.

HD	Freq. #	ν (d^{-1})	A (mmag)	ϕ [-0.5, 0.5]	S/N	Notes
			Be/Oe stars (continued)			
HD 58978	ν_{24}	11.89(1)	0.13(8)	0.1(6)	4.9	
	ν_{25}	17.98(2)	0.1(1)	0.2(9)	4.4	$2\nu_1$
	ν_{26}	12.68(2)	0.11(8)	-0.1(7)	4.9	
	ν_{27}	15.17(2)	0.10(8)	-0.3(8)	4.9	
	ν_{28}	22.39(3)	0.1(1)	0.0(10)	6.6	
	ν_{29}	17.80(3)	0.07(8)	0.0(10)	4.9	
	ν_{30}	17.21(3)	0.06(8)	0.0(10)	4.9	
	ν_{31}	21.62(4)	0.05(8)	0.0(20)	4.9	
HD 39680	ν_1	1.688(2)	1.6(1)	-0.39(7)	4.6	
	ν_2	0.235(2)	1.18(9)	-0.36(8)	4.0	
	ν_3	6.493(9)	0.29(10)	0.4(3)	4.0	
HD 45314	ν_1	0.287(2)	1.7(1)	0.49(7)	5.8	
	ν_2	1.183(2)	1.32(10)	-0.09(7)	4.9	
	ν_3	2.219(2)	1.2(1)	-0.50(9)	4.6	
	ν_4	1.464(2)	1.17(9)	0.25(8)	4.8	$\nu_1 + \nu_2$
	ν_5	3.378(5)	0.9(2)	0.5(2)	5.7	
			NU Ori			
HD 37061	ν_1	0.9126(4)	0.90(1)	-0.19(2)	16.3	tp?
	ν_2	0.7197(5)	0.51(1)	0.15(2)	11.2	tp?
	ν_3	1.1183(9)	0.257(9)	0.44(4)	7.5	tp?
	ν_4	0.1369(9)	0.215(8)	-0.29(4)	8.1	
	ν_5	1.8291(9)	0.203(7)	-0.39(3)	6.6	$2\nu_1$
	ν_6	1.4394(9)	0.177(7)	0.02(4)	6.8	$2\nu_2$
	ν_7	0.5892(9)	0.139(5)	0.39(4)	6.2	
	ν_8	0.3426(9)	0.113(4)	-0.39(3)	5.5	
	ν_9	1.710(1)	0.107(5)	-0.39(4)	5.7	
	ν_{10}	2.738(2)	0.084(5)	-0.20(6)	5.9	$3\nu_1$
	ν_{11}	0.982(1)	0.079(3)	0.44(4)	4.7	
	ν_{12}	3.656(2)	0.064(5)	-0.47(9)	5.7	$4\nu_1$
	ν_{13}	0.052(1)	0.060(3)	0.31(5)	4.1	
	ν_{14}	1.220(2)	0.046(3)	0.27(6)	4.2	
			Upper-main sequence			
HD 97253	ν_1	0.495(2)	2.2(2)	-0.5(1)	4.7	
	ν_2	0.755(2)	2.0(2)	0.1(1)	4.7	
	ν_3	0.401(2)	1.7(2)	0.4(1)	4.0	
	ν_4	0.889(3)	1.6(2)	-0.4(1)	4.0	
HD 151804	ν_1	0.538(1)	7.7(5)	0.26(6)	8.9	
	ν_2	0.261(2)	5.5(4)	-0.21(8)	8.9	$1/2\nu_1$
	ν_3	0.454(2)	5.4(4)	0.24(8)	7.0	
	ν_4	0.656(2)	5.1(4)	-0.23(8)	7.7	
	ν_5	0.1052(6)	4.0(1)	0.40(3)	5.7	
	ν_6	0.848(1)	3.3(2)	0.11(6)	7.1	
	ν_7	0.170(2)	2.9(2)	-0.15(7)	7.5	
	ν_8	0.759(2)	2.3(2)	0.08(7)	6.7	$3/2\nu_1$
	ν_9	1.091(2)	1.5(1)	-0.17(9)	5.6	$2\nu_1$
	ν_{10}	0.375(1)	1.45(9)	-0.10(6)	5.2	
	ν_{11}	1.441(2)	1.2(1)	-0.26(9)	4.7	
	ν_{12}	1.174(1)	1.15(7)	0.30(6)	4.7	
	ν_{13}	1.623(2)	1.07(8)	-0.02(8)	4.4	$3\nu_1$
	ν_{14}	1.552(1)	0.98(6)	-0.35(6)	4.2	

Table continued on the next page.

Table A.2: Continued.

HD	Freq. #	ν (d^{-1})	A (mmag)	ϕ [-0.5, 0.5]	S/N	Notes
			Upper-main sequence (continued)			
HD 303492	ν_1	0.233(2)	7.6(7)	0.42(10)	9.6	
	ν_2	0.420(2)	7.6(8)	-0.4(1)	12.3	
	ν_3	0.358(1)	6.2(3)	-0.10(6)	10.3	$2\nu_2 - 2\nu_1$
	ν_4	0.603(2)	5.8(4)	0.31(7)	10.3	$2\nu_2 - \nu_1$, mp1?
	ν_5	0.148(2)	5.6(6)	0.2(1)	10.0	
	ν_6	0.669(1)	3.8(2)	-0.45(6)	9.1	$\nu_1 + \nu_2$, mp1?
	ν_7	0.531(2)	3.5(3)	-0.05(9)	9.9	mp1?
	ν_8	0.910(1)	3.0(2)	-0.33(7)	7.7	$2\nu_2 + \nu_1$
	ν_9	0.0817(9)	1.97(8)	0.43(4)	7.9	$2\nu_1 - \nu_2$
	ν_{10}	0.776(2)	1.9(2)	-0.21(8)	6.5	$\nu_1 + \nu_3$
	ν_{11}	1.244(1)	1.42(7)	-0.47(5)	5.3	$3\nu_2$
	ν_{12}	1.138(1)	1.22(8)	-0.36(7)	5.1	$\nu_1 + 2\nu_3$
	ν_{13}	0.983(1)	1.17(6)	-0.29(5)	5.8	
	ν_{14}	1.080(1)	0.95(5)	-0.39(6)	4.3	$\nu_1 + 2\nu_2$
	ν_{15}	1.305(1)	0.93(5)	-0.26(6)	4.3	$2\nu_1 + 2\nu_1$
	ν_{16}	1.446(1)	0.79(5)	0.05(6)	4.1	
	ν_{17}	1.734(1)	0.66(4)	0.42(6)	4.3	
HD 37128	ν_1	0.059(2)	11.4(10)	-0.20(9)	11.1	
	ν_2	0.241(3)	8.2(10)	-0.1(1)	9.5	
	ν_3	0.357(2)	6.2(5)	-0.02(8)	7.2	
	ν_4	0.150(4)	3.8(7)	0.2(2)	8.5	$2\nu_1$
	ν_5	0.591(3)	3.7(5)	-0.3(1)	6.4	
	ν_6	0.467(5)	3.3(7)	0.1(2)	6.7	$2\nu_2$
	ν_7	0.978(3)	3.0(4)	0.2(1)	6.2	
	ν_8	0.660(3)	2.0(2)	0.2(1)	5.1	
	ν_9	0.884(2)	1.6(1)	-0.15(7)	5.0	
	ν_{10}	0.743(3)	1.5(2)	0.4(1)	5.6	$3\nu_2$
	ν_{11}	1.176(3)	1.4(2)	-0.2(1)	5.2	
	ν_{12}	1.352(3)	1.3(1)	0.5(1)	4.2	
	ν_{13}	1.690(3)	1.2(1)	-0.1(1)	4.4	
	ν_{14}	1.912(3)	1.1(1)	0.2(1)	4.2	
	ν_{15}	1.525(4)	1.0(1)	0.4(2)	4.1	
HD 38771	ν_1	0.047(2)	8.4(7)	0.44(9)	12.5	
	ν_2	0.264(2)	6.6(5)	0.20(8)	11.5	
	ν_3	0.146(2)	5.8(4)	-0.16(6)	7.9	
	ν_4	1.106(3)	2.6(4)	0.2(1)	5.6	
	ν_5	0.529(2)	2.4(2)	0.05(8)	5.5	$2\nu_2$
	ν_6	0.841(3)	2.1(2)	-0.1(1)	5.5	
	ν_7	0.935(3)	1.6(2)	-0.3(1)	5.2	
	ν_8	0.426(2)	1.4(1)	0.02(8)	4.5	
	ν_9	1.396(2)	1.2(1)	-0.13(9)	4.3	
	ν_{10}	0.751(2)	1.16(9)	0.26(8)	4.2	$3\nu_2$
	ν_{11}	1.807(3)	1.0(1)	-0.3(1)	4.1	
			Post-main sequence			
HD 53138	ν_1	0.1257(6)	3.37(9)	0.17(3)	22.4	
	ν_2	0.250(1)	1.34(7)	0.31(5)	10.8	$2\nu_1$
	ν_3	0.339(1)	1.00(6)	0.27(6)	11.2	
	ν_4	0.436(1)	0.61(3)	-0.07(5)	10.1	
	ν_5	0.5111(8)	0.54(2)	0.49(3)	8.3	$4\nu_1$
	ν_6	0.7712(6)	0.45(1)	0.22(3)	9.4	
	ν_7	0.0412(8)	0.39(1)	-0.36(3)	9.2	
	ν_8	0.608(1)	0.34(2)	-0.11(5)	9.1	
	ν_9	0.9152(7)	0.277(9)	0.46(3)	8.0	
	ν_{10}	1.357(1)	0.090(5)	-0.43(5)	4.9	
	ν_{11}	0.982(1)	0.090(5)	-0.13(5)	4.6	

Table continued on the next page.

Table A.2: Continued.

HD	Freq. #	ν (d^{-1})	A (mmag)	ϕ [-0.5, 0.5]	S/N	Notes
		Post-main sequence (continued)				
HD 53138	ν_{12}	1.084(1)	0.075(5)	0.29(6)	4.5	
	ν_{13}	1.268(2)	0.067(4)	-0.25(7)	4.2	
HD 51309	ν_1	0.1500(8)	3.6(2)	0.45(7)	10.3	
	ν_2	0.1112(7)	3.4(2)	0.22(6)	12.3	
	ν_3	0.2777(9)	3.4(3)	-0.23(8)	10.1	$\nu_1 + \nu_2$
	ν_4	0.483(1)	2.1(2)	0.01(9)	8.8	
	ν_5	0.4343(10)	1.9(2)	0.08(8)	7.9	$3\nu_1$
	ν_6	0.1841(8)	1.8(1)	-0.19(7)	6.7	$2\nu_1 - \nu_2$
	ν_7	0.238(1)	1.6(2)	-0.3(1)	7.7	$2\nu_2$
	ν_8	0.6463(9)	1.5(1)	0.33(7)	7.1	
	ν_9	0.9298(6)	1.31(7)	0.11(5)	5.6	
	ν_{10}	0.8511(8)	1.18(8)	-0.03(7)	5.4	
	ν_{11}	0.3676(7)	1.16(7)	0.34(6)	5.5	$\nu_1 + 2\nu_2$
	ν_{12}	0.586(1)	1.1(1)	-0.12(10)	6.5	
	ν_{13}	0.319(1)	1.01(9)	0.10(9)	5.1	$2\nu_1$
	ν_{14}	0.756(1)	1.0(1)	0.1(1)	6.0	
	ν_{15}	0.545(2)	0.7(1)	-0.4(1)	5.4	
	ν_{16}	1.210(1)	0.73(9)	0.1(1)	4.9	
	ν_{17}	1.1416(9)	0.72(6)	0.46(8)	4.7	
	ν_{18}	1.4002(9)	0.68(6)	-0.29(8)	4.6	
	ν_{19}	0.042(2)	0.66(10)	-0.1(1)	4.9	$\nu_1 - \nu_2$
	ν_{20}	1.7851(7)	0.63(4)	0.30(6)	4.8	
	ν_{21}	1.364(1)	0.54(5)	-0.39(9)	4.7	
	ν_{22}	1.0987(9)	0.52(4)	0.26(8)	5.1	
	ν_{23}	1.5681(5)	0.50(2)	0.09(5)	4.0	
	ν_{24}	1.8620(6)	0.43(2)	-0.45(5)	4.1	
	ν_{25}	0.9783(7)	0.43(3)	0.47(6)	4.7	
	ν_{26}	1.2480(7)	0.42(2)	0.25(6)	4.0	
	ν_{27}	1.6401(6)	0.40(2)	-0.50(5)	4.4	
	ν_{28}	0.7070(6)	0.37(2)	0.12(5)	4.6	
	ν_{29}	1.944(2)	0.28(5)	-0.0(2)	4.8	
	ν_{30}	1.6827(8)	0.25(2)	-0.30(7)	4.0	
HD 27563	ν_1	0.248(1)	3.0(2)	0.23(5)	18.3	
	ν_2	0.325(1)	1.39(7)	0.43(5)	12.9	
	ν_3	0.5320(9)	0.86(4)	0.04(4)	14.1	$2\nu_1$
	ν_4	0.1365(7)	0.53(2)	0.31(3)	10.6	
	ν_5	0.398(1)	0.51(3)	0.08(6)	9.1	
	ν_6	0.5929(6)	0.49(1)	-0.07(3)	9.1	$\nu_1 + \nu_2$
	ν_7	0.6622(8)	0.46(2)	-0.09(4)	7.9	
	ν_8	0.0460(6)	0.269(7)	0.02(3)	7.8	$\nu_2 - \nu_1$
	ν_9	1.0797(8)	0.26(1)	0.16(4)	8.9	
	ν_{10}	0.8605(8)	0.248(9)	-0.35(4)	8.7	
	ν_{11}	0.763(1)	0.156(8)	-0.12(5)	7.2	$3\nu_1$
	ν_{12}	1.2647(10)	0.137(6)	0.01(5)	5.9	
	ν_{13}	1.5381(9)	0.093(4)	-0.31(4)	5.6	
	ν_{14}	0.9307(8)	0.088(3)	-0.34(4)	5.6	
	ν_{15}	1.626(1)	0.065(3)	-0.33(5)	4.4	
HD 46769	ν_1	0.2249(8)	0.087(3)	0.41(3)	11.7	
	ν_2	0.108(1)	0.063(3)	0.27(4)	9.4	$1/2\nu_1$
	ν_3	0.461(2)	0.034(3)	-0.23(8)	4.8	$2\nu_1$
	ν_4	0.321(2)	0.031(3)	0.04(8)	5.0	$3/2\nu_1$
	ν_5	0.539(3)	0.019(3)	-0.0(1)	4.1	$5/2\nu_1$

Notes: Potential triplets or multiplets are indicated as follows: tp/tp? (triplet) or mp/mp? (multiplet) followed by a number if more than one was detected.

Appendix B: MESA & GYRE inlists

Appendix B.1: MESA

```
&star_job

  ! start a run from a saved model
    load_saved_model = .false.

  ! save a model at the end of the run
    save_model_when_terminate = .false.
    save_photo_when_terminate = .false.

  ! display on-screen plots
    pgstar_flag = .false.

  ! history and profile columns
    history_columns_file = 'hist_columns.list'
    profile_columns_file = 'prof_columns.list'

! OPTIONS

! begin with a pre-main sequence model
    create_pre_main_sequence_model = .true.

    ! Model start up
    pre_ms_T_c = 1e5


! Opacity tables to use
    kappa_file_prefix = 'OP_a09_nans_removed_by_hand'
    ! kappa_CO_prefix = 'a09_co'
    ! kappa_lowT_prefix = 'lowT_fa05_a09p'

! Przybilla mixture
    initial_zfracs = 8

/ !end of star_job namelist


&controls

  !!!!!!!!!!!!!!!!!!!!!!!!!!!!!!!!!!!!!!!!
  !! MIXING CONTROLS
  !!!!!!!!!!!!!!!!!!!!!!!!!!!!!!!!!!!!!!!!

   use_Ledoux_criterion = .true.


 ! Do not smooth N^2
   num_cells_for_smooth_gradL_composition_term = 0

   alpha_semiconvection = 0d0
   semiconvection_option = 'Langer_85 mixing; gradT = gradr'
   thermohaline_coeff = 0d0
   alt_scale_height_flag = .true.
   MLT_option = 'Cox'
   mlt_gradT_fraction = -1
   okay_to_reduce_gradT_excess = .false.

   do_conv_premix = .true.

  !!!!!!!!!!!!!!!!!!!!!!!!!!!!!!!!!!!!!!!!
  !! OVERSHOOTING CONTROLS
  !!!!!!!!!!!!!!!!!!!!!!!!!!!!!!!!!!!!!!!!
```

```
! Minimum Diffusive mixing
  set_min_D_mix = .true.
  min_D_mix = 5d0 ! cm^2 / sec

  ! parameters specified in run_star_extras.f
  overshoot_new = .true.

  use_dedt_form_of_energy_eqn = .true.
  use_gold_tolerances = .true.

  write_profiles_flag = .false.
  photo_interval = 500000
  history_interval = 1

  pulse_data_format = 'GYRE'
  write_pulse_data_with_profile = .false.

! starting specifications
  !initial_mass = 15 ! specified in run_star_extras

! stop when the center mass fraction of he4 drops below this limit
  xa_central_lower_limit_species(1) = 'he4'
  xa_central_lower_limit(1) = 1d-3

  HB_limit = 0.95


  !!!!!!!!!!!!!!!!!!!!!!!!!!!!!!!!!!!!!!!!!!!
  !! ATMOSPHERE/WIND CONTROLS
  !!!!!!!!!!!!!!!!!!!!!!!!!!!!!!!!!!!!!!!!!!!

! Mass loss
  hot_wind_scheme = 'Vink'
  Vink_scaling_factor = 0.5d0


  atm_option = 'table'
  atm_table = 'photosphere'



  use_eosDT2 = .false.

  !!!!!!!!!!!!!!!!!!!!!!!!!!!!!!!!!!!!!!!!!!!
  !! MESH & RESOLUTION CONTROLS
  !!!!!!!!!!!!!!!!!!!!!!!!!!!!!!!!!!!!!!!!!!!

  varcontrol_target = 1d-4
  mesh_delta_coeff = 0.4


  max_allowed_nz = 20000 ! maximum number of grid points allowed
  mesh_adjust_use_quadratic = .true.
  mesh_adjust_get_T_from_E = .true.


! Additional resolution based on the pressure and temperature profiles

  mesh_dlogX_dlogP_extra = 0.15             ! resol coeff for chemical gradients
  mesh_dlogX_dlogP_full_on = 1d-6           ! additional resol on for gradient larger than this
  mesh_dlogX_dlogP_full_off = 1d-12         ! additional resol off for gradient smaller than this

  mesh_logX_species(1) = 'he4'              ! taking into account abundance of He4
```

```
  ! Additional resolution near the boundaries of the convective regions
    xtra_coef_os_full_on = 1.0
    xtra_coef_os_full_off = 1.0

    xtra_coef_os_above_burn_h = 0.5d0
    xtra_dist_os_above_burn_h = 0.5d0
    xtra_coef_os_below_burn_h = 0.5d0
    xtra_dist_os_below_burn_h = 0.5d0


    xtra_coef_czb_full_on = 1.0
    xtra_coef_czb_full_off = 1.0

    xtra_coef_a_l_hb_czb = 0.5              ! resol coeff above lower hburn convective boundary
    xtra_dist_a_l_hb_czb = 0.5              ! distance above lower hburn convective boundary
    xtra_coef_b_l_hb_czb = 0.5              ! resol coeff below lower hburn convective boundary
    xtra_dist_b_l_hb_czb = 0.5              ! distance below lower hburn convective boundary

    xtra_coef_a_u_hb_czb = 0.2              ! resol coeff above upper hburn convective boundary
    xtra_dist_a_u_hb_czb = 0.5              ! distance above upper hburn convective boundary
    xtra_coef_b_u_hb_czb = 0.2              ! resol coeff below upper hburn convective boundary
    xtra_dist_b_u_hb_czb = 0.5              ! distance below upper hburn convective boundary

/ ! end of controls namelist
```

Appendix B.2: GYRE

Example GYRE inlist.

```
&constants
/

&model
model_type = 'EVOL'
file = 'model.GYRE'
file_format = 'MESA'
/


&mode
l = 1
m = +1
n_pg_min = -50
n_pg_max = -1
/

&osc
nonadiabatic = .true.
outer_bound = 'UNNO'
/

&num
diff_scheme = 'MAGNUS_GL2'
n_iter_max = 50
/

&scan
    grid_frame = 'INERTIAL'
grid_type = 'INVERSE'
freq_min = 0.025180
freq_max = 3.932893
freq_max_units = 'CYC_PER_DAY'
```

```
freq_min_units = 'CYC_PER_DAY'
n_freq = 600
/


&grid
    n_inner = 5
alpha_osc = 10 ! At least 5 points per oscillatory wavelength
alpha_exp = 2 ! At least 1 point per exponential 'wavelength'

/


&nad_output
summary_file = 'output.HDF'
freq_units = 'CYC_PER_DAY'
summary_file_format = 'HDF'
summary_item_list = 'M_star,R_star,L_star,l,m,n_p,n_g,n_pg,omega,freq,E_norm,W' ! Items to appear in summar
```